INFORMATION TO USERS

This dissertation was produced from a microfilm copy of the original document. While the most advanced technological means to photograph and reproduce this document have been used, the quality is heavily dependent upon the quality of the original submitted.

The following explanation of techniques is provided to help you understand markings or patterns which may appear on this reproduction.

1. The sign or "target" for pages apparently lacking from the document photographed is "Missing Page(s)". If it was possible to obtain the missing page(s) or section, they are spliced into the film along with adjacent pages. This may have necessitated cutting thru an image and duplicating adjacent pages to insure you complete continuity.

2. When an image on the film is obliterated with a large round black mark, it is an indication that the photographer suspected that the copy may have moved during exposure and thus cause a blurred image. You will find a good image of the page in the adjacent frame.

3. When a map, drawing or chart, etc., was part of the material being photographed the photographer followed a definite method in "sectioning" the material. It is customary to begin photoing at the upper left hand corner of a large sheet and to continue photoing from left to right in equal sections with a small overlap. If necessary, sectioning is continued again — beginning below the first row and continuing on until complete.

4. The majority of users indicate that the textual content is of greatest value, however, a somewhat higher quality reproduction could be made from "photographs" if essential to the understanding of the dissertation. Silver prints of "photographs" may be ordered at additional charge by writing the Order Department, giving the catalog number, title, author and specific pages you wish reproduced.

University Microfilms

300 North Zeeb Road
Ann Arbor, Michigan 48106

A Xerox Education Company

73-11,032

ANDERSON, Russell Everett, 1945-
STUDY OF THE ACTIVE SITE OF FERREDOXIN FROM SYNECHOCOCCUS LIVIDUS.

The University of Michigan, Ph.D., 1972
Biophysics, general

University Microfilms, A XEROX Company, Ann Arbor, Michigan

THIS DISSERTATION HAS BEEN MICROFILMED EXACTLY AS RECEIVED.

STUDY OF THE ACTIVE SITE OF FERREDOXIN FROM SYNECHOCOCCUS LIVIDUS

by

Russell Everett Anderson

A dissertation submitted in partial fulfillment
of the requirements for the degree of
Doctor of Philosophy
(Biophysics)
in The University of Michigan
1972

Doctoral Committee:

Professor Richard H. Sands, Chairman
Professor Thomas M. Dunn
Professor Graham A. Palmer
Dr. Henry Crespi, Argonne National Laboratory

PLEASE NOTE:

Some pages may have

indistinct print.

Filmed as received.

University Microfilms, A Xerox Education Company

ACKNOWLEDGEMENTS

I am grateful to my research advisor, Professor Richard Sands for his help and patience and to Professor J. L. Oncley for his guidance and understanding throughout my years in Ann Arbor.

Professor Graham Palmer offered great assistance and instruction in the protein reconstitution.

I would like to thank Dr. Henry Crespi of Argonne National Laboratory for generously providing innumerable ferredoxin samples, even when it often meant a special growth and preparation cycle.

Drs. Tahashi Yonetoni and Mamoru Tamura of the Department of Physical Biochemistry, Johnson Research Foundation, University of Pennsylvania made the magnetic susceptibility measurements.

Professor Alan J. Bearden of Donner Laboratory, University of California at Berkeley kindly made the Mossbauer measurements.

I would particularly like to thank Drs. John Fritz and Dick Dunham for immeasurable help in and outside of the lab, but mostly for just taking the time.

The friendship and encouragement of my parents and friends is greatly appreciated.

This work was supported by NIH Biophysics Training Grant GM-1355 and by NIH research grants GM-12176 and RR-00417-01.

TABLE OF CONTENTS

	Page
List of Tables	v
List of Figures	vi
Chapter 1. Introduction	1
Chapter 2. Materials and Methods	7
Chapter 3. Theory	11
A. Magnetic Interactions	11
1. Diamagnetism	12
2. Paramagnetism	12
3. Ferromagnetism	16
B. Electrostatic Interactions	17
C. Electron Paramagnetic Resonance	23
D. Electron-Nuclear Double Resonance	32
E. Mossbauer Effect	39
Chapter 4. EPR and ENDOR Instrumentation	47
A. ENDOR RF Source	47
B. ENDOR Signal Channel	52
C. ENDOR Field Modulation	53
D. ENDOR Temperature Control	55
E. ENDOR Operating Procedure	59
Chapter 5. Results	62
A. Magnetic Susceptibility Results	62
B. EPR Results	66

TABLE OF CONTENTS (Cont.)

	Page
C. ENDOR Results	72
1. Ferric ENDOR	72
2. Ferrous ENDOR	82
3. Proton ENDOR	96
4. Nitrogen ENDOR	103
D. Mossbauer Results	107
1. Oxidized Protein	107
2. Reduced Ferredoxin	107
Chapter 6. Conclusions	124
Chapter 7. Summary	130
References	135
Appendix. Calculation of ENDOR Spectra with Program Listing	138

LIST OF TABLES

Table		Page
1.	Matrix Elements for Hyperfine Interaction	29
2.	Eta and q for the d-Orbitals	44
3.	Algal Ferredoxin Experimental Effective Hyperfine Constants	97
4.	Mossbauer Parameters for Oxidized and Reduced Algal Ferredoxin	123

LIST OF FIGURES

Figure		Page
1.	Crystal Field Splittings	19
2.	Exchange Energies	22
3.	ENDOR Energy Levels	34
4.	Typical ENDOR Spectra	40
5.	Block Diagram for EPR/ENDOR Spectrometer	48
6.	Block Diagram for ENDOR RF Section	49
7.	Sample Dewar Assembly	57
8.	Temperature Controller Circuit	58
9.	Magnetic Susceptibility of Oxidized Algal Ferredoxin	63
10.	Magnetic Susceptibility of Reduced Algal Ferredoxin	65
11.	EPR of Reduced Native Algal Ferredoxin with Computer Simulation	67
12.	EPR of Reduced Reconstituted ^{56}Fe and ^{57}Fe Algal Ferredoxin	70
13.	EPR of Reduced ^{57}Fe Reconstituted Algal Ferredoxin with Computer Simulation	71
14.	Experimental and Calculated ^{57}Fe (Ferric) ENDOR Spectrum at H_z	73
15.	Experimental and Calculated ^{57}Fe (Ferric) ENDOR Spectrum at H_z + 30 Gauss	74
16.	Experimental and Calculated ^{57}Fe (Ferric) ENDOR Spectrum at H_z + 60 Gauss	76
17.	Experimental and Calculated ^{57}Fe (Ferric) ENDOR Spectrum at H_z + 120 Gauss	77
18.	Experimental and Calculated ^{57}Fe (Ferric) ENDOR Spectrum at H_x - 80 Gauss	78

LIST OF FIGURES (Cont.)

Figure		Page
19.	Experimental and Calculated ^{57}Fe (Ferric) ENDOR Spectrum at H_x	80
20.	Experimental and Calculated ^{57}Fe (Ferric) ENDOR Spectrum at H_x + 60 Gauss	81
21.	Experimental ^{56}Fe and ^{57}Fe (Ferrous) ENDOR Spectra at H_z	84
22.	Experimental Difference and Calculated ENDOR Spectra at H_z	85
23.	Experimental ^{56}Fe and ^{57}Fe (Ferrous) ENDOR Spectra at H_z + 60 Gauss	86
24.	Experimental Difference and Calculated ENDOR Spectra at H_z + 90 Gauss	88
25.	Experimental ^{56}Fe and ^{57}Fe (Ferrous) ENDOR Spectra at H_y	89
26.	Experimental Difference and Calculated ENDOR Spectra at H_y	90
27.	Experimental ^{56}Fe and ^{57}Fe (Ferrous) ENDOR Spectra at H_y	91
28.	Experimental Difference and Calculated ENDOR Spectra at H_y	92
29.	Experimental ^{56}Fe and ^{57}Fe (Ferrous) ENDOR Spectra at H_x	94
30.	Experimental Difference and Calculated ENDOR Spectra at H_x	95
31.	Experimental ENDOR Spectrum of Protonated Algal Ferredoxin at H_x	98
32.	Experimental ENDOR Spectrum of Deuterated Algal Ferredoxin at H_x	99

LIST OF FIGURES (Cont.)

Figure		Page
33.	Experimental ENDOR Spectrum of Deuterated Algal Ferredoxin in Potassium Phosphate Buffer (D_2O) at H_x	100
34.	Experimental ENDOR Spectrum of Deuterated Algal Ferredoxin at H_z	102
35.	Experimental EPR Spectrum of ^{14}N and ^{15}N Chlorella Vulgaris Ferredoxin	104
36.	Experimental ^{14}N and ^{15}N ENDOR of Chlorella Vulgaris Ferredoxin at H_x	105
37.	Experimental and Computed Mossbauer Spectra for Oxidized Algal Ferredoxin ($T = 4^oK$, $H = 0$)	108
38.	Experimental and Computed Mossbauer Spectra for Oxidized Algal Ferredoxin ($T = 4^oK$, $H = 46$ K Gauss)	109
39.	Experimental Mossbauer Spectrum for Oxidized Algal Ferredoxin ($T = 77^oK$, $H = 0$)	110
40.	Experimental Mossbauer Spectrum for Oxidized Algal Ferredoxin ($T = 77^oK$, $H = 46$ K Gauss)	112
41.	Experimental and Computed Mossbauer Spectra for Reduced Algal Ferredoxin ($T = 250^oK$, $H = 580$ Gauss)	114
42.	Experimental and Computed Mossbauer Spectra for Reduced Algal Ferredoxin ($T = 250^oK$, $H = 46$ K Gauss)	115
43.	Experimental and Computed Mossbauer Spectra for Reduced Algal Ferredoxin ($T = 4^oK$, $H = 580$ Gauss)	118
44.	Experimental and Computed Mossbauer Spectra for Reduced Algal Ferredoxin ($T = 4^oK$, $H = 46$ K Gauss)	119

CHAPTER 1

INTRODUCTION

The purpose of this study is to characterize the magnetic interactions at the active site of a ferredoxin from the blue-green algae, Synechococcus lividus. The ferredoxins are oxidation-reduction proteins found in virtually all organisms, but initially the name was given (1) to an iron-containing protein from Clostridium pasteurianum, a nonphotosynthetic anaerobic bacterium. The term ferredoxin has since replaced the original names given to a number of proteins from green plants, mammals, and bacteria. This relabelling was initially justified by the fact that the ferredoxin from Clostridium pasteurianum could replace the original chloroplast protein catalyzing the photoreduction of NAD. These observations, coupled with further chemical and physical studies, have led to a definition for the class ferredoxin in terms of a number of characteristics (2):

1. Ferredoxins have equal amounts of labile sulfur and iron.
2. They lack other prosthetic groups such as hemes or flavins.
3. They have low molecular weights.
4. They are electron transport proteins.

The ferredoxin studied here is a member of a subgroup of ferredoxins, alternately called the two-iron or plant-type ferredoxins. All the members of this subgroup contain two iron and two labile sulfur atoms, have very similar amino acid sequences and very similar optical and electron spin resonance spectra.

The role of the ferredoxins in photosynthesis is as a single electron carrier, and with its very low reduction potential E'_o = -240 mv to•420 mv), it is one of the strongest reducing enzymes known. Ferredoxin receives the photoexcited electron from the excited chlorophyll molecule, but it is not known whether there is an intermediary species. The role of ferredoxin in photosynthesis can, however, be described in general as,

$$2\,X^-_{red} + 2\,Fd_{ox} \rightleftarrows 2\,X_{ox} + 2\,Fd_{red}$$

$$H^+ + 2\,Fd_{red} + NADP^+ \rightleftarrows 2\,Fd_{ox} + NADPH$$

The NADPH is then used in CO_2 fixation. Other ferredoxins have roles in the hydrogenase system of many anaerobic bacteria, in the reduction of nitrogen in nitrogen-fixing bacteria, and in mitochondrial electron transport.

In each of the above reactions, the ferredoxin transfers one electron. Chemical titrations with dithionite (3) have also shown these ferredoxins to accept only a single electron where the extent of chemical or photo-reduction is observed by a 50% decrease in the optical absorbance at 420 nm. This absorption is also lost if mercurials are added to bind the sulfur atoms from methionine, cysteine, and labile sulfur, or if the protein is denatured by acid, base, or heat; denaturation also evolves H_2S from the labile sulfur atoms.

Although the purpose of this and most other protein studies is to understand the biological function and the mechanisms involved in that function, often one must first determine the physical structure,

particularly at the active site. The ideal method for determining the complete protein structure is x-ray diffraction. This method however, requires a large, stable, single crystal, and such crystals for the two-iron ferredoxins have not yet been grown. The next best alternative is to use the various spectroscopic techniques. Unfortunately, optical absorbance is not specific enough to allow unique interpretation, hence it is generally used only as a label. For instance, in addition to using absorbance to determine the extent of reduction, the ratio of "active-site" absorbance at 420 nm to protein (primarily tryptophanes, tyrosines, and phenylalanines) absorbance at 276 nm is used as a measure of purity.

Paramagnetic molecules such as the reduced ferredoxins are most successfully probed with the very specific techniques of electron spin resonance (EPR (4), electron-nuclear double resonance (ENDOR) (5), and magnetic susceptibility (6); since the ferredoxins contain iron, both oxidation states can also be studied by Mossbauer effect spectroscopy (7).

The EPR spectrum is similar for all two-iron ferredoxins, and has an average g-value of 1.97. Comparison of the total EPR absorption of reduced ferredoxin and that of a standard reveals (4) that the EPR signal is due to one electron per mole of protein; the oxidized protein exhibits no EPR signal. This information supports the chemical evidence that the ferredoxin is a one electron acceptor.

When spinach ferredoxin was reconstituted (8) with ^{57}Fe ($I = 1/2$), the EPR signal broadened, indicating that at least one of the iron atoms had a hyperfine interaction with the net electron spin. A similar experiment (9) with ferredoxin from Pseudomonas putida and pig adrenal cortex showed a 1:2:1 triplet at g_z, indicating that at that field the hyperfine interactions between the net electron spin and the two nuclei were nearly identical; later ENDOR evidence (5) showed the interactions not to be equal at other fields. Although these latter two proteins are not identical to spinach ferredoxin, it was tentatively concluded that all two-iron ferredoxins have both of their iron atoms at the active site. Putidaredoxin was grown (10) on ^{33}S ($I = 3/2$) instead of the naturally abundant ^{32}S ($I = 0$) to show that sulfur (cysteine and/or methionine and/or labile sulfur) is also at the active site. When this protein was reconstituted with ^{33}S but grown on ^{32}S (hence cys and met had ^{32}S but the labile sulfurs had ^{33}S), the effect (11) was intermediate between those specimens grown on ^{33}S and ^{32}S. The conclusion was that both cysteine (and/or methionine) and labile sulfur were at the active site. A repeat of the reconstitution experiment with ^{80}Se ($I = 0$) and ^{77}Se ($I = 1/2$) demonstrated (12) (although selenium did alter the symmetry of the active site) that for seleno-putidaredoxin, both the labile selenium (hence sulfurs) are at the active site. A similar selenium reconstitution experiment was performed with parsley ferredoxin (13, 14) (more similar to spinach and algal ferredoxin than putidaredoxin) and showed a similar but

less clearly resolved effect. The conclusion was that the reducing electron goes into an active site which contains both iron atoms, both labile sulfur atoms, and at least one cysteine (or met) sulfur.

In addition to providing the qualitative information discussed above, EPR (4, 8), ENDOR (5), Mossbauer (7), and magnetic susceptibility (6) have also been successfully applied to spinach ferredoxin to yield detailed information about the active site. Of the four techniques, Mossbauer spectroscopy contains the most information about both oxidation states but the interpretation relies on parameters which can in principle be determined by EPR, ENDOR, and magnetic susceptibility. The complete ENDOR data for spinach ferredoxin was not possible, however, due to large proton signals which obscured some of the iron signals; exchangeable protons were replaced with deuterium but the problem was not appreciably diminished. Quite good Mossbauer simulations were obtained, even though two of the six parameters that ENDOR should have fixed were unknown. The data did show that the iron atoms are both high spin ferric in the oxidized state and are antiferromagnetically exchanged coupled resulting in diamagnetism at low temperatures. In the reduced state one iron becomes high spin ferrous with the paired electron in a d_{z^2} orbital.

In order to test the Mossbauer simulations most stringently, one would like to have as few free parameters as possible; in particular all of the ENDOR iron data is necessary. The ideal solution to

the difficulty in obtaining the ENDOR iron data is to use fully deuterated protein. Attempts to grow organisms (15) on totally deuterated mediums generally fail, but if the relative percentage of D_2O is increased over a period of weeks or months, some organisms will adapt. A number of lower organisms have been adapted in this manner and will grow in 99.7% D_2O, although growth rates are slowed and subcellular organization is less ordered (15). A fully deuterated ferredoxin from the blue-green algae, Synechococcus lividus is studied in this thesis using EPR, ENDOR, Mossbauer spectroscopy, and magnetic susceptibility. The intention is to accurately fix as many parameters as possible to test whether the Mossbauer simulations are still accurate within the constraints set by the other techniques. If this is true, the Mossbauer interpretations can more confidently be used to determine the nature of the ferredoxin active site.

CHAPTER 2

MATERIALS AND METHODS

The ferredoxin studied in this thesis is from the blue-green algae, Synechococcus lividus. The algae was grown by Dr. Henry Crespi (15) of Argonne National Laboratory at 50°C in 99.7% D_2O with a nutrient solution of inorganic salts; the nitrogen and carbon sources were a gas mixture of 95% N_2 and 5% CO_2. The necessary light and agitation were provided by fluorescent lighting through sealed lucite rocking trays. After approximately two weeks of growth, Dr. Crespi (16) extracted both ferredoxin and flavoprotein using DE-52 cellulose and G-50 Sephadex columns; the ferredoxin and flavoprotein are separated from each other on a hydroxyapatite column. All of the extractions were carried out in protonated phosphate buffers. The typical ferredoxin purity ratio was $\epsilon_{420}/\epsilon_{270}$ = 0.64.

Since the EPR spectrum of the algal ferredoxin was nearly identical to that of spinach ferredoxin, a few biochemical experiments were performed to compare the two proteins. Protonated algal ferredoxin was used in all of the preliminary steps.

An algal ferredoxin sample of initial purity 0.65 revealed no additional impurity with disk gel electrophoresis. The molecular weight was compared to that of spinach ferredoxin (molecular weight 10,500) by running the two proteins consecutively on a Sephadex G-75, molecular sieve, column. The elution volumes of spinach and algal

ferredoxin were virtually identical (75.2 ml and 74.6 ml, respectively) while a spinach dimer eluted off in two-thirds the volume (54 ml). The molecular weight of S. lividus ferredoxin was concluded to be approximately 10,500.

The molar iron content of algal ferredoxin was determined by removing the iron from the protein (with mersalyl acid) and complexing it with Tiron (disodium-1,2-dihydroxybenzene-3,5-disulfonate monohydrate). The extinction coefficient of the complex was measured (ϵ_1) at 420 nm. A known amount of iron was added to the solution, and the absorption of all complexed iron was measured (ϵ_2). The following ratios were obtained:

$$(\epsilon_{420})_{\text{protein}}/[\text{iron}]_{\text{protein}} = \frac{\epsilon_2 - \epsilon_1}{[\text{iron}]_{\text{std}}}$$

$$= 4730 \text{ Al Fd}$$

$$= 4700 \text{ Sp Fd}$$

Since spinach ferredoxin is known to have two iron atoms per molecule, the conclusion is that algal ferredoxin also has two iron atoms per molecule. In all concentration measurements, the extinction coefficient for spinach ferredoxin was used, $\epsilon_{420} = 9.4/\text{mM}$.

Algal ferredoxin was also judged identical to spinach ferredoxin by optical absorption, circular dichroism, and EPR measurements.

Ferredoxin enriched in ^{57}Fe was needed for EPR, ENDOR, and Mossbauer effect spectroscopy. Although no differences between

native and reconstituted ferredoxins have been observed, only reconstituted ^{56}Fe ferredoxin was used for comparisons with ^{57}Fe ferredoxin. Fully deuterated protein was used for the ENDOR experiments, but it was found that protons had exchanged onto the protein during the extraction procedure. These protons could only be removed by performing the reconstitutions in totally deuterated buffers and using totally deuterated columns. Stock DE-52 and trichloroacetic acid were twice freeze-dried and dissolved in 99.7% D_2O. Dry P-60 was dissolved in D_2O, poured into a column, and washed with deuterated phosphate buffer. The buffer itself was prepared from dry potassium phosphate dissolved in 99.7% D_2O. The proton contamination in each of the above steps was judged insignificant. A second reconstitution using protonated protein was performed similarly, but standard protonated buffers and columns were used; this sample was used for the ferric ENDOR and Mossbauer effect.

The reconstitution begins with the preparation of the apoprotein. The ferredoxin is first denatured in 2 N NaOD, then the iron is bound to excess Tiron, and the apoprotein is precipitated in 5% TCA. Following centrifugation at 10,000 RPM for 10 minutes, the apoprotein is redissolved and reprecipitated. This process was repeated three times. The final apoprotein was buffered in 0.1 M potassium phosphate.

The apoprotein was reconstituted (17) at pH 8.8 using a ten-fold excess of ferrous iron (^{57}Fe or ^{56}Fe), a fifty-fold excess of

dithiothreitol, and a five-fold excess of Na_2S. The two samples were shaken at two minute intervals for fifteen minutes, and then incubated at room temperature for two hours. The samples were bound to the DE-52 column, washed with 0.01 M potassium phosphate buffer, and eluted with the lowest possible salt concentration, 0.4 N NaCl, 0.01 M potassium phosphate buffer. The excess iron-sulfur complex remains bound to the DE-52 column. The samples are then passed through a P-60 column (in 0.01 M potassium phosphate) and concentrated with DE-52. The two samples were freeze-dried, taken up in 0.35 ml D_2O, placed in 4 mm O.D. quartz EPR tubes, reduced with a two-fold excess of dithionite in 0.1 M potassium phosphate buffer (pH 7.4), and frozen in liquid nitrogen.

CHAPTER 3

THEORY

A previous section has summarized much of the evidence that ferredoxin contains two iron atoms with sulfur ligands from cysteine and labile sulfur. Further understanding of the mechanisms by which the protein functions requires careful interpretation of the electrostatic and magnetic interactions at the active site. Since these interactions are functions of the active site environment, considerable structural information can also be derived without direct structural studies such as x-ray diffraction. The following is a brief review of the theory necessary to interpret the data presented later.

A. Magnetic Interactions (18)

There is associated with all electrons an intrinsic spin angular momentum (S), and (except for a free electron) an orbital angular momentum (L). Both are quantum mechanical effects, but the orbital momentum can in part be viewed classically as resulting from a circulating current due to the electron; electron spin has no classical analogue. These momenta have a magnetic dipole moment given by,

$$\vec{\mu} = -g_e \beta \vec{S}$$

where g_e is the dimensionless electronic gyromagnetic ratio (g_e = 2.0023), and β is the Bohr magneton ($\beta = e\hbar/2mc$, where -e and m are the charge and mass of the electron), a positive number with units of ergs/gauss. The energy of the magnetic dipole moment when it is subject to an applied magnetic field, is given by $E = -\vec{\mu} \cdot \vec{H}$. The

solution to this problem can be shown to be identical to its classical analogue, the gyroscope. The effect of the applied field will be to cause the magnetic dipole to precess about an axis parallel or anti-parallel to the field. In a macroscopic sample, all of these moments will behave similarly resulting in a bulk term called the magnetization, $\vec{M}$. $\vec{M}$ generally varies linearly with the applied field and hence can be written, $\vec{M} = \chi \vec{H}$, where the magnetic susceptibility χ (in general a dimensionless tensor), is usually independent of field, but may vary with other parameters, such as spin and temperature. A new term, the magnetic induction, is then defined as $\vec{B} = \vec{H} + 4\pi\vec{M} = (1 + 4\pi\chi)H$. There are three cases for χ:

1. Diamagnetism, $\chi_D < 0$:

All materials possess diamagnetism, a quantum mechanical effect, in which magnetic moments are induced by the field. These moments align antiparallel to the applied field, hence $B < H$. χ_D is very small and is generally independent of both applied field and temperature.

2. Paramagnetism, $\chi_P > 0$:

Molecules with permanent net dipole moments are paramagnetic. This paramagnetism results from an alignment of these moments parallel to the field and, when present, is generally large compared with the χ_D for the same paramagnetic material. However, the paramagnetic sample is often diluted in a diamagnetic material

(e. g. water or the protein) resulting in a total diamagnetism which is greater than the paramagnetism.

The expectation value of the individual angular momenta, $\vec{J}$, is quantitized such that $\langle J_z \rangle = m_J \hbar$, where $m_J = -J, -J + 1, \ldots, +J$. When a magnetic field is applied, the following Hamiltonian describes the resulting electronic Zeeman energies:

$$\text{Energy}_{m_J} = \langle \mathcal{H} \rangle = g\beta \vec{H} \cdot \vec{J} = g\beta H m_J .$$

The "g" used in the above equation is in general a tensor and should not be confused with g_e, the constant electronic g-factor. The origin of the g-tensor will be discussed later.

For a system of N_o atoms, the calculation (18) of the paramagnetic susceptibility in a static magnetic field is simply the summation over the states, m_J, where each moment is weighted by its Boltzmann probability, $\exp(-E/kT)$. The approximation $E \simeq E_{m_J}$ is used in this calculation since the electronic Zeeman interaction dominates. The resulting sum can be expressed exactly with the Brillouin function,

$$\chi_o = N_o \left(\frac{2J + 1}{2J} \coth \frac{(2J + 1) g\beta HJ}{2JkT} - \frac{1}{2J} \coth \frac{g\beta HJ}{2JkT} \right)$$

For the approximation $g\beta H/kT < 1$ (where $T = 0.01\,^{\circ}K$ for nuclei, $T = 10\,^{\circ}K$ for electrons), one can write the Curie magnetic susceptibility with its inverse temperature dependence,

$$\chi_o \simeq N_o g^2 \beta^2 \frac{J(J + 1)}{3kT} \qquad \text{Equation 1}$$

Two informative complications may arise in Equation 1. First, the electronic g-tensor may be anisotropic, thereby resulting in an anisotropic magnetic susceptibility; this anisotropy is small in the problem of interest, and the random powder sample has a χ_o characteristic of an average g-value of 1.97. Second, the expectation value of the electron spin angular momentum may itself have a temperature dependence due to exchange interactions; this effect will prove to be very important and will be discussed later.

For the case of χ_o, a scalar, a field applied along the z-axis will result only in a z-component of the magnetization,

$$\vec{M} = \chi_o \vec{H} = \chi_o H_o \hat{k} = M_z \hat{k}$$

The fact that there is no x- or y- component to the net magnetization can be seen by considering the fact that the spins are precessing about H_z at the Larmor frequency, $\omega_o = -\gamma H_o$, where $\gamma = g\beta/\hbar$. Since each moment is precessing independently of its neighbor, there is no mechanism to produce the phase coherence necessary for a net, nonzero M_x or M_y. To observe magnetization in the x- or y-plane, a time dependent perturbing field, such as $2 H_y \cos\omega_1 t$, must be added in that plane. It can then be shown that if the frequency of that field, ω_1, is such that $\omega_1 = -\gamma H_o$, the spin moments will precess about H_1 as H_1 rotates about H_o. This time dependent field in the x-y plane will cause electronic Zeeman transitions, $\Delta m_s = \pm 1$.

The time dependent field at the electronic Zeeman frequency would eventually equalize the two spin state populations if there were

no additional processes which tend to return the populations to their Boltzmann levels. These so-called relaxation processes describe interactions among the spins and between the spin and the lattice. The spin-lattice relaxation time, T_1, describes the time necessary after H_o is changed, for M_z to equal 1/e times its thermal equilibrium value. This time determines the rate at which energy from the spin system can be dissipated in the lattice and hence determines how much power the sample can absorb from the radiating field. The spin-spin relaxation mechanisms are one of the processes responsible for the decay of the x and y components of the magnetization. They result from the effect of those random time-dependent dipolar fields of the spin moments which have static or slowly varying components as well as components varying at the Larmor frequency. These processes conserve the net spin and hence the net electronic Zeeman energy, but disturb the spin phase coherence introduced by the H_1 field; they contribute a relaxation rate $1/T'_2$. Also tending to restore the x and y magnetization components to zero are T_1 processes and variations in the Larmor frequency due to distributions (assumed Lorentzian) in the effective applied static field. The sum of all these relaxation rates, $1/T^*_2 = 1/2\ T_1 + 1/T'_2 + \gamma\Delta H_1$, determines the transverse relaxation rate, and hence the EPR and ENDOR intrinsic linewidths.

Both T_1 and T^*_2 are considered as first order effects on the M_i. Bloch (19) used this assumption to write down the

phenomonological equations describing the time dependence of the magnetization vector:

$$d\vec{M}_z/dt = (\vec{M} \times \vec{H})_z + (\vec{M}_o - \vec{M}_z)/T_1$$

$$d\vec{M}_{x,y}/dt = (\vec{M} \times \vec{H})_{x,y} - \vec{M}_{x,y}/T^*_2$$

The steady-state solutions to these equations can be expressed as real and imaginary components of a dynamic magnetic susceptibility. Using the definition for the susceptibility, $\vec{M} = \chi \vec{H}$, with $\chi = \chi' - \chi''$ and $H_1 = 2\, H_1 \mathrm{Re}(\exp i\omega t)$, one gets,

$$\chi'(\omega) = \frac{1}{2}\chi_o \omega_o T^*_2 \frac{(\omega_o - \omega)T_2}{1 + (\omega_o - \omega)^2 T^{*2}_2 + \gamma^2 H_1{}^2 T_1 T_2} \qquad \text{Equation 2}$$

$$\chi''(\omega) = \frac{1}{2}\chi_o \omega_o T^*_2 \frac{1}{1 + (\omega_o - \omega)^2 T^{*2}_2 + \gamma^2 H_1{}^2 T_1 T_2}$$

Note that both of these susceptibilities exhibit resonant behavior as ω approaches ω_o. For $\omega = \omega_o = \gamma H_o$, χ' is changing sign (passing through zero) and χ'' is maximized.

3. Ferromagnetism, $\chi_F >> 0$:

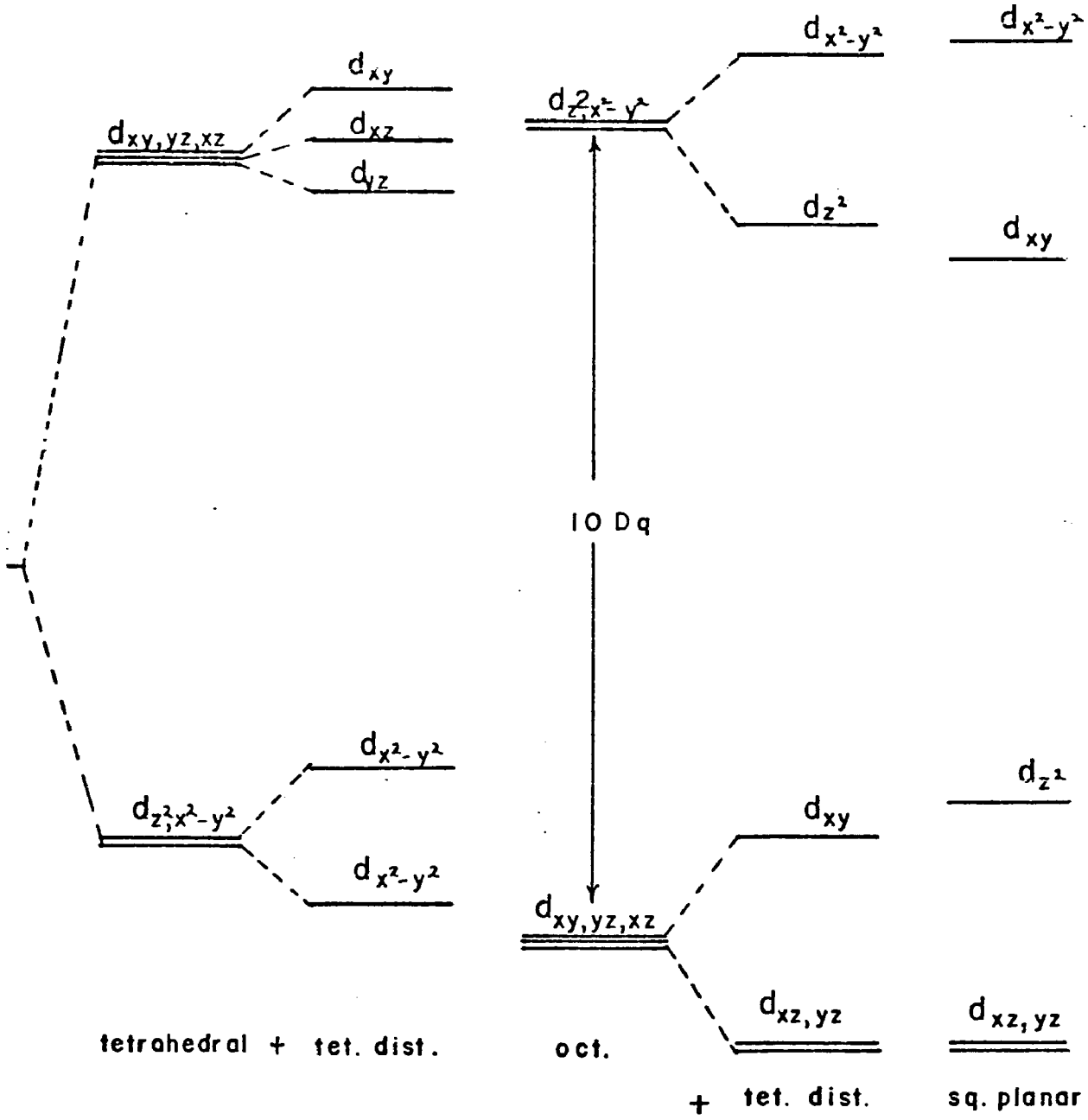
In ferromagnetic materials, all the individual moments align cooperatively due to both the applied magnetic field and an electrostatic exchange interaction (see below). The magnetization can be much greater than for the simple paramagnetic case, but will reduce to the latter at temperatures large enough for kT to dominate the exchange interaction.

B. Electrostatic Interactions (20)

The electrostatic interactions affecting the iron atoms will be of particular interest because these interactions will reflect the nature of the iron environment. The five d-orbitals will have either five electrons, giving ferric iron, or six electrons giving ferrous iron; in each case the spins are most commonly either aligned parallel resulting in the high spin case (S = 5/2 or 2 respectively) or paired two per orbital resulting in the low spin case (S = 1/2, S = 0). Exchange interactions result in free iron being high spin, while in a molecule the spin state is determined by interactions with the iron environment and the exchange interactions.

In addition to determining the iron spin state, external fields can also lift the degeneracy of the d-orbitals in a manner which reflects the symmetry of the ligands causing the field. This added set of electrostatic interactions can be most simply treated, but not always correctly, by assuming that the electrostatic field results from point charges situated around the iron. The assumption that there is no electron wave function overlap between the iron and ligand electrons is called the crystal field approximation. The resultant electrostatic potential at the center of the ligands can be calculated and expanded in terms of spherical harmonics (21); the spherical harmonics can in turn be expressed as angular momentum operators using the method of operator equivalents. This final form allows one to calculate the effect of different symmetries on the relative energies of the d-orbitals.

Tetrahedral symmetry (which will be assumed in most of what follows and justified by later data) results from point charges placed at four corners of a cube. This crystal field will most affect those d-orbitals which have a large electron probability near the ligand, hence raising the energy of that d-orbital. For the tetrahedral example, orbitals $d_{xy, xz, yz}$ remain degenerate but their energy is raised above the free iron case; d_{z^2} and $d_{x^2-y^2}$ are also degenerate, but their energy is raised less. The resulting energy differences for this and some other crystal field symmetries and some distortions are shown in Figure 1. It should be noted that some but not all degeneracies may be lifted. For example, both octahedral and tetrahedral crystal field symmetries result in two subsets of degenerate states. The energy difference between the two subsets is called the crystal field splitting, $10\ D_8$, where for the octahedral case $q = 2\ \langle r^4 \rangle /105$ and $D = 35\ Ze^2/4\ a^5$; $\langle r \rangle$ is the position expectation value for the electron in question and $\underline{a}$ is the distance from the center of the distribution to the ligands whose charge is Ze. The tetrahedral crystal field splitting is 4/9 that of the octahedral case. All the orbital degeneracies may be lifted by continuous distortions of the crystal fields to lower symmetries, but for systems with an odd number of spins, a two-fold degeneracy will always remain (Kramer's theorem); this degeneracy can only be lifted by an applied magnetic field and results in the electronic Zeeman splitting. It will be useful to note from Figure 1 that any method which determines the relative energies



FREE ION ENERGY

FIGURE 1. CRYSTAL FIELD SPLITTINGS.

of the d-orbitals will provide valuable information about the symmetry and strength of the crystal field.

One other feature of the crystal fields is that real wave functions result which are equal combinations of $\pm m_L$ wave functions. This means that there will be no net orbital angular momentum and hence no orbital contribution to the observed energy differences. An interaction which will be dealt with later, the spin-orbit interaction, will alter this "quenched" angular momentum condition by mixing wave functions $|m_L\rangle$ with $|m_L \pm 1\rangle$; the expectation value of L_z will no longer be zero and the resulting changes in the electronic Zeeman transitions are related to the magnitude of the interaction.

Evidence will be shown later to indicate that the electron spins on the two iron atoms in ferredoxin are coupled antiferromagnetically, i.e. their spins point in opposite directions and hence subtract. The interaction which couples the spins is written in the simple case as,

$$\mathcal{H} = -2 J S_1 \cdot S_2$$

and is called the exchange interaction. The above Hamiltonian was first used by Heisenberg to describe an exchange interaction resulting from the Coulombic inter-electron repulsion potential. This potential results in an energy difference of the spin states because of the Pauli exclusion principle, that is, the energy depends on the wave function spatial symmetry. Since this spatial wave function symmetry can also be expressed as spin symmetry, the electrostatic exchange interaction can also be expressed in terms of spin symmetry even

though it does not arise as a direct spin-spin interaction. J is the off-diagonal matrix element of the Coulomb interaction and is related to the extent of wave function overlap; it is not generally calculable. The above interaction results in ferromagnetism and is often dominated by super-exchange interactions. These latter interactions are presumably similar in origin but are mediated by bridging atoms between the two spins. The complexity and the failure of the Heisenberg theory to predict even some simple results requires that both the sign and magnitude of J be determined empirically.

The exchange interaction stabilizes the (anti-) aligned spin (S_1 and S_2) configuration resulting in a coupling between the two spins such that $\vec{S} = \vec{S}_1 + \vec{S}_2$. Thermal (kT) effects will compete with the exchange interaction so that in the high temperature limit, $kT > J$, the two spins will no longer be coupled. For the antiferromagnetically coupled case, the minimum total spin, $|S| = |S_1| - |S_2|$, occurs for $kT < J$; the maximum possible spin is $|S| = |S_1| + |S_2|$. Excited states weighted by the Boltzmann probability will occur at all temperatures resulting in a temperature dependent net spin and a magnetic susceptibility no longer describable by the Curie law. To calculate the relative energies of the excited states, it is convenient to rewrite the exchange interaction Hamiltonian as,

$$\mathcal{H}_{ex} = -2\,JS_1 \cdot S_2 = -J(S^2 - S_1^2 - S_2^2)$$

The results for the two cases of interest here are shown in Figure 2. Figure 2a represents the exchange energies for the oxidized ferredoxin

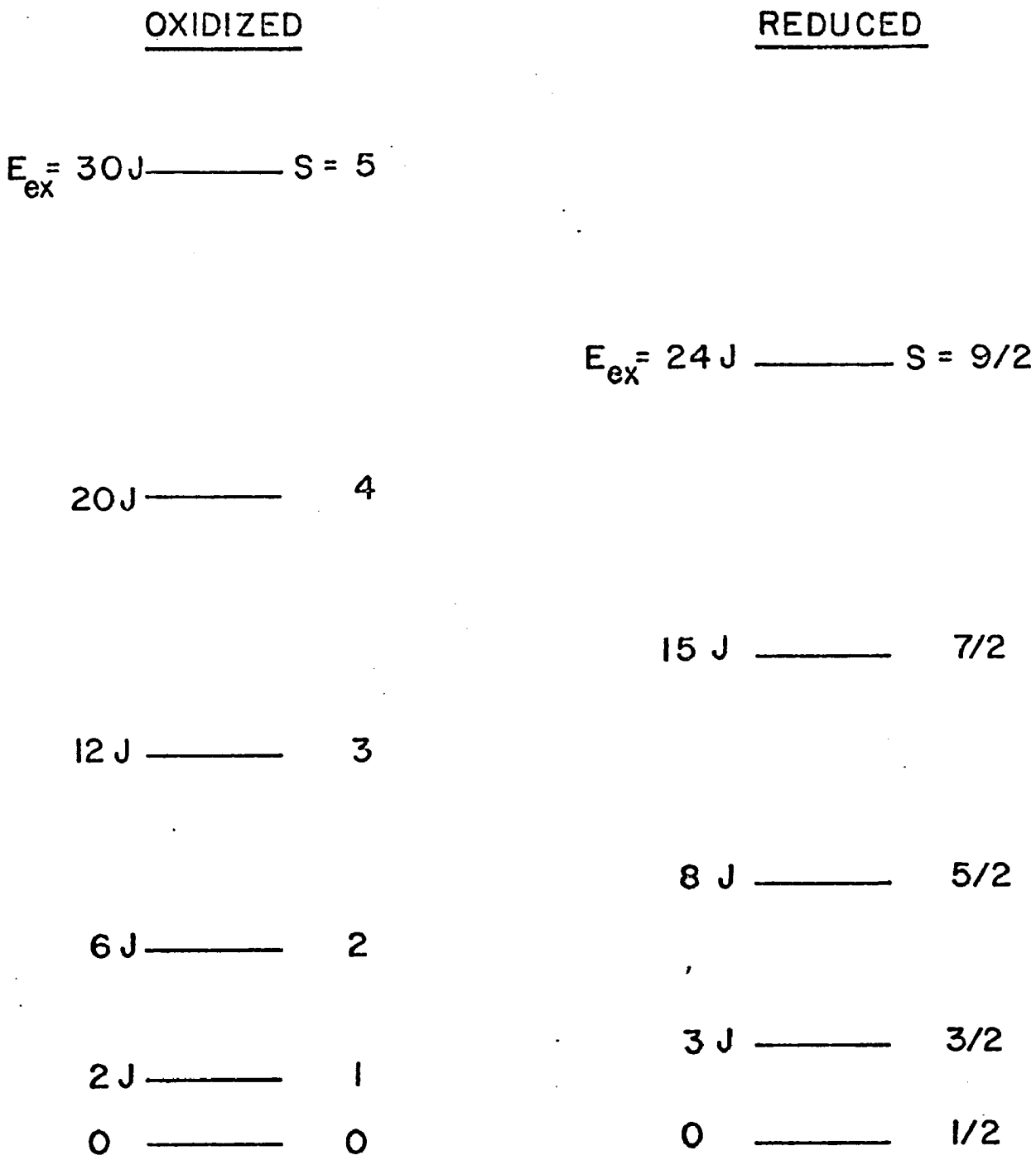


FIG. 2 EXCHANGE ENERGIES

where it will be seen that $S_1 = S_2 = 5/2$; for this case the excited states are at energies 2 J, 6 J, 12 J, 20 J, and 30 J. Figure 2b represents the case for reduced ferredoxin where $S_1 = 5/2$, $S_2 = 2$, and the excited states are at 3 J, 8 J, 15 J, and 24 J. To calculate the temperature dependence of the magnetic susceptibility, one must take the sum over all the states, each weighted by its Boltzmann probability.

C. Electron Paramagnetic Resonance

Electron paramagnetic resonance (EPR) occurs when the frequency of the time-dependent field, $2H_1 \cos\omega t$ in Equation 2, approaches ω_o. During resonance, the spin system will absorb power from H_1 in quanta $\hbar\omega$ as long as the two spin states have a population difference. The net power absorbed is derived using the dynamic susceptibilities and can be shown to be (22),

$$P = \frac{1}{T}\int_o^t \frac{dM}{dt} H_1 dt = 2\omega H_1^2 \chi''$$

Thus the power absorbed is proportional to χ'', the imaginary component of the complex dynamic susceptibility.

If χ'' always described the free electron case, EPR as a spectroscopic tool would be of little value. In real systems, numerous different resonances occur, most all of which are shifted from the free electron value. These resonance conditions are determined by magnetic interactions among the various angular momenta (both electronic spin and orbital momentum, and nuclear spin), and by

electrostatic interactions between electrons and the crystal field. Hence, information about these interactions is contained in the number and positions of the EPR resonances.

As mentioned previously, a cubic crystal field results in real electron wave functions with $\langle L_z \rangle = 0$. The orbital contribution to the Zeeman interaction then averages to zero to give,

$$\mathcal{H}_z = \beta (\vec{L} + g_e \vec{S}) \cdot \vec{H} = g_e \beta \vec{S} \cdot \vec{H}$$

Assuming no other interactions, the free electronic g_e value would fully describe this simple situation. However, the electron spin-orbit interaction, $\lambda L \cdot S$, can restore some net orbital angular momentum. This can be seen by rewriting the spin-orbit interaction as,

$$\lambda L \cdot S = \lambda [L_z S_z + \frac{1}{2} (L_+ S_- + L_- S_+)]$$

The x and y components of the spin-orbit interaction result in an admixture of states $|m_L \pm 1\rangle$ to the zeroth order states $|m_L\rangle$. Now $\langle L_z \rangle$ is no longer zero and the Zeeman Hamiltonian will have an orbital contribution.

It is convenient to write a spin-only Hamiltonian which includes both the spin and orbital Zeeman contributions,

$$\mathcal{H} = \beta \hat{S} \cdot g \cdot H$$

where g is now in general a tensor, and $\hat{S}$ is a fictitious spin defined such that the new wave functions (with the $L \cdot S$ admixed states) are eigenfunctions of S_z. The g-tensor, like any Hamiltonian tensor, can be diagonalized by an appropriate series of coordinate rotations,

and hence one can write the Zeeman interaction in the g-tensor principal axis frame as,

$$\mathcal{H} = \beta(g_x S_x H_x + g_y S_y H_y + g_z S_z H_z)$$

The elements of the g-tensor can be calculated (23) using perturbation theory for the Hamiltonian $\mathcal{H} = \mathcal{H}_o + \mathcal{H}_1$. $\mathcal{H}_o$ describes the electrostatic interactions and provides the zeroth order wave functions. Thus,

$$\mathcal{H}_o \psi_o^n = E_o^n \psi_o^n$$

where the ψ_o^n are the 3-d orbitals resulting from the crystal field. The perturbation Hamiltonian $\mathcal{H}_1 = \lambda[L \cdot S] + \beta H \cdot (L + 2S)$ contains both the Zeeman and spin-orbit terms. The problem is then to solve for the full Hamiltonian,

$$\mathcal{H} \psi^n = E^n \psi^n$$

where the ψ^n will be the perturbed wave functions,

$$\psi^n = \psi_o^n + \sum a_{nm} \psi_o^m$$

Proceeding with the calculation results in the more useful form for the full Hamiltonian,

$$\mathcal{H} = 2\beta(\delta_{ij} - \lambda \Lambda_{ij}) S_i H_j - \lambda^2 \Lambda_{ij} S_i S_j - \beta^2 \Lambda_{ij} H_i H_j \qquad \text{Equation 3}$$

where, $\Lambda_{ij} = \sum \frac{1}{E_o^m - E_o^n} \langle \varphi_o^m | L_i | \varphi_o^n \rangle \langle \varphi_o^n | L_j | \varphi_o^m \rangle$

and $\psi_o^n = \varphi_o^n \alpha_n^p$. φ = spatial, α = spin wave function.

The first term has the form of the desired spin-only Hamiltonian, with the elements of the g-tensor given by,

$$g_{ij} = 2(\delta_{ij} - \lambda \Lambda_{ij})$$

For a single electron in a tetrahedral crystal field with a rhombic distortion, the g-values are

$$g_{zz} = g_e$$

$$g_{yy} = g_e - 6\lambda/\Delta_{yz^2 - z^2}$$

$$g_{xz} = g_e - 6\lambda/\Delta_{xz - z^2}$$

Thus g_z is unshifted from the free electron g_e value. The axial anisotropy varies with the spin-orbit coupling and inversely with the crystal field strength. The magnitude of $g_x - g_y$ is a measure of the rhombic distortion. The second term in Equation 3 is a zero field splitting due to the spin-orbit interaction, but written as the product of spin-only operators. It is more commonly written as the traceless operator,

$$\mathcal{H} = D(S_z^2 - S(S+1)/3) + E(S_x^2 - S_y^2)$$

where $D = \frac{\lambda^2}{2}\Lambda_{zz}$ and $E = -\frac{1}{2}\lambda^2\Lambda_{zz} - \lambda^2\Lambda_{xx}$

Although the spin-orbit interaction is the more important zero-field term for transition metals, spin-spin dipolar interactions can also be written in the same form. In either case, zero-field splittings can be very large. One should note, however, that for $S = 1/2$, the zero-field terms vanish; this conveniently is the case for the ground state in the system of interest.

The third term is the temperature independent paramagnetic susceptibility. Since it does not change the spin transition energy, it is of no interest here.

Another dipolar interaction occurs between the electron spin and any nearby non-zero nuclear spin. This term varies as $1/r^3$ (where r is the distance from the nuclear moment to the average electron density) and has the classical dipolar angular dependence, $1-3\cos^2\theta$; this term describes the anisotropic hyperfine interaction. There is also an isotropic hyperfine interaction, or Fermi contact interaction, which can be written as $\underline{a}\,(I\cdot S)$ where the value of $\underline{a}$ is proportional to the s-state character (intrinsic or induced) of the electron. This number can be a guide to the electron density at the nucleus in question. The full calculation (23) of the hyperfine Hamiltonian for a single electron requires the use of the relativistic Dirac equation and includes the finite size of both the electron and the nucleus. For the more classical Pauli approximation, the hyperfine Hamiltonian reduces to terms for the orbital-nuclear interaction, the electron spin-nuclear spin dipolar interaction, and the contact interaction. Using the method of operator equivalents, the spatial operators can be replaced with spin operators to yield a more convenient form for the hyperfine interaction. For a single d-electron, the hyperfine Hamiltonian can then be written,

$$\mathcal{H}_{hyp} = -g_e\beta_e g_n\beta_n\left\langle\frac{1}{r^3}\right\rangle\left\{L\cdot I + \frac{1}{7}[4\, I\cdot S - (L\cdot S)(L\cdot I) - (L\cdot I)(L\cdot S) - \kappa I\cdot S\right\} \qquad \text{Equation 4}$$

where κ is a dimensionless constant representing one's ignorance about how much s-state character is induced by the valence electrons; both the sign and the magnitude of κ must be determined empirically.

The hyperfine interaction can be written as, $\mathcal{H}_{hyp} = I \cdot A \cdot S$ where the A-tensor contains both the isotropic and anisotropic parts; this interaction is generally three orders of magnitude smaller than the electronic Zeeman interaction, and splits each electron spin state into 2 I + 1 states. The hyperfine tensor, like the g-tensor, can be written in its principal axis frame such that,

$$\mathcal{H}_{hyp} = A_x S_x I_x + A_y S_y I_y + A_z S_z I_z$$

The A- and g-tensor principal axes needn't coincide. The principal A-values for a single electron in the various 3-d orbitals are calculated from Equation 4 and are shown in Table 1. This table will be particularly useful in trying to identify the electron distribution corresponding to observed hyperfine values.

Although the nuclear Zeeman interaction does not affect the energy differences observed in EPR, it does shift the levels and can be observed by ENDOR and NMR. It is generally of the same order or smaller than the hyperfine interaction. Assuming an isotropic g_N,

$$\mathcal{H}_{nucl\ Zeeman} = -g_n \beta_n H \cdot I$$

The final Hamiltonian of interest for EPR and ENDOR is,

$$\mathcal{H} = \beta H \cdot g \cdot S + I \cdot A \cdot S - g_n \beta_n H \cdot I$$

This tensor relation means that if a crystal is oriented such that its g_z axis is parallel to the static field, then for S = 1/2 (assume also that the g- and A-tensors are coincident) the hyperfine interaction will split the single electronic Zeeman line into 2 I + 1 lines, each separates by A_z, with the "center of gravity" at $h\nu = g_z \beta H_o$. The appendix

Table 1

Matrix Elements for Hyperfine Interaction

$$\mathcal{H}_{hyp} = -g_e\beta_e g_n\beta_n\left\langle\frac{1}{r^3}\right\rangle\left\{ L\cdot I + \frac{1}{7}[\,7\, I\cdot S - (L\cdot S)(L\cdot I) - (L\cdot I)(L\cdot S)] - KI\cdot S\right\} \quad \text{Equation 5}$$

given in units of $-g_e\beta_e g_n\beta_n\left\langle\frac{1}{r^3}\right\rangle$.

D-orbital	A_x	A_y	A_z
$d_{x^2-y^2}$	2/7 - K	2/7 - K	-4/7 - K
d_{z^2}	-2/7 - K	-2/7 - K	4/7 - K
d_{xz}	2/7 - K	-4/7 - K	2/7 - K
d_{yz}	-4/7 - K	2/7 - K	2/7 - K
d_{xy}	2/7 - K	2/7 - K	-4/7 - K

shows that if the orientation of the laboratory frame with respect to the g-frame is described in terms of the Euler angles (α, β, γ), then for a field applied along the laboratory z-axis the diagonalized Zeeman Hamiltonian can be written

$$\mathcal{H}_z = g_{eff}\beta H_o m_s$$

where, $g_{eff}^2 = g_x^2 \sin^2\beta\cos^2\gamma + g_y^2 \sin^2\beta \sin^2\gamma + g_z^2 \cos^2\beta$

Since H_o is parallel to the z-axis, the rotation about z by α doesn't appear in g_{eff}. If in addition there exists a hyperfine interaction, then with the A-tensor principal axes coincident with the g-tensor principal axes and with the magnetic field oriented as before, a diagonalized hyperfine Hamiltonian can be written,

$$\mathcal{H}_{hyp} = a_{eff} I \cdot S$$

where, $$a_{eff}^2 = \frac{1}{g^2}\left\{ g_x^2 A_x^2 \sin^2\beta\cos^2\gamma + g_y^2 A_y^2 \sin^2\beta\sin^2\gamma + g_z^2 A_z^2 \cos^2\beta \right\}$$ Equation 6

The case for g- and A-tensors not coincident is discussed in the appendix.

For the case of a polycrystalline or amorphous sample, the molecular orientations (hence g-tensor orientations) are random. The EPR simulations for this case must account for the fact that for each applied field, only molecules within a certain solid angle are resonating. An analytical expression for the number of spins resonating at a given applied field has been derived (24, 25) but this expression does not include the transition probability; therefore, the direct

stepwise integration over the solid angle is used for computer simulations. The effect of a rhombic g-tensor on transition probability has also been calculated and is given by (26),

$$\text{Prob} \quad \frac{g_x^2 g_y^2 g_z^2}{g^2} \left\{ \frac{\cos^2\gamma + \cos^2\beta \sin^2\gamma}{2 g_x^2} + \frac{\sin^2\gamma + \cos^2\beta \cos^2\gamma}{2 g_y^2} + \frac{\sin^2\beta}{2 g_z^2} \right\}$$

The EPR simulations used weight the signal intensities by both the solid angle and the anisotropic transition probability.

The ferredoxin EPR spectrum can be interpreted immediately in terms of its principal g-values; that is, the high and low field peaks and the crossing points are true g-values. This, however, is not always the case and confusion can arise if spectra are labelled incorrectly. This confusion can arise if there are large zero-field Hamiltonian terms, resulting in resonances which are not located at true g-values. For instance, a resonance at field H_i is often described as being due to a g_i-value, where $g_i = h\nu/\beta H_i$; if however, $h\nu = g_i \beta H_i$ + zero field term, g_i will not be the correct gyromagnetic ratio. The confusion can be resolved by repeating the EPR experiments at different fields; the resonant frequency for the field dependent terms (e. g. Zeeman interaction) will move linearly with H_o while the zero-field and hyperfine resonances will remain unchanged.

D. Electron Nuclear Double Resonance (ENDOR) (27)

ENDOR is a spectroscopic technique developed to measure electron-nuclear hyperfine splittings. The measurement is performed by observing the change in the amplitude of an EPR signal with respect to the frequency of a nuclear transition induced by an applied radio frequency (rf) field. Thus one observes the change in a given $\Delta m_s = \pm 1$ transition signal due to a $\Delta m_I = \pm 1$ resonance. As this experimental procedure suggests, the instrument required to observe the ENDOR effect is simply an ordinary EPR spectrometer with the addition of a variable frequency rf field source at the sample (see the instrumental section). Although there will in general be many nuclear resonances induced during a typical rf frequency sweep, only those affecting the paramagnetic center will be detected. The most important nuclei are those having a hyperfine interaction with the unpaired spin; the mechanism for this case will be discussed below. A less frequent (it does occur for protons in data presented later) and less informative process is that due to more distant nuclei. These nuclei are polarized by the electron moment via spin-diffusion; when the nuclear transition is induced, the polarization is removed and the EPR signal is changed. This is observed as an ENDOR signal which occurs at the free nuclear Zeeman frequency. Data presented here will show this "distant" or "matrix" ENDOR only for protons.

The ENDOR effect (27) can best be understood by considering the simple case of $S = I = 1/2$, where in addition to the electronic

and nuclear Zeeman terms, there is a hyperfine interaction between the two moments. The resultant energies will be,

$$E_n = g\beta H m_s - g_n\beta_n H m_I + a m_s m_I \qquad \text{Equation 7}$$

where the hyperfine interaction is assumed isotropic and m_s, m_I take on values ± 1. Two $\Delta m_s = \pm 1$ EPR transitions are possible and the two nuclear transitions, $\Delta m_I = \pm 1$, occur at

$$E = h\nu_{\mp} = \frac{A}{2} \pm g_n\beta_n H$$

The energies for this simple case are shown in Figure 3 along with the equilibrium population differences. The population differences are determined by the Boltzmann distribution via the relaxation processes. The relative populations for states $|m_s m_I\rangle$ are

$$\frac{N(\frac{1}{2}, \pm\frac{1}{2})}{N(-\frac{1}{2}, \pm\frac{1}{2})} = \exp(-E_n/kT)$$

where E_n from Equation 7 is approximated $E_n = g\beta H$. This approximation results in two equally populated nuclear states for each electronic state. Thus the two $m_s = -1/2$ states have a population $1 + g\beta H/2 \equiv 1 + \Delta_e/2$ relative to the two $m_s = +1/2$ states having $1 - g\beta H/2 = 1 - \Delta_e/2$. If a weak EPR field, H_1, is applied at $h\nu = g\beta H \pm A/2$, the equilibrium populations are essentially unchanged and an rf field at $h\nu_+$ would not affect the EPR signal. However, if the EPR transition is saturated by making H_1 large enough to induce transitions fast with respect to the electronic relaxation rates, i.e. $\gamma H_1 > (T_1 T_2)^{-2}$, the state $|m_s m_I\rangle = |+\frac{1}{2}, +\frac{1}{2}\rangle$ will now have the same population (Fig. 3b) as states $|-\frac{1}{2}, \pm\frac{1}{2}\rangle$ while the populations

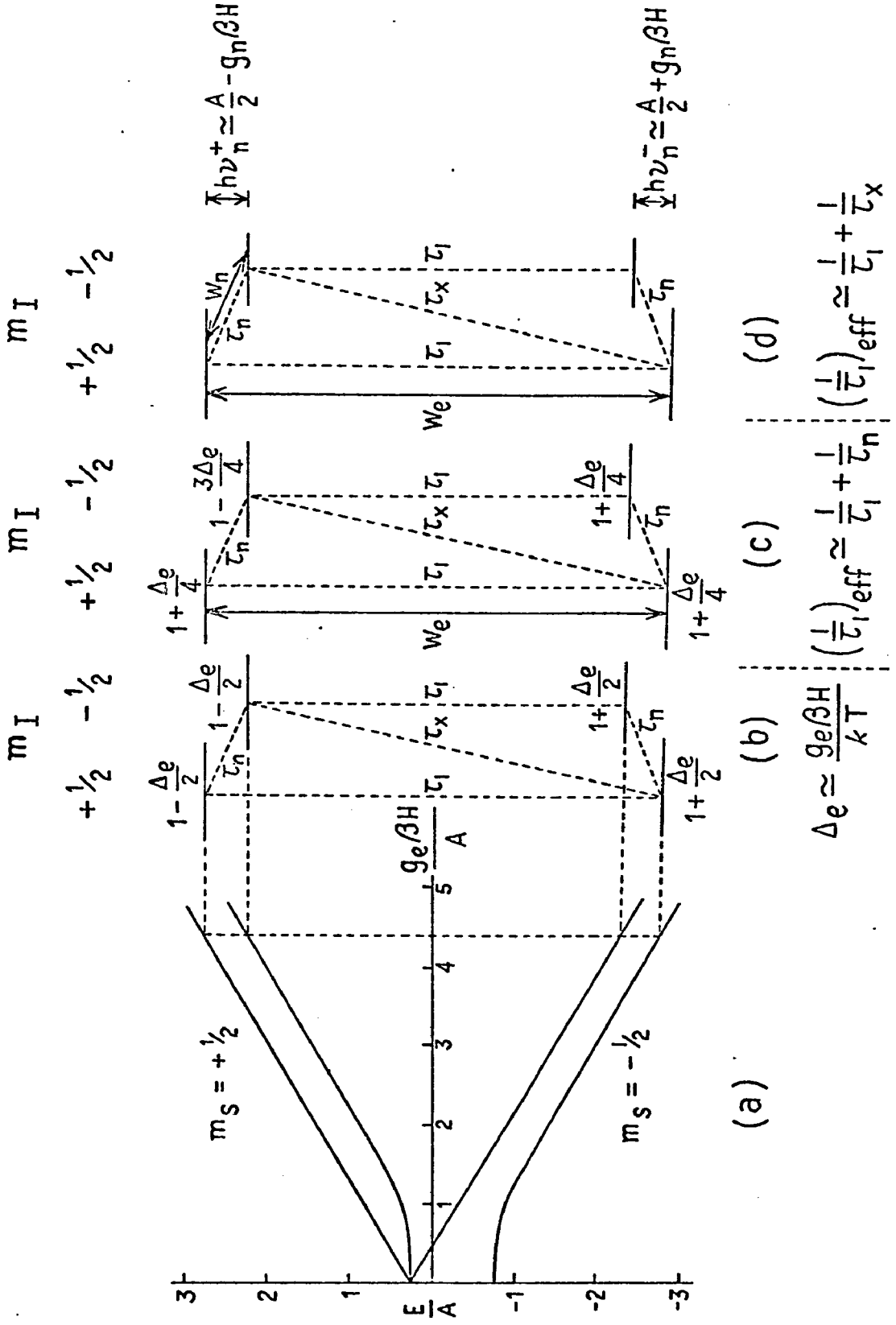


Figure 3. ENDOR Energy Levels

of states $\left|\frac{1}{2}, \frac{+1}{2}\right\rangle$ will differ by Δ_e. Since the two nuclear levels for $m_s = +\frac{1}{2}$ have the population difference the two electron spin levels had at equilibrium, the application of radiation $h\nu_+$ at a rate fast relative to the cross relaxation time, i.e. $\gamma H_{rf} > T_x^{-1}$, will cause the previously saturated EPR transition to absorb more power (Figure 3c). Thus if one monitors the EPR signal while varying the rf frequency, the signal intensity will increase only at the nuclear transition resonant frequency.

An alternative view (27) of the ENDOR process centers on the change in the net relaxation time when the nuclear relaxation rate, T_n, is replaced by an rf induced transition rate, W_n, which is fast compared to T_n and T_x. This results in a change in the effective rate (see Figure 3) from,

$$T_{eff}^{-1} = T_1^{-1} + (T_x + T_n)^{-1} \simeq T_1^{-1} + T_n^{-1}$$

to, $$T_{eff}^{-1} = T_1^{-1} + (T_x + W_n^{-1})^{-1} \quad T_1^{-1} + T_x^{-1}$$

Thus, the rf induced transitions (for a sufficiently rapid transition rate) change the effective relaxation rate by approximately T_1/T_x. If the rf induces transitions at a rate greater than T_n^{-1} but not greater than T_x^{-1}, the change in the effective rate is only T_1/T_n.

In this simple example the other nuclear transition, $h\nu_- = A/2 + g_n\beta_n H$ would not be seen since $T_{xx} = 0$. This is because cross relaxation processes involve dynamic Hamiltonian terms such as,

$$A_x S_x I_x + A_y S_y I_y = \frac{1}{4}(A_x + A_y)(S_+ I_- + S_- I_+) + \frac{1}{4}(A_x - A_y)(S_+ I_+ + S_- I_-) \qquad \text{Equation 8}$$

The two states $\left|\frac{1}{2}, -\frac{1}{2}\right\rangle \leftrightarrow \left|-\frac{1}{2}, \frac{1}{2}\right\rangle$ are connected by $S_+ I_-$, a "flip-flop" transition, so the probability for this transition will vary as the square of the matrix element (from Equation 8), i.e. $(A_x + A_y)^2$. Hence a relaxation time, T_x, can be defined as the inverse of that rate:

$$T_x^{-1} \propto (A_x + A_y)^2$$

Similarly for the other path, the transition $\left|\frac{1}{2}, \frac{1}{2}\right\rangle \leftrightarrow \left|-\frac{1}{2}, -\frac{1}{2}\right\rangle$ a "flip-flop" transition, is connected by $S_+ I_+$ terms, hence,

$$T_{xx}^{-1} \propto (A_x - A_y)^2$$

Thus the contribution to T_x is related to the average value of the other two hyperfine values, while T_{xx} is related to the anisotropy. Since the ENDOR signal is proportional to T_1/T_x or T_1/T_{xx}, the two lines $h\nu_+$ will not in general have the same amplitude. Such an effect will be seen in later data. However, the differences observed are not as great as expected from the A-tensor anisotropy.

The ENDOR requirements alluded to above can be summarized as (28),

$$T_x \geq \sqrt{T_1 T_2} \geq (\gamma H_1)^{-1} \simeq (\gamma_n H_{rf})^{-1} \qquad \text{Equation 9}$$

The first relation, $T_x \geq T_1 T_2$, states that the EPR line must not be homogeneously broadened, i.e. that the line width must not be dominated by other spin-spin relaxation effects. Since EPR and ENDOR

have the same intrinsic line width ($1/T_2$), ENDOR is useful only for inhomogeneously broadened EPR lines. The second part of Equation 9, $T_1 T_2 \geq (\gamma_e H_1)^{-1}$ states the condition for EPR saturation. Since T_1 changes rapidly with temperature, this condition can be met by varying the temperature and/or microwave power. The final relation, $\gamma H_1 \approx \gamma_n H_{rf}$, states that for the rf to sufficiently change the populations, it must induce transitions at a rate comparable to the electron transition rate. For the proteins of interest, these conditions require low temperatures (10-20°K), high microwave fields (H_1 = 0.1 gauss), and high rf fields (H_{rf} = 10 gauss).

Although ENDOR's sensitivity is less than that of EPR by the factor T_1/T_x, it is comparable to the sensitivity of Mossbauer spectroscopy, and considerably better than that of NMR and magnetic susceptibility. ENDOR is most useful, however, when EPR lines are inhomogeneously broadened (e.g. by hyperfine interactions or "g-strain"); in this case ENDOR hyperfine resolution will be considerably improved over EPR. To see this, consider a system of N sets of n identical nuclei with spin I. For an EPR experiment, the number of lines at each g-value would be $\prod_{i=1}^{N} (2 n_i I_i + 1)$ while for ENDOR the corresponding number would be simply 2N. Since both EPR and ENDOR have the same intrinsic line width, $1/T_2$, the density of lines (lines/unit energy) is considerably decreased.

For amorphous samples with anisotropic g-tensors, ENDOR has the additional unique advantage of selecting molecules with a particular orientation via the anisotropic g-tensor. For example, when the g_z EPR signal is saturated, only molecules with their z-axes oriented parallel to the H_o field will resonate. When the rf frequency is swept, the EPR signal will change (ENDOR will occur) only when the rf frequency corresponds to the A-tensor component. In this way the angular variation of the A-tensor relative to the g-tensor can, in principle, be determined. Thus as long as the g-tensor is anisotropic, one does not need a single crystal to determine the A-tensor; a single crystal is technically more convenient and requires less sample since all the molecules will resonate collectively.

Unfortunately, ENDOR is limited first of all by the 100-fold decrease in sensitivity since this requires a corresponding increase in sample concentration. For biological samples, a factor of 100 is generally serious, and often adequate concentrations cannot be obtained. Secondly, the ENDOR conditions are not always easily met; many interesting biological problems can't be studied by present ENDOR spectrometers due to the limited magnitude of H_{rf}. Finally, even though the resolution is greater for ENDOR than for EPR, biological molecules often have resonances (especially protons and nitrogen nuclei) which obscure the resonance of interest.

Figures 4a and b show the two classes of ENDOR problems which occur. Figure 4a shows a typical spectrum for A/2 greater than the nuclear Zeeman frequency; the pair of ENDOR lines originating from the nucleus with any spin I is centered at A/2 and is split by twice its nuclear Zeeman frequency. Figure 4b shows the case for A/2 less than the nuclear Zeeman frequency; the pair of lines is centered at the nuclear Zeeman frequency and is split by the hyperfine interaction. Case 4a is typical of iron hyperfine while 4b is typical of protons.

E. Mossbauer Effect (29, 30, 31)

The Mossbauer effect is a form of resonant spectroscopy which involves transitions between the ground and excited states of nuclei, iron nuclei for the cast of interest. The magnitude of transition from the ground to the first excited state for the "free" ^{57}Fe case is 14.41 kev, but shifts and splittings of this single transition occur due to interactions with the irons' electromagnetic environment. The observed energy splittings all occur within a range of approximately 3×10^{-7} eV for the two-iron ferredoxins. The Mossbauer experiment is simply a measurement of the percent gamma ray transmission as a function of gamma ray energy, the energy being scanned through the region 14.41 kev $\pm$ 3×10^{-7} eV.

The Mossbauer effect spectrometer (29) consists of a gamma ray source (^{57}Co diffused into a platinum matrix), the absorbing iron sample, and a gamma ray counter. The variation in gamma

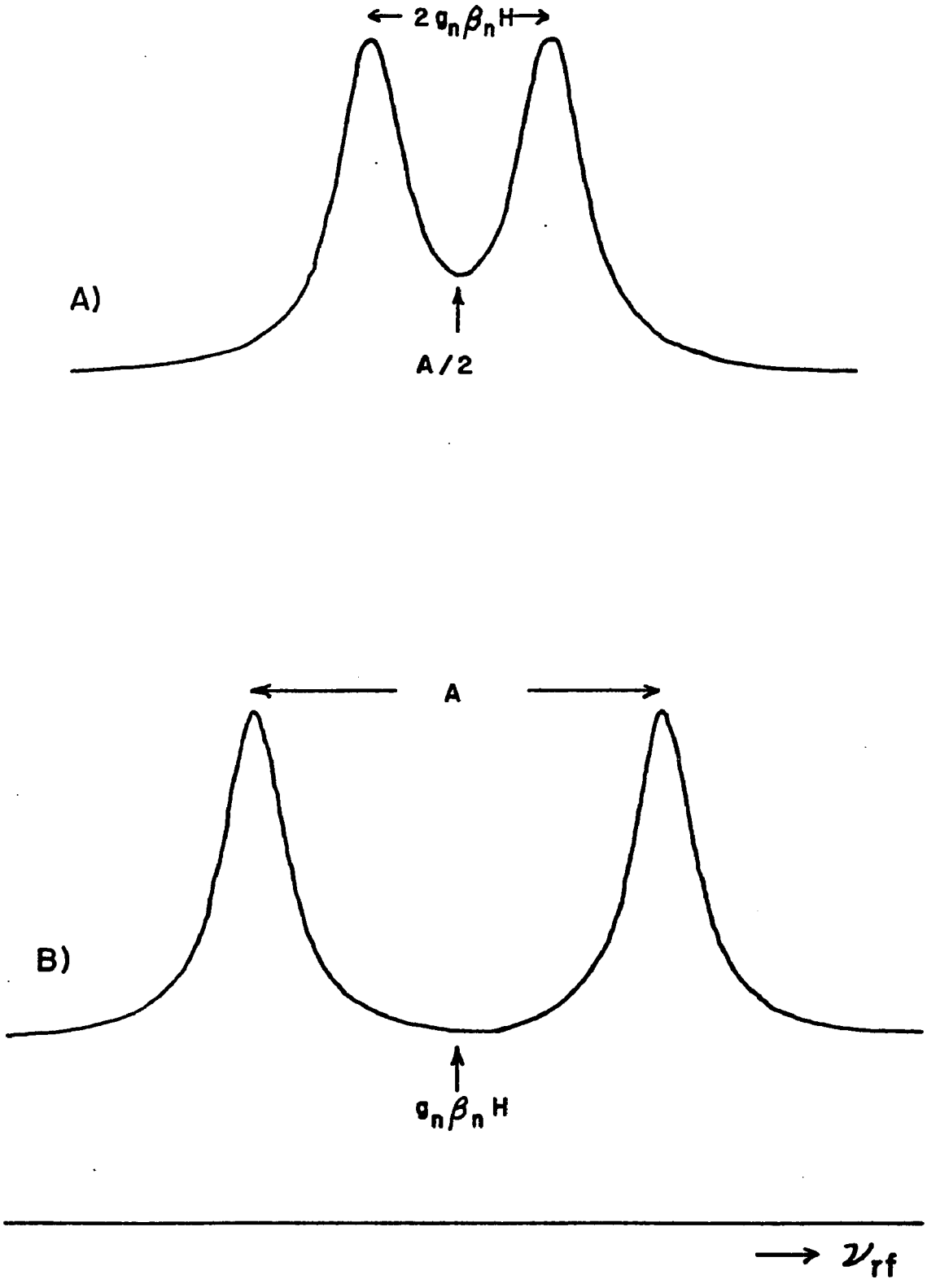


Figure 4. Typical ENDOR Spectra

ray energy is provided by moving the source relative to the absorber and counter at a velocity v; this results in a relativistic Doppler energy shift given by $E = E_\gamma (1 + v/c)$. The counter output is stored in a multichannel analyzer as a function of the instantaneous source velocity. The resulting spectrum is a plot of percent gamma ray transmission versus the Doppler energy shift (in mm/sec, where 1 mm/sec $\simeq 5 \times 10^{-6}$ eV).

The perturbations on the ^{57}Fe nuclear ground-excited state transition due to electrostatic interactions can be expressed (30) using the nuclear charge density, $\rho_n(r)$, and a multipole expansion of the electrostatic potential, V(r), due to iron and ligand electrons; this potential obeys Poisson's equation, $\nabla^2 V(r) = -4\pi \rho_e(r)$ where $\rho_e(r)$ is the electron charge density. The energy of the nuclear charge distribution in this potential is,

$$E = \int \rho_n(r)\, V(r) d^3r \qquad \text{Equation 10}$$
$$= V(o)\int \rho_n d^3r + \frac{\partial V}{\partial x_i}\int \rho_n x_i d^3r + \frac{1}{2!}\left(\frac{\partial^2 V}{\partial x_i \partial x_j}\right)\int \rho_n x_i x_j d^3r + \ldots$$

The first term is due to the nuclear point charge and since it simply shifts all energy levels, it is not of interest here. The second term vanishes because ρ_n is an even function of position. The third term of the multipole expansion is an interaction describable by the product of two symmetric, third order tensors. The physical origins of the interaction is more easily understood, however, if it is divided into the product of two scalars, represented by the term E_R, and the product of two traceless tensors, represented by E_Q (30). E_R results

from the fact that the nucleus has a finite size and is nonzero if the electron density within the nucleus is nonzero. Hence it is due to that part of the electrostatic potential which can be written,

$$\nabla^2 V = -4\pi \rho_E(o)$$

where $\rho_E(o) = e|\psi(o)|^2$

The resulting energy, E_R, can be written,

$$E_R = -\frac{2}{5}\pi Z e^2 R^2 |\psi(o)|^2$$

where $|\psi(o)|^2$ is the electron density at the nucleus, hence the electron's s-state character, and R^2 is the mean nuclear charge radius, here assumed to be the radius of a sphere. In general, the nuclear charge radius is different for the nuclear ground and excited states, hence a shift in both the gamma ray source energy and the absorber energy will occur. This shift, the <u>isomer shift</u>, is given by,

$$\text{I.S.} = \frac{4\pi}{5} Z e^2 \left\{ |\psi^{(o)}_{\text{absorber}}|^2 - |\psi^{(o)}_{\text{source}}|^2 \right\} \left\{ R^2_{\text{excited}} - R^2_{\text{ground}} \right\}$$

The isomer shift is generally not calculable and only high spin-ferrous iron can be uniquely identified by the isomer shift data. The isomer shift is determined from the experimental spectra visually simply as a shift in the "center of gravity" of the absorption lines.

The term E_Q, also from the third element of the multipole expansion, can be written as the product of two traceless tensors (30),

$$E_Q = \frac{1}{2} V_{ij} Q_{ij}$$

where V_{ij} ($V_{ij} \equiv \frac{\partial^2 V}{\partial x_i \partial x_j}$) is the electric field gradient tensor due

to electrons outside the nucleus (since $\nabla^2 V = tr V_{ij} = 0 = -4\pi \rho_E(o)$) and Q_{ij} is the nuclear quadrupole moment (nonzero for $I > 1/2$; $I = 0$ for the ground state iron; $I = 3/2$ for excited state iron). This quadrupole interaction can be written for its principal axis frame in terms of an asymmetry parameter, $\eta \equiv (V_{xx} - V_{yy})/V_{zz}$ and $V_{zz} \equiv eq$. If $D \equiv eqQ/4I(2I - 1)$, (Q = nuclear quadrupole moment) and $E \equiv \eta D$, then the quadrupole splitting can be written,

$$Q.S. = \frac{e^2 qQ}{2}(1 + \eta^2/3)^{1/2} = 6\ D(1 + \eta^2/3)^{1/2}$$

for the Hamiltonian,

$$\mathcal{H}_{Q.S.} = D[3I_z^2 - I(I+1) + \eta(I_x^2 - I_y^2)]$$

Table 2 shows the values of q and η as calculated (32) for the d-orbitals. A comparison of the observed q and η with the calculated values in Table 2 allows some conclusions about the electron orbital, but a unique determination will clearly not always be possible. Note that both the magnetic hyperfine interaction (Table 1) and the electrostatic quadrupole interaction (Table 2) determine the electron orbital and hence must agree. The quadrupole interaction for zero applied field results in a pair of lines split by Q. S. and centered at the isomer shift.

Since one is measuring nuclear transition energies, the nuclear magnetic interactions will also affect these energies. The two of principal interest are familiar from EPR and ENDOR; they are the electron-nuclear hyperfine interaction and the nuclear Zeeman

Table 2

Eta and q for the d-Orbitals

d-orbital	q	n
$d_{x^2-y^2}$	$4/7 \langle r \rangle^{-3}$	0
d_{z^2}	$-4/7 \langle r \rangle^{-3}$	0
d_{xz}	$-2/7 \langle r \rangle^{-3}$	+3
d_{yz}	$-2/7 \langle r \rangle^{-3}$	-3
d_{xy}	$4/7 \langle r \rangle^{-3}$	0

interaction. The total Mossbauer Hamiltonian of interest here is the sum of four terms,

$$\mathcal{H} = \mathcal{H}_{I.S.} + \mathcal{H}_{Q.S.} + S \cdot A \cdot I - g_n \beta_n H \cdot I + g \beta H \cdot S$$

Mossbauer effect spectroscopy is useful for the iron-sulfur proteins because it can measure at the nucleus, quantities related to the electron density, the magnetic fields, and the electric field gradient. Each of these can be related to the iron atoms' electronic and structural environment. Mossbauer also has good resolution and selectivity. The resolution results from the narrow gamma ray intrinsic linewidth ($\sim 10^{-8}$ eV) relative to the energy differences ($\sim 10^{-7}$ eV). The selectivity results from the fact that the cross section for iron resonant absorption in the gamma ray energy range is three orders of magnitude greater than for other background processes. An important advantage is that Mossbauer does not require paramagnetism and hence it is useful for both the oxidized and reduced ferredoxins. Both ENDOR and Mossbauer spectroscopy require approximately one micromole of ^{57}Fe.

Mossbauer spectroscopy is basically limited by the fact that multiparameter computer fits are required to analyze the data. In order to uniquely fit the Mossbauer data, one must determine the electronic g-values with EPR, the magnitudes of the hyperfine tensors, and the relative orientations of the hyperfine tensors with respect to the g-tensor. The Mossbauer simulations will, with their fixed

parameters, determine the quadrupole splitting, isomer shift, asymmetry parameter, and the signs of the hyperfine tensors.

CHAPTER 4

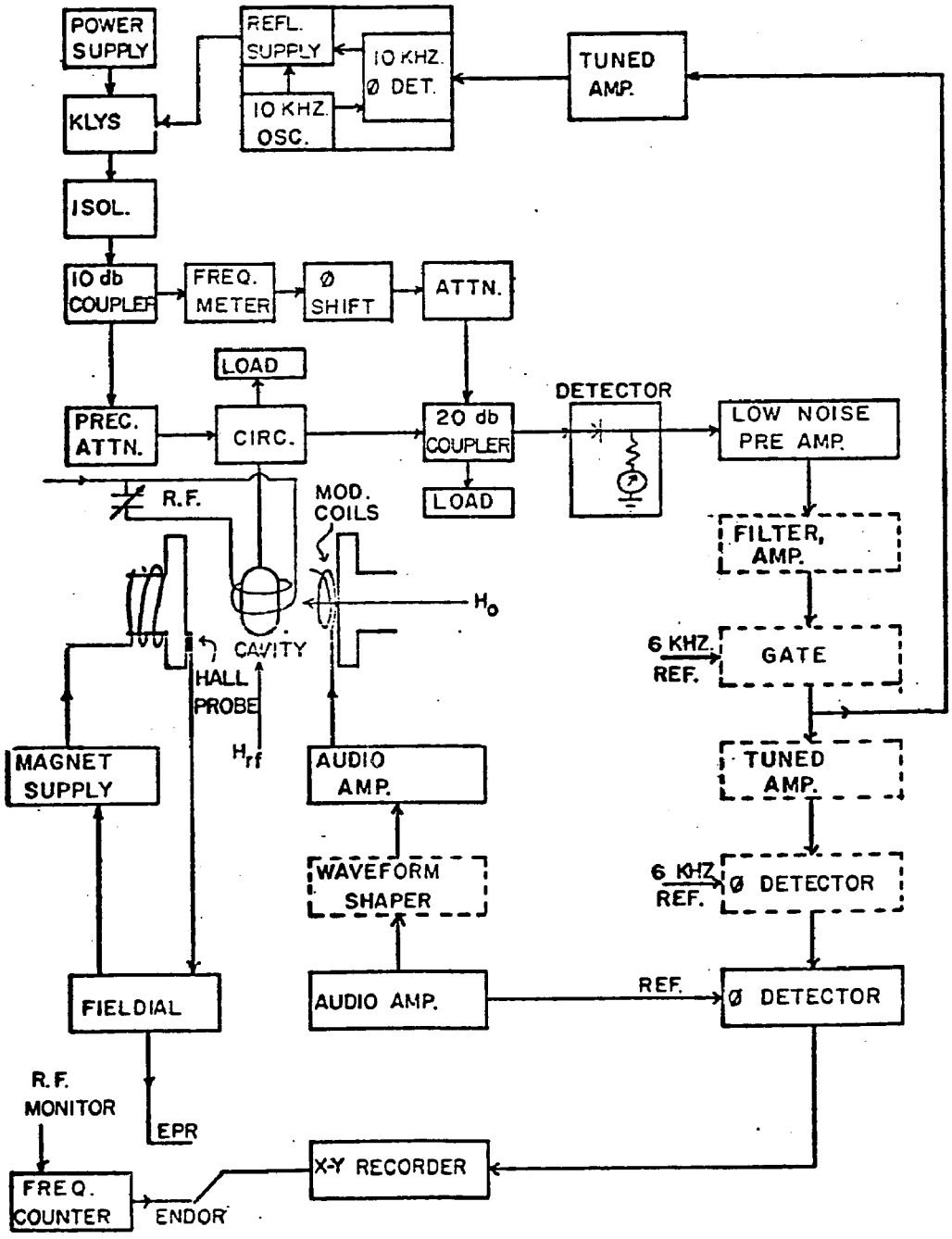
EPR AND ENDOR INSTRUMENTATION

For all EPR measurements, a modified commercial Varian V-4500 EPR spectrometer was used. For X-band (9 GHz) EPR and ENDOR, a homemade microwave bridge with separate bias arm was employed; for K-band (35 GHz) EPR, the Varian V-4561 bridge was used. The resonant cavity employed for X-band EPR is the Varian V-4531 multipurpose rectangular cavity operating in the TE_{012} mode, for K-band EPR a cylindrical Varian V-4566 cavity was used in the TE_{011} mode, and for ENDOR at X-band the cylindrical Varian V-4533 cavity was used in the TE_{011} mode.

The additions required to adapt an EPR spectrometer for ENDOR are shown in the dotted regions in Figure 5. These additions can be separated into two groups: a) variable frequency rf (radio frequency) generation, amplification, and transmission to the sample (see Figure 6) and b) changes in the signal channel to discriminate against rf noise. The ENDOR spectrometer was built by John Fritz and is described in greater detail elsewhere. Only minor modifications have been made for this work.

A. ENDOR Rf Source

The basic rf oscillator is voltage variable over a frequency range 11 MHz to 40 MHz; up to three frequency divide-by-two circuits can be selected, making 1.3 MHz the lowest available frequency. In order to provide large rf fields at the sample without excessive



EPR/ENDOR BLOCK DIAGRAM

Figure 5. Block Diagram for EPR/ENDOR Spectrometer

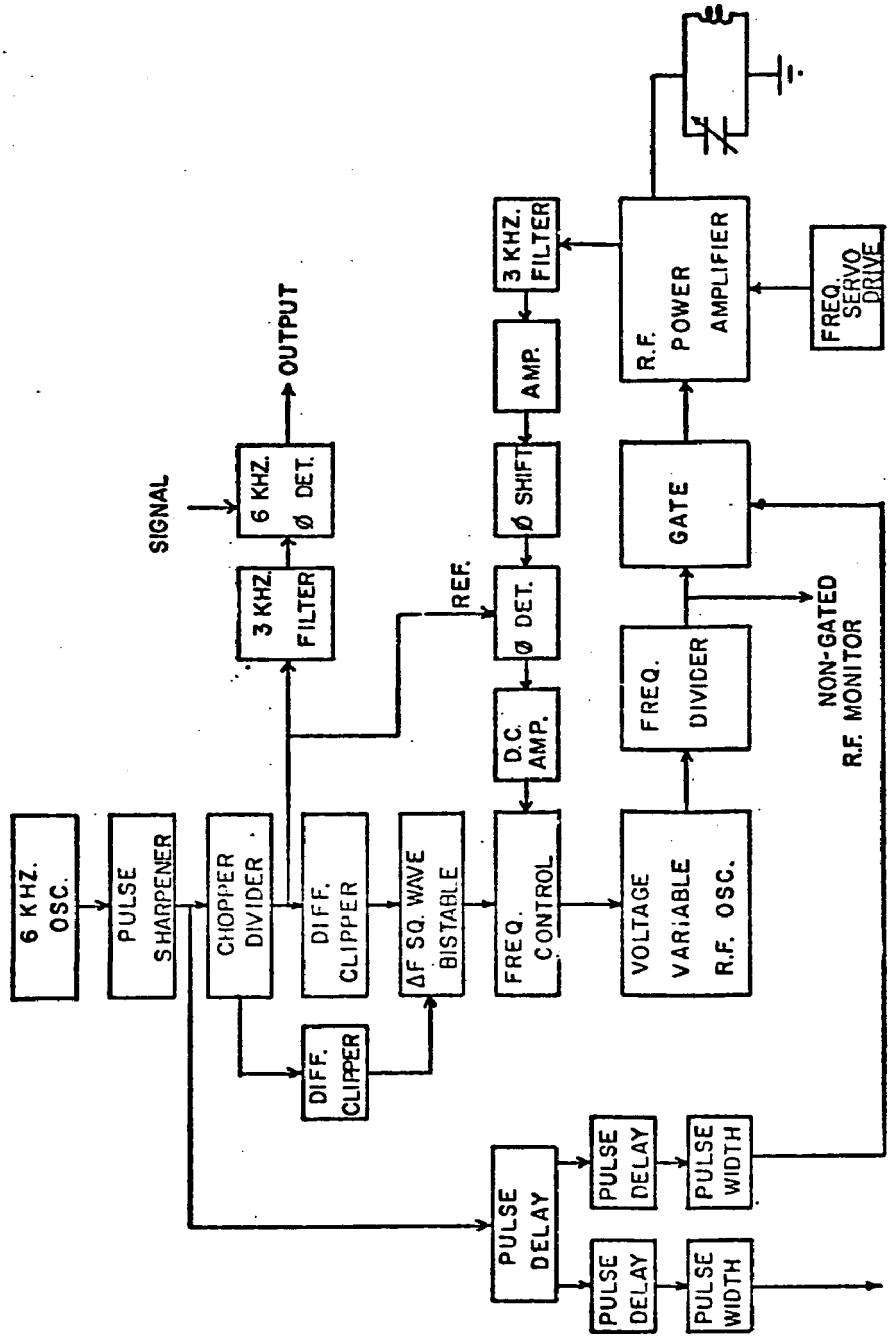


Figure 6. Block Diagram for ENDOR RF Section

cavity heating, the rf is gated on only 10% of the time. A 6 kHz sine wave is generated, rectified, and shaped to drive the gate open for 18 microseconds at a 6 kHz rate. The pulsed rf is broadband amplified to a voltage of approximately 2 volts (peak-to-peak) and sent to the final tuned amplifier.

The final amplifier is capable of 10 kW pulsed (10%) or 1 kW continuous wave operation; it has only been used as a pulse amplifier. It consists of a broadband transistor (2N1143) stage followed by three class C vacuum tubes (#s 6146, PR125, and PR1000) tuned stages. Four frequency ranges (each tuneable over a 2.5:1 frequency range) allow operation from 1.4 MH_z to 40 MH_z. The first tank circuit couples the 6146 to the EIMAC PR125 driver, and the second couples the driver to the final PR1000. The output of the PR1000 is ac coupled through a blocking capacitor to the final tank circuit via a 5-tap impedance-matching autotransformer. The final tank circuit consists of a variable (50-3000 pf. 5 kV; or 200-5000 pf 3 kV) vacuum capacitor and the coil (with 1, 2, 4 or 8 turns) at the microwave cavity; the rf coil must be oriented perpendicular to the dc field to minimize rf field modulation. The highest frequency coil (11-56 MHz) is a single loop which uses the top and bottom end-plates of the microwave cavity and is completed with a copper strap connecting them. For frequencies 3-21 MHz, coils (with 2 or 4 turns) potted in epoxy were used; for frequencies 1.3-12 MHz, an 8-turn open-air coil was used. Rotating rf fields of approximately 5 gauss

were typically used although fields up to four times this magnitude can be obtained with the high frequency coil. Heat dissipation and capacitor high voltage breakdown are the two major limitations; the amplifier is operated typically at 15% of capacity.

The tuned amplifier is frequency swept by a stepping motor which drives the three identical ganged, variable (air) capacitors; two of the capacitors are for the coupling tank circuits and a third tank circuit is for tracking the voltage variable oscillator (vvo) to the amplifier resonant frequency; all three tank circuits are initially aligned to resonate at the same rf frequency. The third tank circuit is used as a phase discriminator where the frequency modulation is provided at the voltage variable rf oscillator by a 3 kHz square wave. This square wave frequency modulates the ν_{rf} so that alternate rf pulses are at frequencies ν_{rf} and $\nu_{rf} + \delta f$; δf is approximately 15 kHz, that is, small relative to the tuned amplifier bandpass and small relative to the ENDOR linewidths. When the motor drives the ganged capacitors, thus changing the amplifier resonant frequency, a 3 kHz signal (superimposed on the 6 kHz signal) is obtained from the tracking tank circuit which, when phase-detected at 3 kHz, provides a dc voltage to the vvo, forcing it to follow the amplifier frequency. The pulses to the stepping motor drive are adjusted such that $\Delta\nu_{rf}/\Delta t \simeq 30$ kHz/sec and is essentially constant for all frequency sweeps.

The final tank circuit is manually tracked by maximizing the rf voltage across the tank circuit. The rf power is kept approximately constant (within 10%) by simultaneously adjusting the PR 1000 plate supply to maintain a tank circuit voltage proportional to the rf frequency; the rf power for various runs is, however, consistent to within a few percent; for difference spectra, consistency is more important than constancy.

B. ENDOR Signal Channel

The signal channel changes (33) from EPR to ENDOR (dotted regions in Figure 5) result from the need to phase detect at the rf pulse repetition rate and the need to discriminate against rf noise and rf-induced baseline shifts. The latter two problems are remedied by field modulation, hence the 6 kHz phase detector must be followed by a second phase detector at 47 Hz, the field modulation frequency.

In order to avoid signal channel noise (primarily diode and klystron noise) during the rf off-time, a gate is placed early in the signal channel as shown in Figure 5. This gate is synchronized with the 6 kHz rf pulse repetition rate and, like the pulse, has a 10% on-time. Thus, although the pulsed-ENDOR signal intensity has decreased by a factor of 10 relative to cw ENDOR, gating the noise during the rf off-time decreases the noise by $\sqrt{10}$, hence only a factor of approximately 3 in signal to noise is lost. To see detector noise (the minimum noise possible) above gate noise, an amplifier must precede the gate (33); the total gain before the gate is

approximately 10^3. Another noise problem can be introduced by the gate if noise at all frequencies is gated and allowed to reach the phase detectors. For instance, if noise at a low frequency, ν_1, is gated at ν_2, then the gate output will have noise at frequencies $n\nu_2 \pm \nu_1$. Since the phase detector at the gate frequency (6 kHz) must pass 6 kHz $\pm$ 47 Hz, it will also pass noise at ν_1 ($\nu_1 < 50$ Hz) after it is gated at 6 kHz; this is called the up-conversion of noise (33). Some down-conversion of high frequency noise by the gate is possible, but it is a much smaller effect. To prevent both the up- and down-conversion of noise, a passive filter is placed before the gate whose band width (5-100 kHz) passes a 6 kHz pulse without serious attenuation of any of its high frequency components. The gate is followed by a 6 kHz tuned amplifier which drives the 6 kHz phase detector; the time constant (0.003 sec) is set to pass the 47 Hz field modulation. The 6 kHz phase detector is followed by a 47 Hz phase detector (T = 1 sec) whose output drives the y-axis of the chart recorder; both phase detectors are EMC Model RJB, and the recorder is a HP/Moseley 7035B. The x-axis drive of the recorder is derived from the ungated rf signal through a digital frequency counter (HP 52456) and a digital-to-analog converter (HP 580A).

C. ENDOR Field Modulation

For ENDOR of amorphous samples with large g- and A-tensor anisotropies, sinusoidal field modulation samples a distribution of

g-values ($\Delta g = h\nu/\beta\Delta H_{mod}$) and hence A_i values, resulting in complex derivative spectra with broadened linewidths. In this experiment, such problems were avoided by using square wave field modulation large enough to sample only one EPR field while the other half cycle of the square wave is off the EPR line. Since the ferredoxins have a 400 gauss wide EPR spectrum, 200 gauss field modulation was sufficient to reach all points on the EPR line. Square wave field modulation has the added advantage of presenting absorption ENDOR spectra.

In practice a good square wave of such magnitude was difficult to obtain. A compromise had to be reached between available audio power, desired field strength, sharpness of the square wave, and the problem of a voltage spike at the audio amplifier output accompanying the falling field. The coils used (200 turns, #24 wire) had an inductance of 1 mh and a resistance of 3 ohms; this resulted in a rise time of $\sim$0.4 msec; a series resistance of 3 ohms was used to halve the rise time at the expense of doubling the input power. The 47 Hz signal was generated by a HP 209A sine/square wave generator (the sine wave is used for the 47 Hz phase detector reference) and each coil of the Helmholtz pair was driven by one channel of an (Heathkit AA121) 80 watt stereo amplifier. A problem more serious than the rise time was the "ramp" in the square wave at the amplifier output due to the interstage coupling capacitors. This was avoided by adding a sawtooth (of the

proper sign) to the square wave at the amplifier input and adjusting the relative proportions until a quite flat square wave was observed across the 3 ohm resistor. Another check on the squareness of the field modulation is made by doing ordinary EPR (i.e. sweep H_o) with a strong, narrow (BDPA, α,γ-bisdiphenylene β-phenyl allyl, $C_{33}H_{21}\cdot C_6H_6$, 0.4 gauss line width) sample but using only 47 Hz field modulation; this requires that the Tektronix preamp output be connected directly to the 47 Hz phase detector. A perfectly flat, symmetrical, fast rise time square wave modulation of 200 gauss would result in two narrow (1/2 gauss), equal - but of opposite sign - absorption EPR lines separated by 200 gauss. The observed result was a line of 3 gauss width for a point sample (at the center of the cavity), and a 6 gauss width for a sample distributed along the height of the cavity. This demonstrates that there is some rounding of the square wave, the rise time is approximately 1 msec, and the modulation field is distributed along the sample axis. None of these findings was surprising, and a 6 gauss (out of 400 gauss) smearing was judged acceptable, because even the most anisotropic signals only move approximately 0.2 MHz in 6 gauss while the linewidth is at least 0.5 MHz.

D. ENDOR Temperature Control

The ENDOR experiment of interest required that the sample temperature be lowered to 10-20°K. This was achieved by boiling liquid helium in a 30 liter supply dewar (using a 20 watt, 1000 ohm

resistor powered by a Variac) and transferring the cold gas through a rigid vacuum-jacketed transfer tube (34) to the quartz sample dewar. The transfer tube mates with the dewar ground glass ball-joint and the dewar fits into the microwave cavity along the cylindrical axis. The sample temperature is varied by changing the boil-off rate, that is, changing the voltage dropped across the 1000 ohm resistor. The temperature is measured using the resistance versus temperature characteristic of 1/8 watt carbon resistor calibrated at three temperatures (room temperature, liquid nitrogen, and liquid helium); this resistor is placed just below the sample (see Figure 7) and the resistance is measured on a HP 410 VTVM. The temperature was generally constant within $\pm$ 0.5^{o}K.

Temperature control to within $\pm$ 0.1^{o}K was necessary for the ferrous iron ENDOR difference spectra and was achieved by constructing a feedback temperature controller. The controller (see Figure 8) uses a resistance bridge with the temperature sensing resistor in one arm and a precision decade resistance box in another. If the bridge becomes unbalanced due to a temperature change, a dc voltage is developed which, when amplified, turns on or off a power transistor which regulates the current to a 35 ohm nichrome heater coil located below the sample and temperature sensor (Figure 7). In practice, the boil-off rate is adjusted to maintain some heater current (0.2 ma) so that the heater always warms the gas approximately

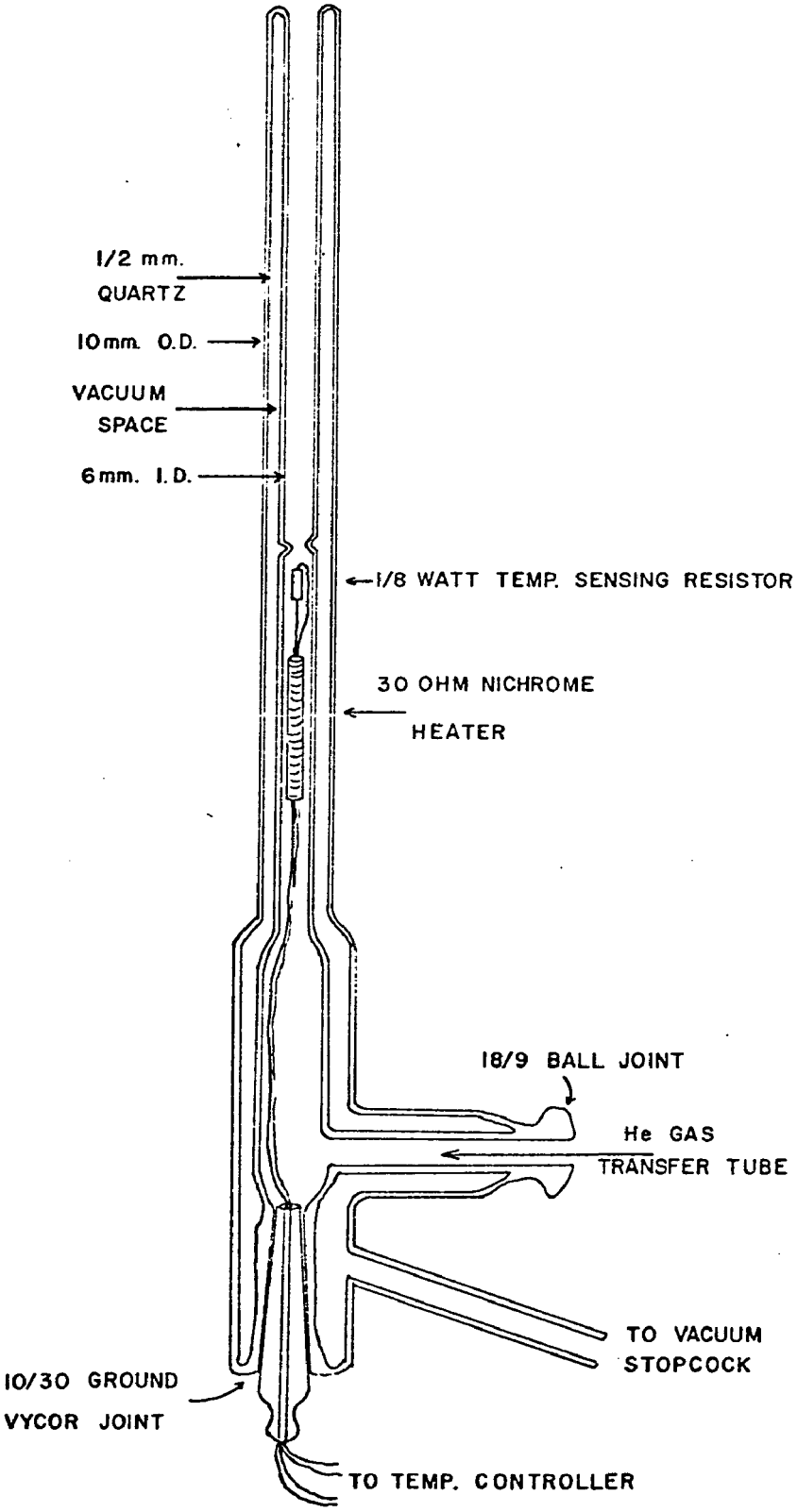


Figure 7. Sample Dewar Assembly

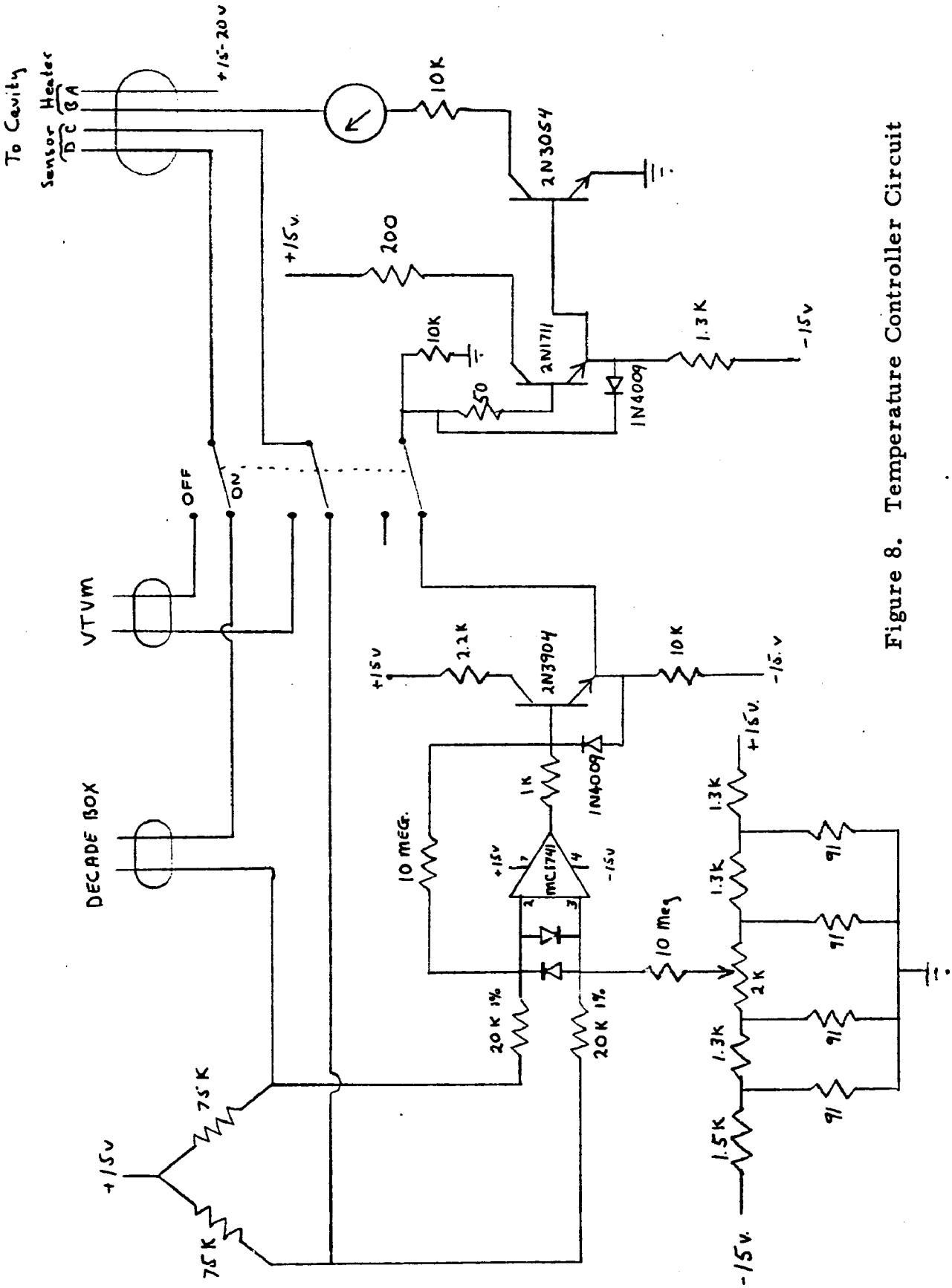


Figure 8. Temperature Controller Circuit

1°K. The heater current holds the temperature to the value set on the decade box with a time constant of approximately 0.5 second.

Low temperature (8-15°K) operation with reasonable helium consumption rates (3 liter/hr at 13°K) is possible only if the sample dewar is re-evacuated before lowering the temperature to remove the helium gas which diffuses through the quartz dewar wall; a stopcock is provided for this purpose. The temperature instability and helium consumption were also lessened by placing a nylon cap over the sample and dewar top. This cap - when frozen in place - provides a cold chamber around the top of the sample, thereby reducing the temperature gradient along the sample. The helium in the cap is allowed to pass out a side port, through a rubber hose, and blows on the transfer tube-sample dewar connection. A plastic bag is placed around the bottom of the sample dewar to keep the junction region cold and relatively frost free.

E. ENDOR Operating Procedure

Although the ENDOR conditions are described in the theoretical section, the actual conditions are determined experimentally. The first step is to determine with EPR the microwave power saturation dependence of the sample and how this dependence varies with temperature; this step will also determine the amount of sample required since the ENDOR sensitivity is less than the EPR sensntivity by approximately a factor of 100. Since the available rf power probably will not saturate the nuclear transition, the full power is

used (5 gauss in the rotating reference frame). The next step is to look for ENDOR signals at various temperatures and microwave powers such that the EPR signal is maximized. Generally one knows the nuclei which are expected to have ENDOR signals (from the chemical and EPR data) so the rf frequency would then be swept in the expected region. Once an ENDOR signal is found, it is necessary to optimize the temperature and microwave power operating conditions. If difference spectra with two different isotopes are necessary (as for ferrous iron in the ferredoxins) the difference amplitude may maximize under different conditions than the total ENDOR amplitude due to differing relaxation times for the different contributing nuclei.

To take difference ENDOR spectra, one also needs to be able to correctly scale the relative observed amplitudes for the two samples. The obvious approach is to take ENDOR data on both samples and to adjust the relative gains to coincide with the sample concentrations as determined by double integration of the EPR spectra. Unfortunately, even with temperature control and "identical conditions", ENDOR intensity variations of 10-15% over a few hours are not uncommon; presumably, most of these variations are caused by temperature and gas flow variations in spite of the controller. Since the difference signals may be on the same order as the fluctuations, reliable difference data requires that one set the relative gains empirically for each pair of runs by forcing the amplitudes to be equal at some point where there is no ENDOR signal. The location

of such a point must also be determined empirically starting from a region of zero total ENDOR signal. Since the frequency sweep range is limited by both the final tank circuit and the amplifier range, one must be certain to have at least one region of zero difference signal, otherwise the gains cannot be adjusted for that sweep range; the same gain settings in one sweep range cannot confidently be used in another. Also, if the difference signal is not zero at both ends of the sweep range, one must sweep adjoining instrument ranges and try to match the difference amplitude at the overlap region. This is generally difficult to do quantitatively since the different rf coils result in different field strengths and field distributions at the sample. Since the contributing amplitudes are varying as H_{rf}^{n} where $1 \leq n \leq 2$ (n for all nuclei needn't be the same), one must settle for an estimate of the shape. Accurate determination of the zero difference region can be made, however, and these regions were used as the major criterion for computer simulations. Finally, amplitude variations with time during and between runs requires that many spectra be taken, and those with the greatest internal consistency used.

CHAPTER 5

RESULTS

A. Magnetic Susceptibility Results

The static magnetic susceptibility of ferredoxin was measured on an Iizuka-Kotani (35) torsion balance. This instrument does not provide an absolute susceptibility value, but rather measures the variation in susceptibility with temperature (77-270^{o}K). The variation in the susceptibility with temperature is very small relative to the solvent and protein diamagnetism; the sample cuvette also has a temperature-dependent susceptibility which is comparable with the protein paramagnetism. In practice the experiment must be repeated until reproducible data is obtained and then this data is assumed correct. The problems inherent in the measurement must be kept in mind so that the data is not used with excessive confidence. This procedure is reasonable since experimental data does agree with the susceptibility calculated for a standard.

Figure 9 (solid curve) shows the results for the oxidized ferredoxin. The experimental data has been corrected for the susceptibility of the cuvette and the ordinate has been expressed in esu units per mole of protein. The fact that the curve is asymtotically approaching a horizontal line at low temperatures means that at these temperatures the protein is diamagnetic. As the temperature is increased, the sample becomes increasingly paramagnetic. This behavior is characteristic of exchange coupled electron spins which at high

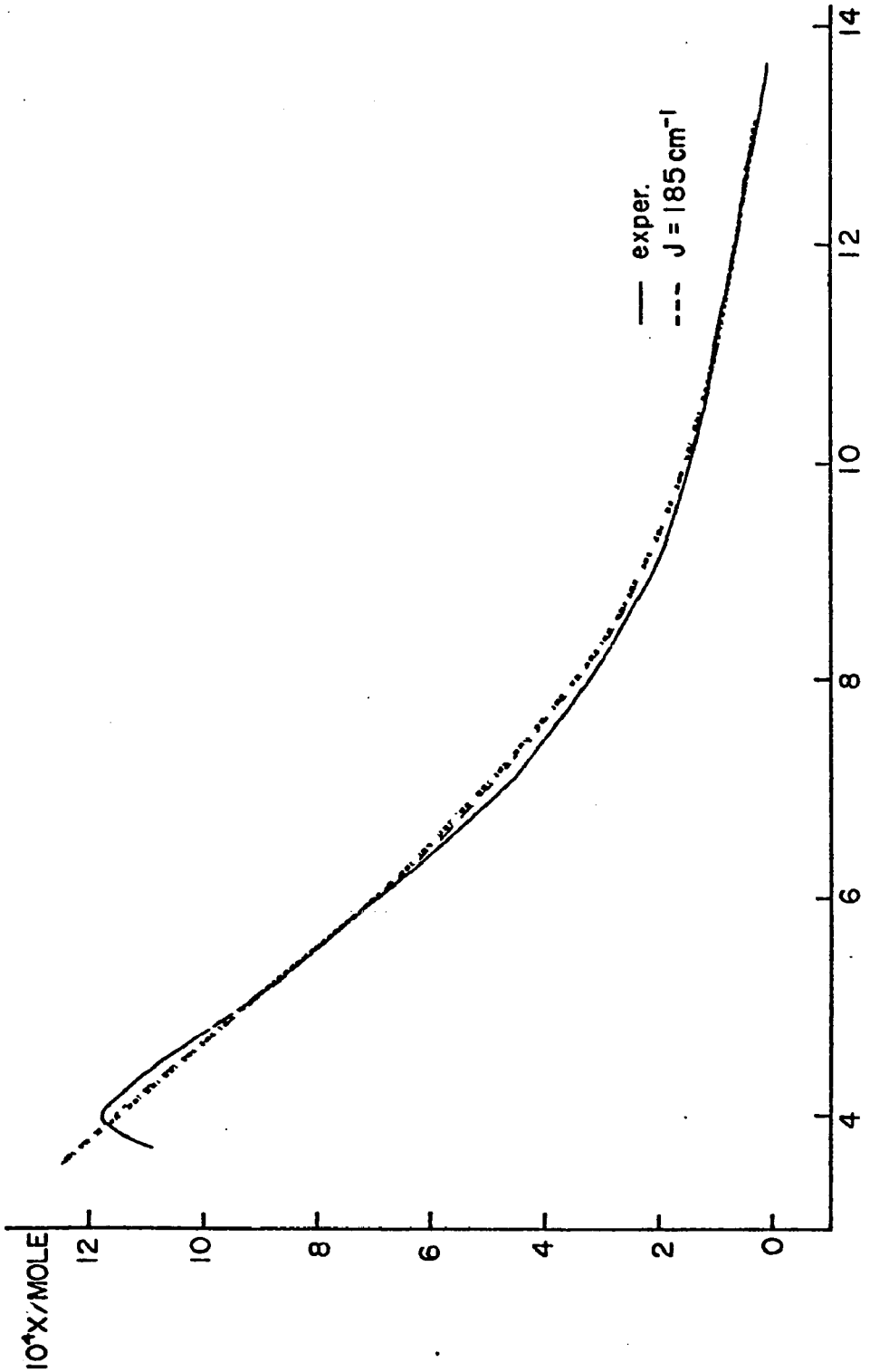


Figure 9. Magnetic Susceptibility of Oxidized Algal Ferredoxin

temperature the exchange energy becomes small with respect to kT. Since there are two iron atoms in the ferredoxin, this data suggests that the two spins are antiferromagnetically coupled. Using the Curie susceptibility equation and summing over the possible states, each being weighted by the Boltzmann probability, the data can be fit with $S_1 = S_2 = 5/2$, 2, 3/2, or 1. Figure 9 (dotted curve) shows only the fit for $S_1 = S_2 = 5/2$ with $J = -185\ cm^{-1}$ since this is the only choice consistent with other data. Susceptibility alone cannot select the spin states of the individual iron atoms.

Figure 10 shows that at low temperatures, $T = 77^{o}K$, the reduced protein behaves like a single electron, $S = 1/2$, with simple Curie inverse temperature behavior. However, at higher temperatures, the sample shows more paramagnetism than expected for the simple $S = 1/2$ case, again indicating a spin exchange interaction. Since the Mossbauer results will show that a $d_{x^2-y^2}$ excited state may lie $430\ cm^{-1}$ above a ferrous iron d_{z^2} ground state orbital, the magnetic susceptibility was calculated with and without the excited state contribution. The dashed curve in Figure 10 shows the theoretical susceptibility for $S_1 = 5/2$, $S_2 = 2$ with $J = 115\ cm^{-1}$; this calculation assumed that the orbital with the paired electron is d_{z^2}. The dotted curve is the theoretical susceptibility for the same spin states but with $J = 98\ cm^{-1}$ for the d_{z^2} orbital and an excited ferrous $d_{x^2-y^2}$ at $430\ cm^{-1}$ above the d_{z^2} ground state with $J_{exc} = 175\ cm^{-1}$. It has also been shown that the addition of

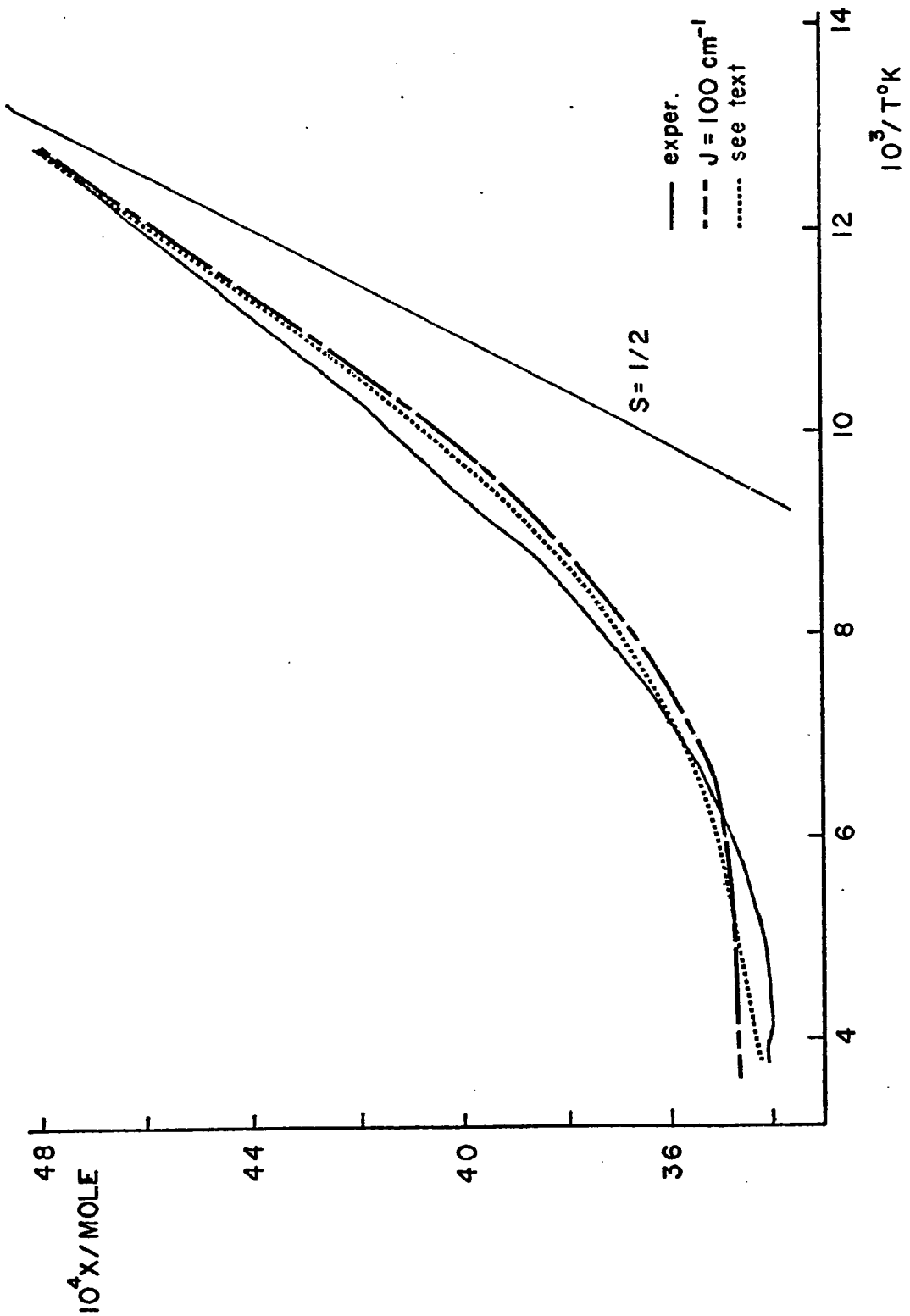


Figure 10. Magnetic Susceptibility of Reduced Algal Ferredoxin

3% ferric due to reoxidized protein will lower the calculated J to 80 cm^{-1} (7).

Although the magnetic susceptibility cannot alone determine the spin states for either the oxidized or reduced ferredoxin, it does establish that in both states the iron atoms are antiferromagnetically exchanged coupled. This interaction results at low temperatures in diamagnetism for the oxidized protein and a net spin of one-half for the reduced protein. Thus both iron atoms have the same spin in the oxidized proteins, and their spins differ by one-half in the reduced protein.

B. EPR Results

EPR was attempted on both oxidized and reduced algal ferredoxin. No EPR signal was observed in the oxidized protein which is consistent with the magnetic susceptibility data that the protein is diamagnetic at low temperatures. At higher temperatures the oxidized protein does become paramagnetic, but the signal has yet to be observed.

Reduced algal ferredoxin has the EPR spectrum shown in Figure 11. A computer simulation (36) is also shown in Figure 11 using a single unpaired electron, as is justified by the fact that at low temperatures the magnetic susceptibility is simple Curie S = 1/2. EPR electronic g-values and anisotropic linewidths are the computer program input parameters, and the best fit occurs for $g_{x,y,z}$ = 1.88, 1.96, 2.05 and $L_{x,y,z}$ = 22.0, 13.0, 9.5 gauss (HWHM). The origin

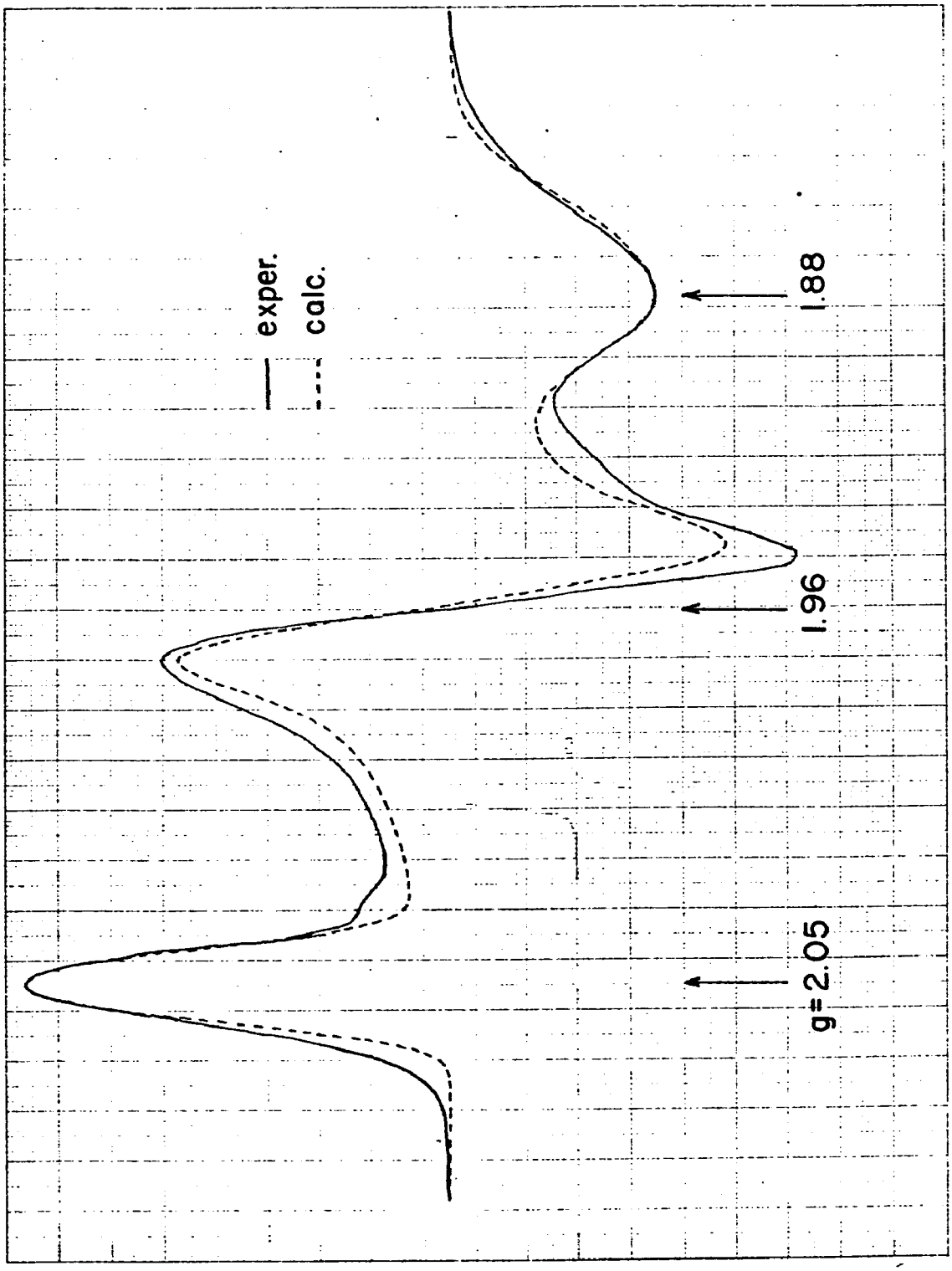


Figure 11. EPR of Reduced Native Algal Ferredoxin with Computer Simulation

of the low g-values will be discussed later, but the large EPR linewidths are not readily explained since the intrinsic linewidth ($1/\gamma T_2$) has been determined to be less than a gauss by both EPR saturation experiments and from the ENDOR linewidths. If this width were due to hyperfine interactions (e.g, protons and nitrogen), the linewidth would be magnetic field independent, but since the electronic Zeeman interaction is linear with applied field, the field separation between principal g-values will increase with field. EPR data at X- and K-band was compared and revealed that for the four-fold increase in magnetic field, the EPR linewidths increased by the same (within experimental error) four-fold factor; the Zeeman interaction behaved as expected. Another experiment which shows that the linewidths are not due to hyperfine interactions compares fully protonated to fully deuterated proteins. The resulting EPR spectra are identical except for a 10% decrease in linewidth for the deuterated protein. Since the deuterium moment ($I = 1$) is one-tenth that of the proton ($I = 1/2$), the hyperfine interactions with deuterium in this case would have a negligible effect on the linewidth. One can conclude that although there are proton hyperfine interactions with the unpaired spin, these interactions are too small to account for the EPR linewidths.

All of the above experiments require that the EPR linewidth originates from a term linear with applied field and not from hyperfine interactions. This effect can be represented - but not explained -

by a "g-strain" term where the principal g-values are no longer unique but take on a distribution of values for various molecules. This however, neither answers the question of the origin of such an effect, nor can one determine if there is a distribution of slightly different proteins, or a distribution in the conformation of the same protein.

Figure 12 shows the EPR for two fully deuterated algal ferredoxin samples, one reconstituted with ^{56}Fe (I = 0) and the other reconstituted with ^{57}Fe (I = 1/2). A comparison of the native (Figure 11) and ^{56}Fe reconstituted (Figure 12) shows that they are identical. The fact that the linewidth at g_z increases by approximately 20% implies that the iron has a hyperfine interaction with the unpaired electron and hence is near the active site. A computer simulation can account for this broadening using either one or two iron atoms, but EPR cannot distinguish between the two cases. The z-component of the hyperfine interaction can be estimated to be 14 gauss. Since the magnetic susceptibility, ENDOR, and Mossbauer all demand the two nonequivalent iron case, the parameters from these other data are used for the computer fit in Figure 13. Both the native and ^{57}Fe reconstituted ferredoxin EPR computer simulations show the assumed lineshape is not correct. A Gaussian shape was used but neither it nor a Lorentzian shape is adequate. Since the origins of the large EPR linewidth are not understood, however, these discrepancies are not surprising.

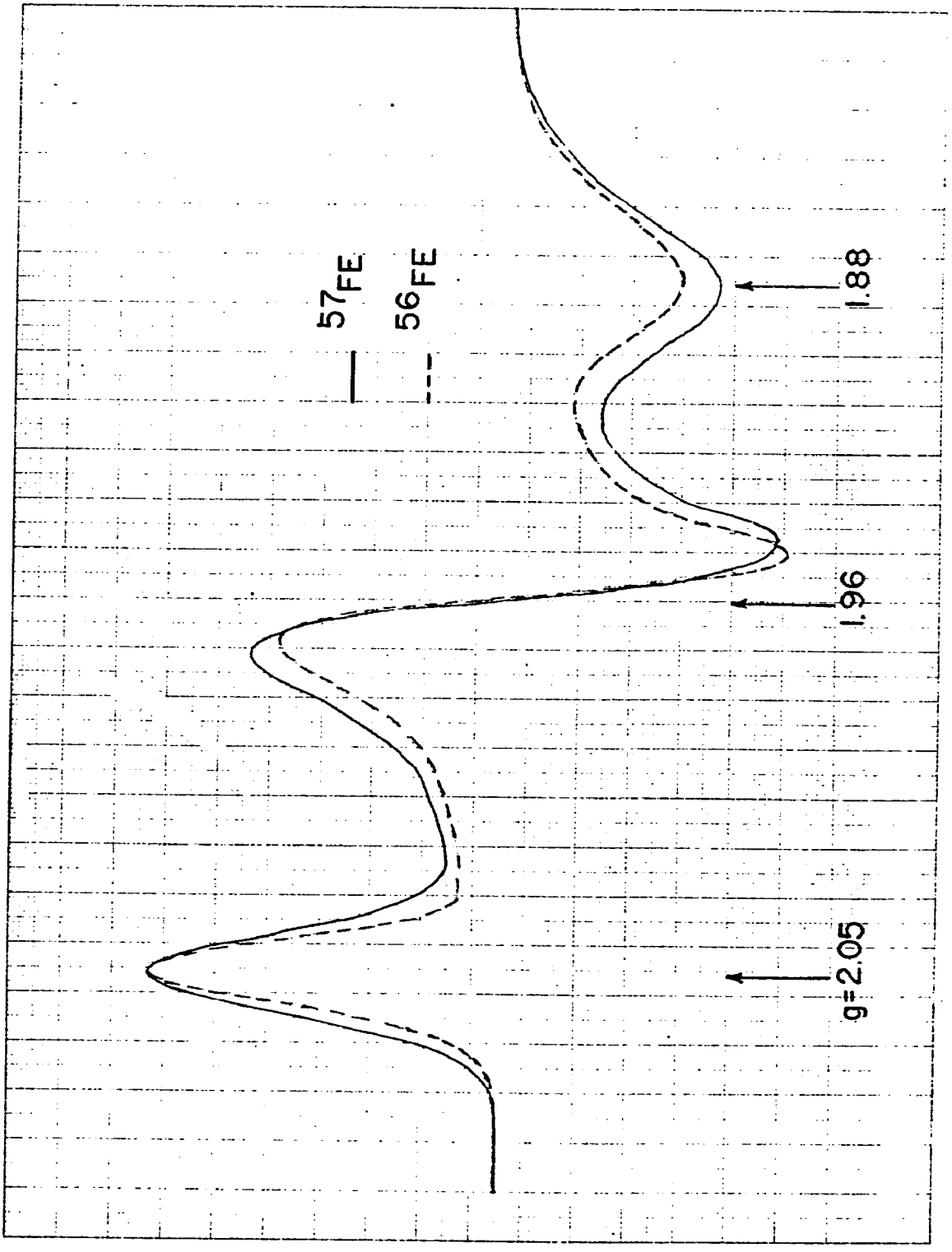


Figure 12. EPR of Reduced Reconstituted ^{56}Fe and ^{57}Fe Algal Ferredoxin

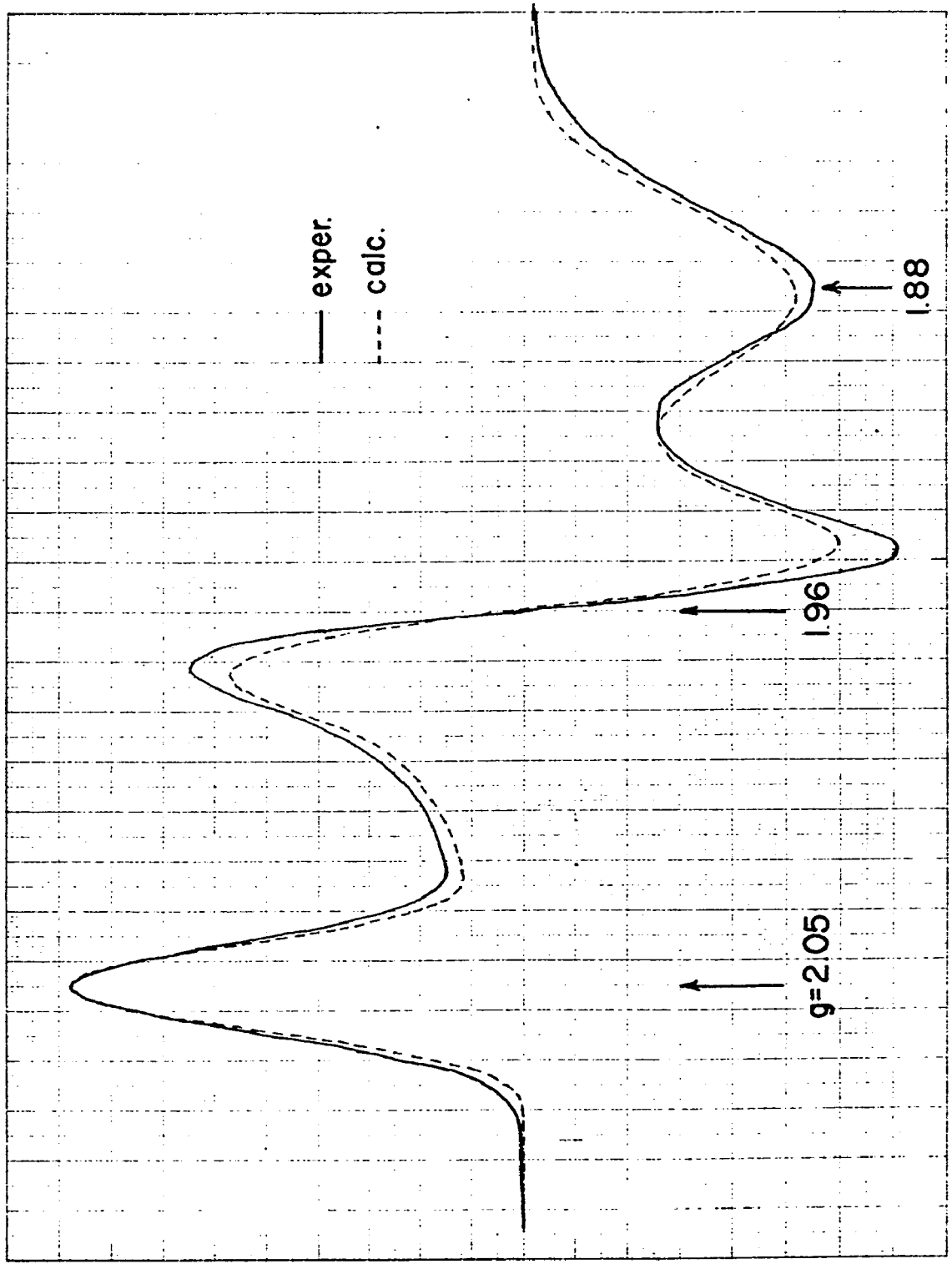


Figure 13. EPR of Reduced ^{57}Fe Reconstituted Algal Ferredoxin with Computer Simulation

C. ENDOR Results

The following data is a measurement of the hyperfine tensors for the two iron atoms in algal ferredoxin. As discussed previously, the iron ENDOR lines will be centered at $A_{eff}/2$ and if only a single orientation is being observed, a doublet will appear which is split by twice the iron Zeeman frequency, or 1 MHz. In practice a resolved doublet is virtually never seen since many orientations in the amorphous sample are observed. The ferric iron ENDOR signals will appear in the 20-30 MHz region, protons centered at the proton Zeeman frequency will appear in the 8-20 MHz region, nitrogen will be observed as a long sloping baseline from 1 MHz to 15 MHz, and the ferrous iron will appear in the region 5-18 MHz along with nitrogen and proton ENDOR signals.

1. Ferric ENDOR

The most readily observed and interpreted ferredoxin ENDOR signals are the ferric iron resonances. The native protein exhibits no ENDOR resonances in the region 20-30 MHz, but the protein reconstituted with ^{57}Fe does. Figure 14 is an ENDOR spectrum taken while saturating the g_z region of the EPR line. The absorption appears as a broad symmetric distribution from 20 to 24 MHz centered at 22 MHz. If the A- and g-tensor principal axis were coincident, this field setting would result in the most resolved A_z doublet and hence the most accurate determination of A_z would be 44 MHz. However, Figure 15 shows that at H_z + 30 gauss, a resolved doublet appears centered at

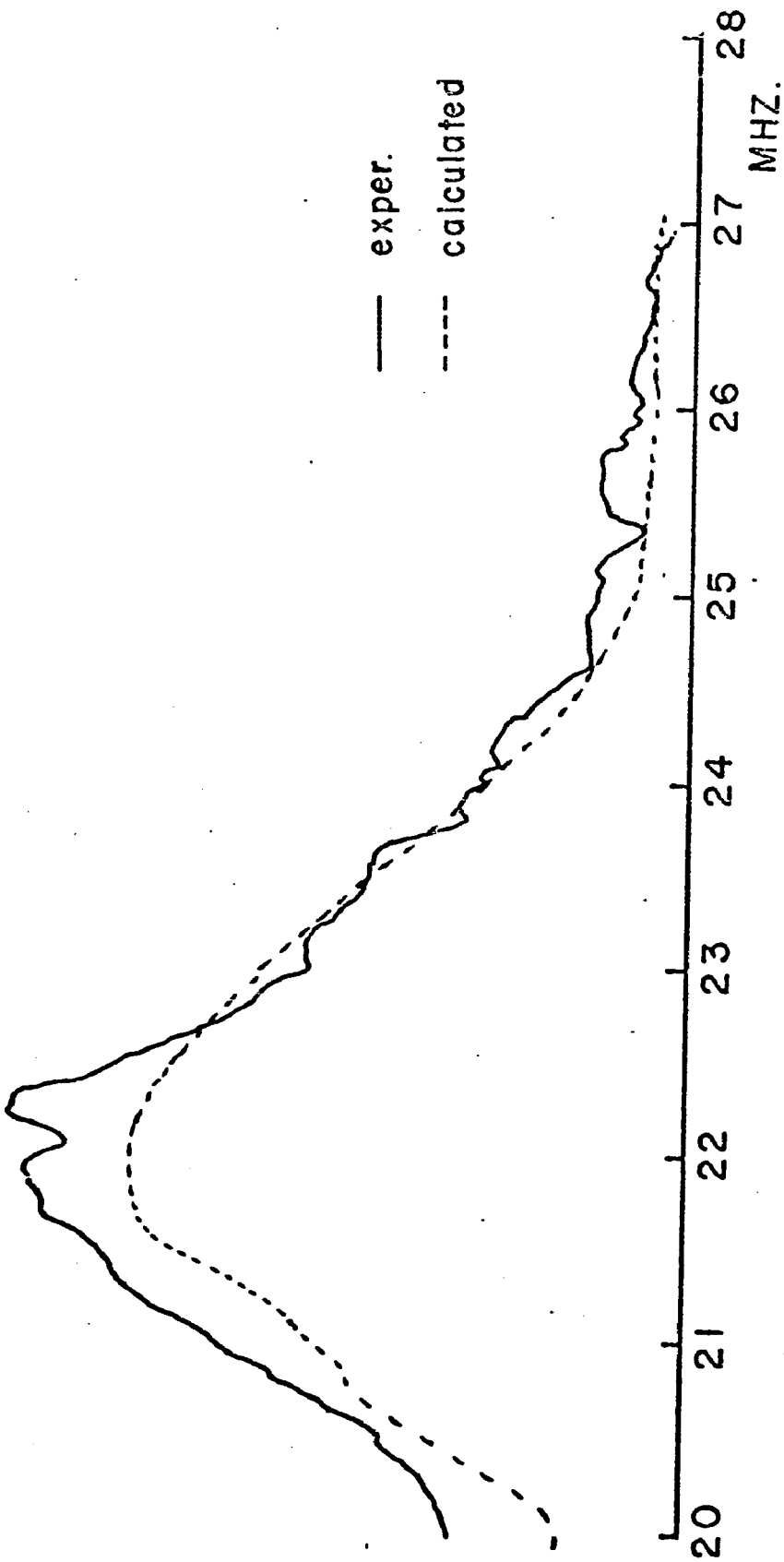


Figure 14. Experimental and Calculated ^{57}Fe (Ferric) ENDOR Spectrum at H_z

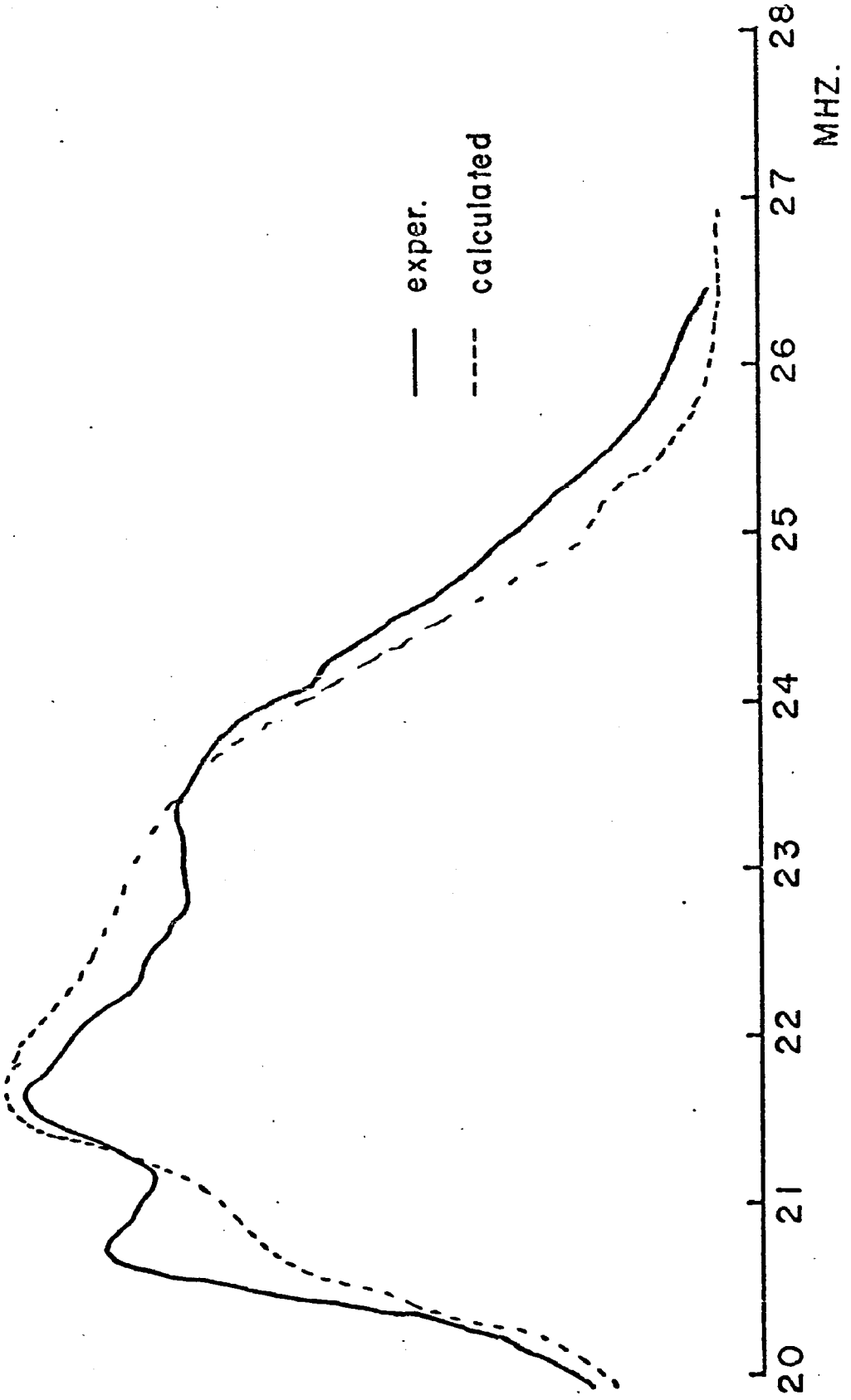


Figure 15. Experimental and Calculated ^{57}Fe (Ferric) ENDOR Spectrum at H_z + 30 Gauss

21.2 MHz and split by 1 MHz, twice the iron Zeeman frequency. A broad distribution to higher frequency (centered at 23 MHz) also overlaps part of the doublet and extends the ENDOR resonance to 26 MHz. The fact that a resolved doublet appears at a field not corresponding to a principal g-value indicates that the A- and g-tensors are not coincident. For the $H = H_z$ case, molecules whose A-tensor z-axis lies aong the applied field are not saturated, but they are at H_z + 30 gauss. Hence the A-tensor is oriented relative to the g-tensor by a rotation about the g_x axis. The amount of rotation can be calculated from the equation for g_{eff} (see p. 30) and the angle is approximately 25-35°, if one assumes the principal A_z value occurs for H_z + 30 gauss. This assumption is justified by the fact that although the doublet resolution is equally good at H_z + 60 gauss (Figure 16), it is now centered at a higher frequency, 21.4 MHz; the broad distribution at this field has moved up frequency faster than the doublet and is centered at 24.3 MHz. At H_z + 120 gauss (or H_y - 20 gauss) - Figure 17 - two broad distributions occur since now many orientations are being sampled. A similar situation exists in Figure 18 for H_z + 195 gauss (or H_y + 50 gauss, or H_x - 80 gauss) but now the two distributions have merged and are centered at 24.3 MHz; there is also a hint of a doublet centered at 25 MHz and split by 1 MHz. The data at H_y - 20 gauss and H_y + 50 gauss (the maximum field modulation is too small to reach H_y exactly, but little would be gained) suggests that $A_y/2$ is approximately

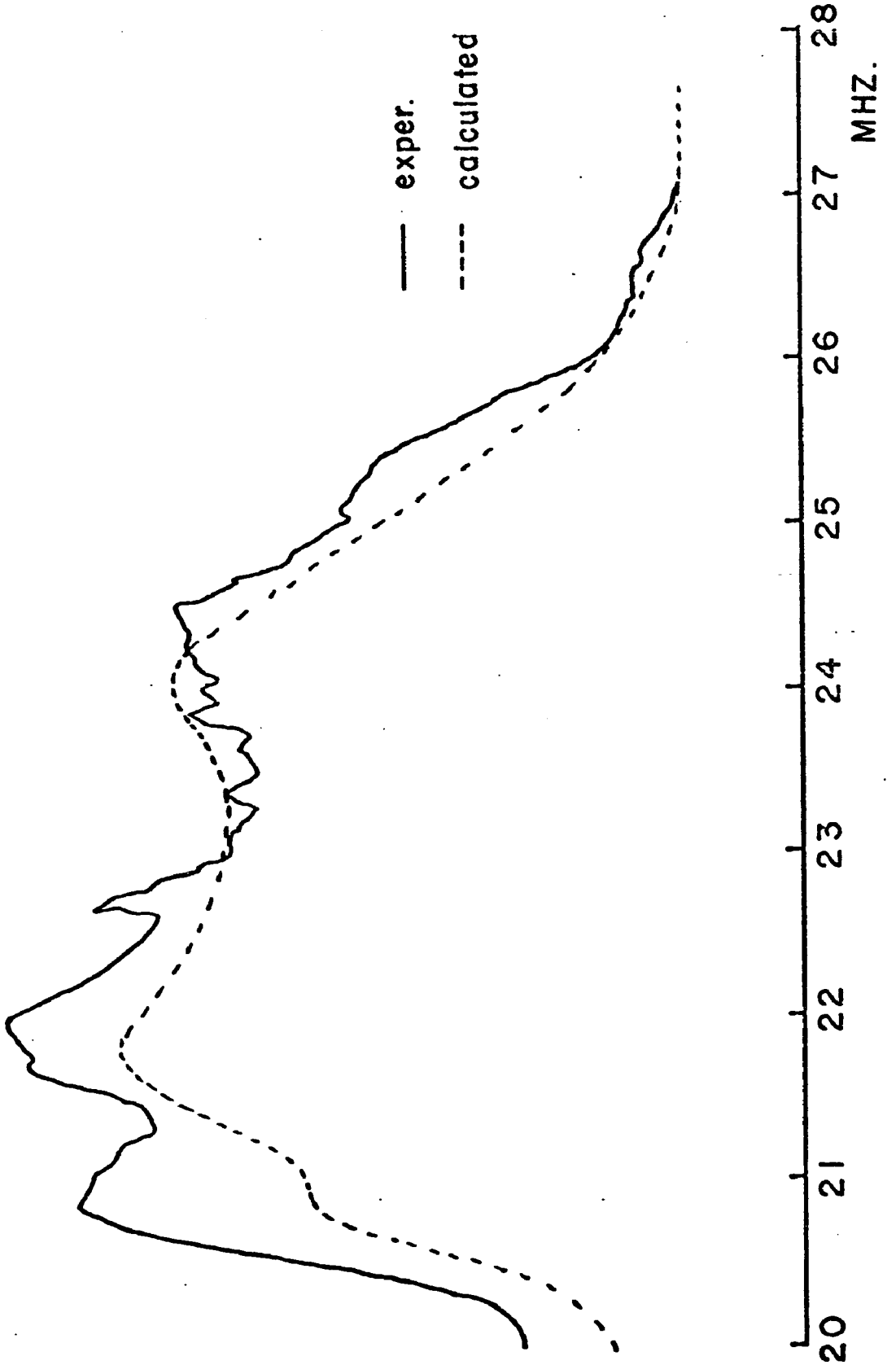


Figure 16. Experimental and Calculated ^{57}Fe (Ferric) ENDOR Spectrum at H_z + 60 Gauss

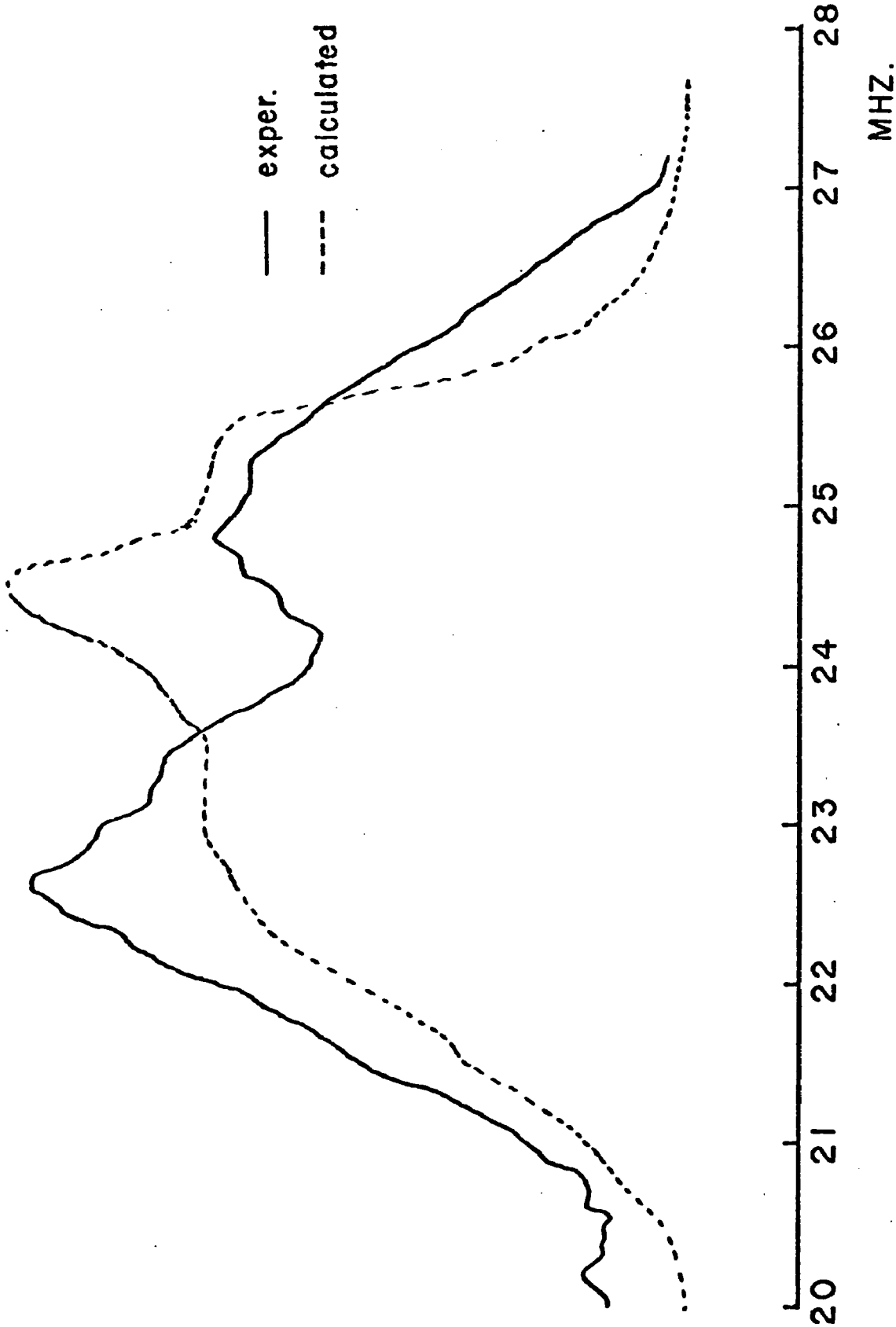


Figure 17. Experimental and Calculated ^{57}Fe (Ferric) ENDOR Spectrum at H_z + 120 Gauss

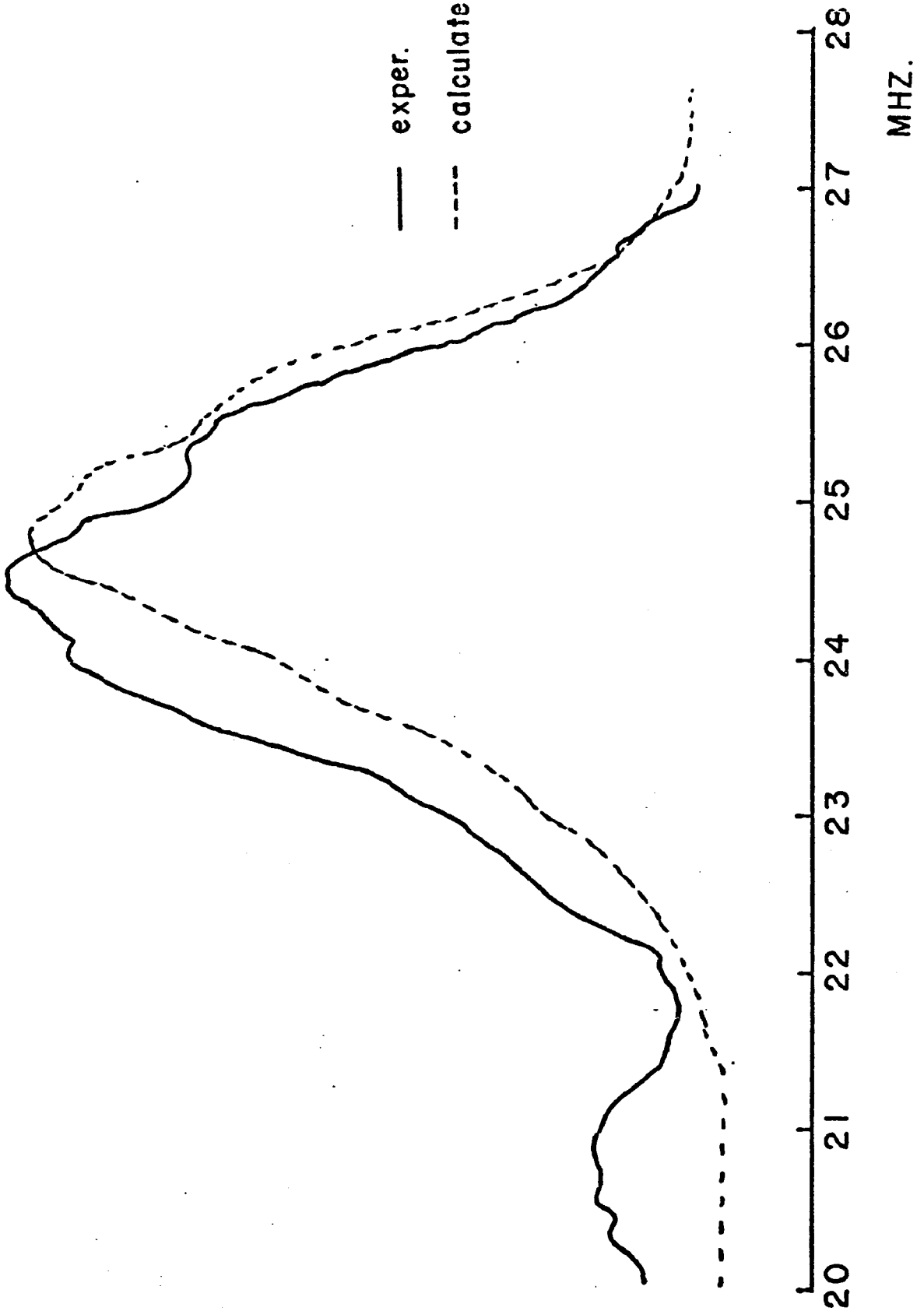


Figure 18. Experimental and Calculated ^{57}Fe (Ferric) ENDOR Spectrum at H_x - 80 Gauss

24.5 MHz $\pm$ 1 MHz, but since so many orientations are being sampled a computer fit is required; this will be discussed below. The third principal A-value, A_x, is obtained with the field set at H_x. Figure 19 shows this resonance which is a skewed, poorly resolved doublet. By setting the field 60 gauss above H_x there is very little EPR intensity but a "purer" selection of g_x molecules is obtained. Figure 20 shows this data and now a nicely resolved doublet appears centered at 25.6 MHz and split by 1 MHz. A_x is taken as 51.2 MHz. A_y must be determined by computer fits using the experimental values for A_x and A_z and the 30° rotation about the g_x axis.

The computer simulation (see Appendix) uses as input parameters the EPR anisotropic g-values, EPR linewidths, ENDOR linewidth (assumed isotropic), and the principal hyperfine values. The program calculates an EPR stick spectrum and then for each chosen applied field, the rf frequency space is sampled and contributions to the ENDOR spectrum are summed. The computer simulations accompany the experimental data (Figures 14-20) and show that the agreement is quite good except at g_y, where, because many orientations are sampled, a computer fit is necessary to determine A_y. The curious feature of the data which the simulations does not demonstrate is the persistency (from H_z to H_y - 20 gauss) of the A_z contribution centered at 22 MHz (see Figures 14-17). The ENDOR resonance moves 1 MHz from H_z to H_z + 120 gauss and then at H_y it suddenly moves and merges with the distribution at 25 HMz. This

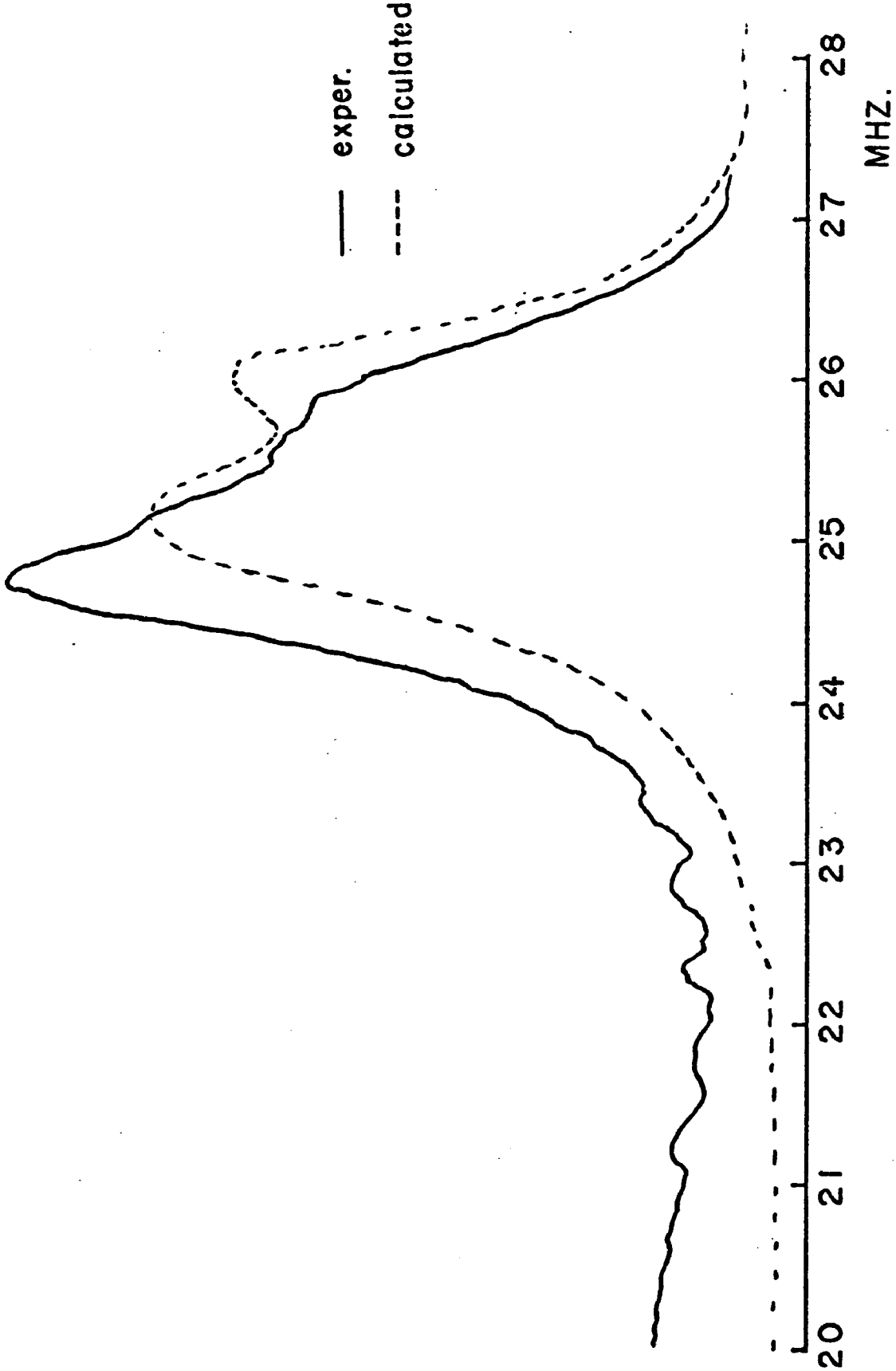


Figure 19. Experimental and Calculated ^{57}Fe (Ferric) ENDOR Spectrum at H_x

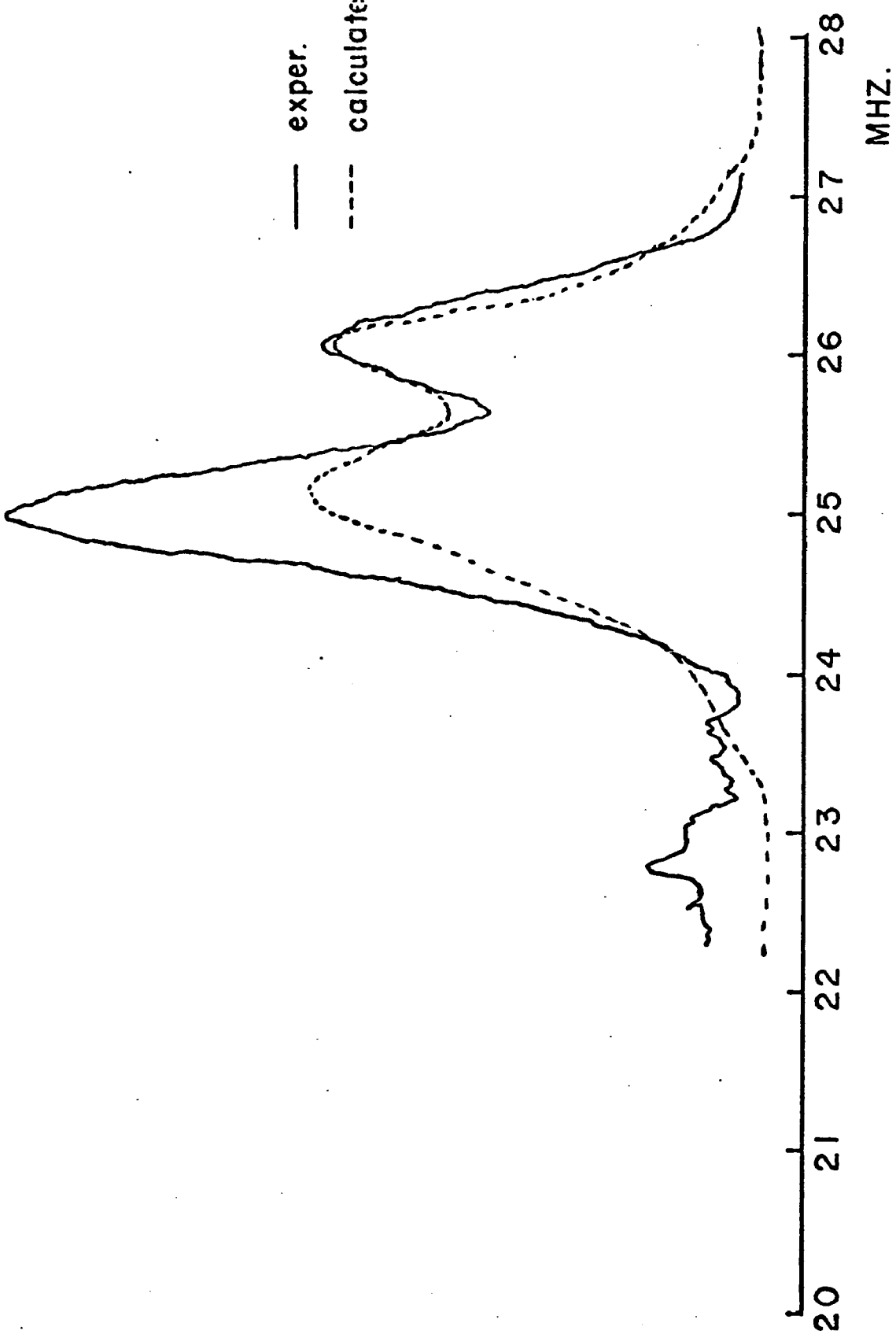


Figure 20. Experimental and Calculated ^{57}Fe (Ferric) ENDOR Spectrum at H_x + 60 Gauss

remains unexplained and hence A_y cannot be determined with great accuracy.

2. Ferrous ENDOR

The ENDOR determination of the ferrous iron hyperfine values was complicated by the presence of many proton and nitrogen ENDOR signals. Nitrogen will be shown to result in the broad distribution whose maximum amplitude is below the minimum operating frequency of the spectrometer and which approaches zero at 20 MHz. In protonated samples, the nitrogen tail above 10 MHz is obscured by numerous proton ENDOR signals which are centered at the free proton frequency (14 MHz) and split by their hyperfine interactions; the largest observed proton splitting occurs at 18.5 MHz. These difficulties with proton signals prevented the observation of A_x and A_y for the ferrous iron in spinach ferredoxin (5) and protonated algal ferredoxin. The following data are all obtained from fully deuterated algal ferredoxin.

The nitrogen signals are sufficiently large to require one to take ^{56}Fe versus ^{57}Fe difference spectra as discussed in the instrumentation section. The ferric ENDOR data showed that there is zero difference ENDOR signal at 19-20 MHz for H_z, and 19-24 MHz at H_x; these results allow one to set the relative gains to equalize the ENDOR intensity at 19.5 MHz. Any resulting differences in other regions below 19 MHz must result from the presence of the iron nuclear spin.

Figure 21 shows the ENDOR spectrum from 10-20 MHz with the field set to H_z on the ferredoxin EPR line. The difference spectrum is plotted in Figure 22 and shows a distribution with full width at half maximum of 2.5 MHz and centered at 17.5 MHz. This distribution is due principally to A_z, although the skewing to the low frequency side is due to contributions from molecules whose g_z-axis is not quite oriented parallel to H_o. The contributions from these other molecules would be greatly decreased by operating below H_z, but the intensity is too small to get reliable data. The fact that one observed no doublet split by twice the iron nuclear Zeeman frequency can result from (1) ENDOR linewidths too great to observe resolution, (2) signal-to-noise not sufficiently high to observe any resolution, or (3) the A_z principal axis is not coincident with the g_z axis. Although this last possibility cannot be excluded, the signal-to-noise is insufficient to make such a conclusion. Hence it is tentatively concluded that the observed A-value is a principal value, giving A_z = 35 MHz $\pm$ 0.5 MHz.

As one moves up field from H_z, the distribution skews more toward low frequency. Whereas the zero difference signal began at 16 MHz at H_z, it has moved to 15.5 MHz at H_z + 30 gauss, and to 12.5 MHz at H_z + 60 gauss (Figure 23). The maximum of the distribution moves more slowly, having reached 16.5 MHz at H_z + 60 gauss relative to 17.5 MHz at H_z. This broadening occurs because many orientations, hence many A_{eff} values, are sampled when the field is

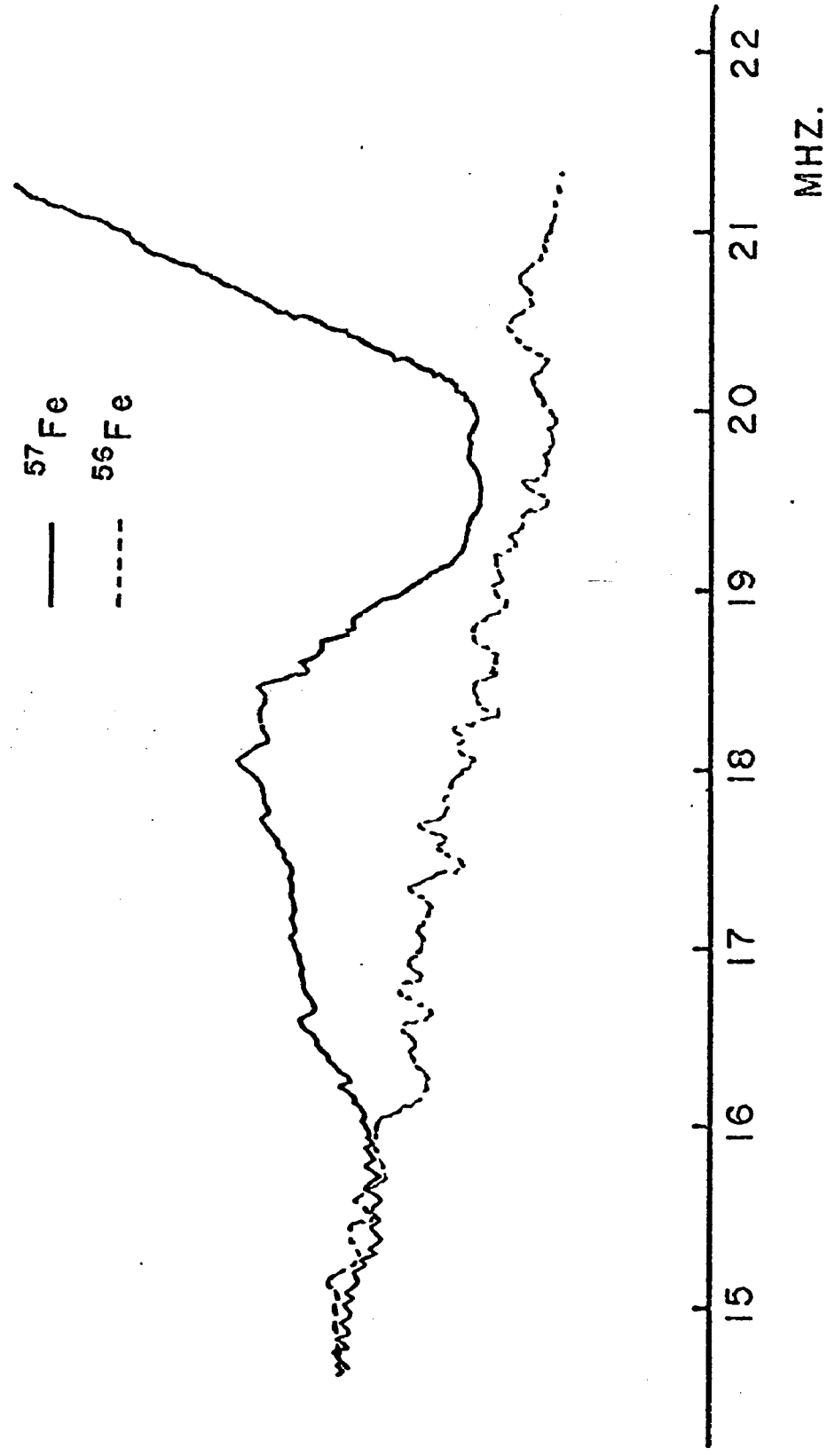


Figure 21. Experimental ^{56}Fe and ^{57}Fe (Ferrous) ENDOR Spectra at H_z

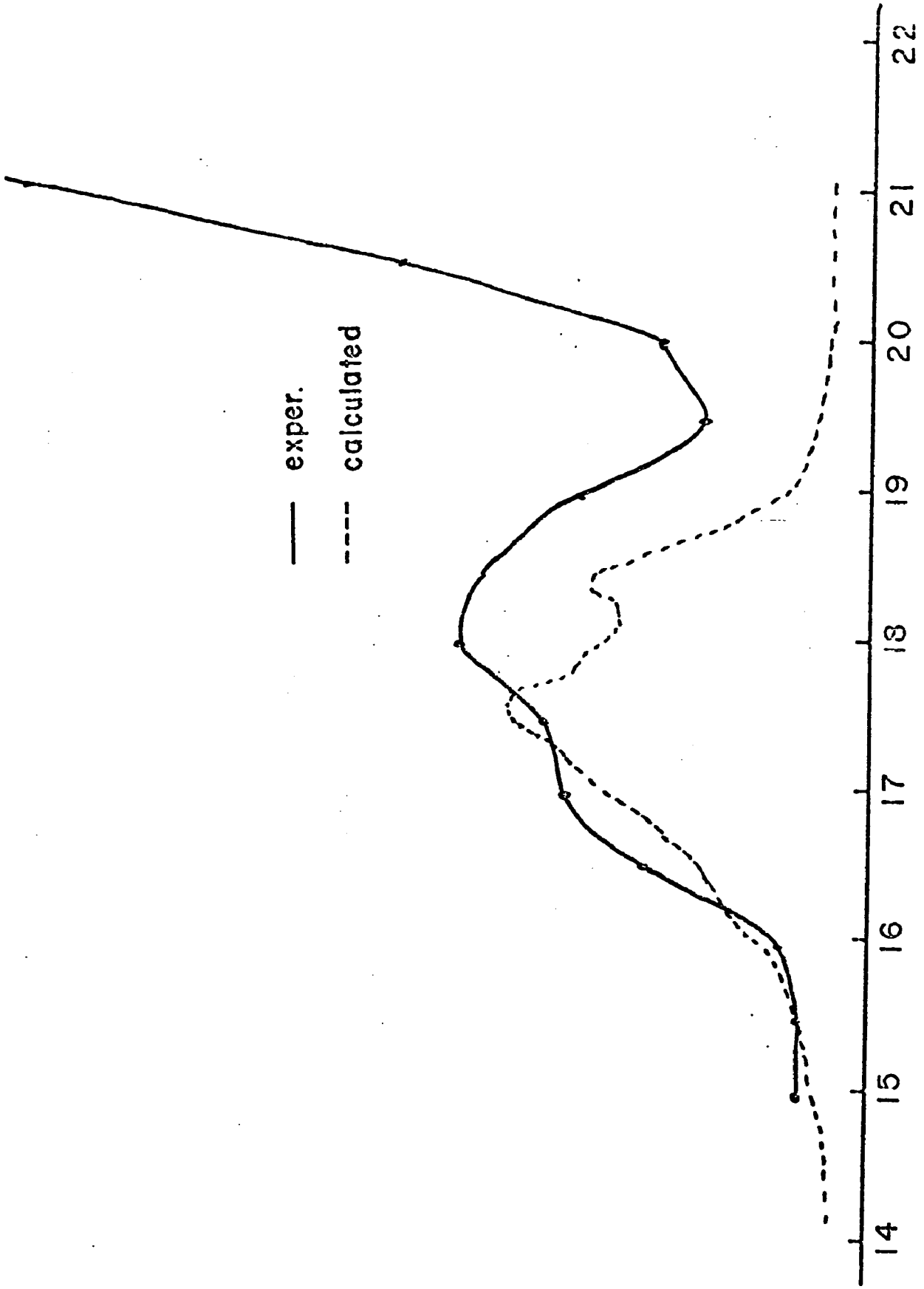


Figure 22. Experimental Difference and Calculated ENDOR Spectra at H_z

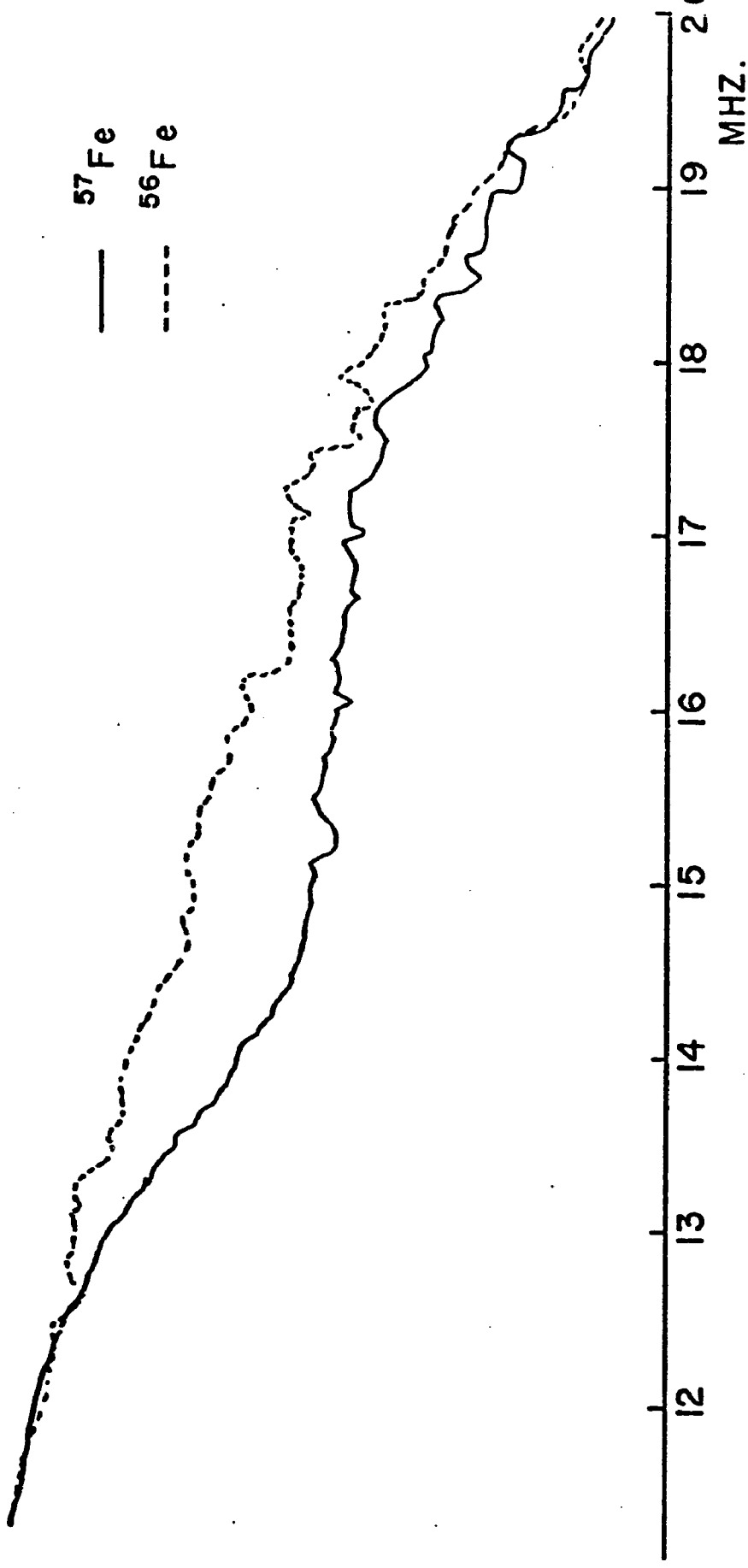


Figure 23. Experimental ^{56}Fe and ^{57}Fe (Ferrous) ENDOR Spectra at H_z + 60 Gauss

not set to H_z, but yet the nearest principal A value still dominates. At H_z + 90 gauss the difference intensity is very small (10% of background) due to the great width (4 MHz) of the distribution; at this field the difference (Figure 24) is nonzero from 9.5 to 17.5 MHz.

Additional technical problems arise at H_y since the instrument rf sweep range cannot span the A_y distribution. The high frequency portion of the distribution (Figure 25) is obtained as usual by sweeping from 7.6 MHz to 20 MHz, setting the gains for zero difference signal at 19 MHz; this is justified by the movement of the distribution from A_z as noted above. With these gain adjustments, it was found that the zero difference extended from 15.5 MHz to 19 MHz (Figure 26); above 19 MHz the ferric iron contributes to the difference. Below 14 MHz the distribution is essentially flat to the bottom of the range at 7.6 MHz; the largest signal difference in this region is approximately 15% of the background signal. For the low frequency portion of the distribution (Figures 27 and 28) the amplifier range used was 4.8 MHz to 13 MHz while the final tank tuning range was 4.8 MHz to 19.5 MHz. By using the second harmonic of the amplifier frequency, that is, tuning the final tank circuit to 19 MHz while the amplifier and rf oscillator are tuned to 9.5 MHz, the gains were adjusted for zero difference, and then the fundamental range, 4.8-13 MHz, was swept. The result showed that the difference signal was nearly zero at 4.8 MHz. A spectrum swept from 3-7 MHz, with the relative gains set at 3 MHz, showed

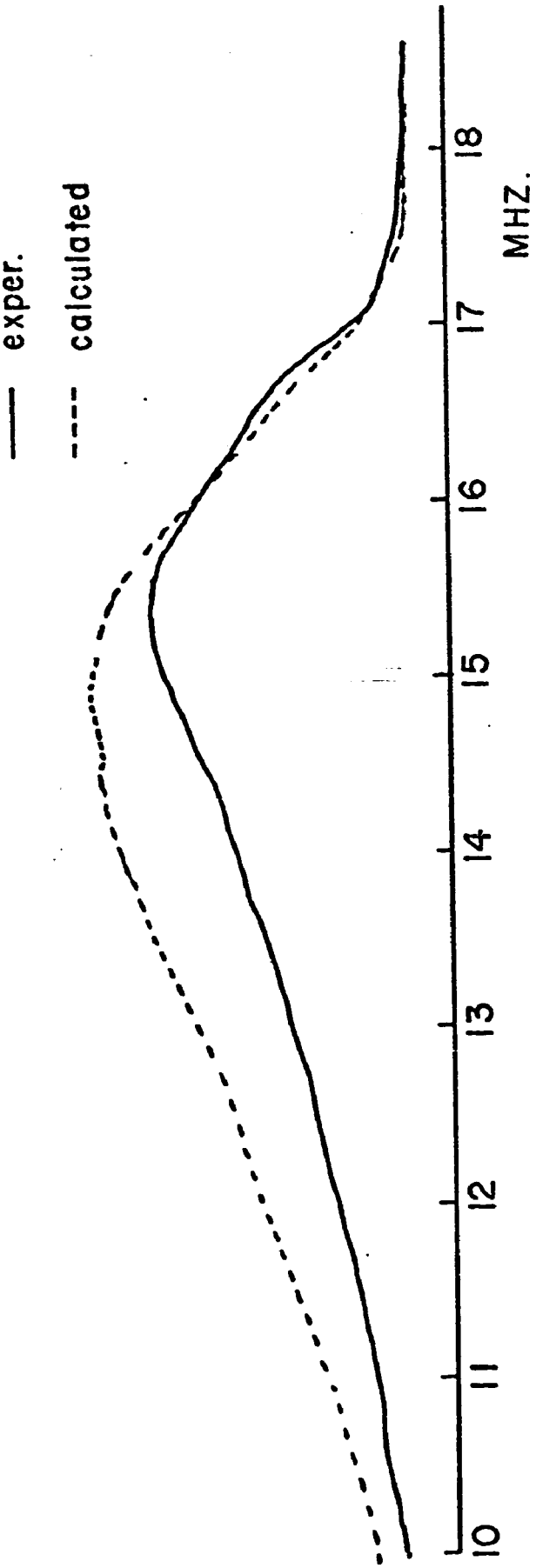


Figure 24. Experimental Difference and Calculated ENDOR Spectra at H_z + 90 Gauss

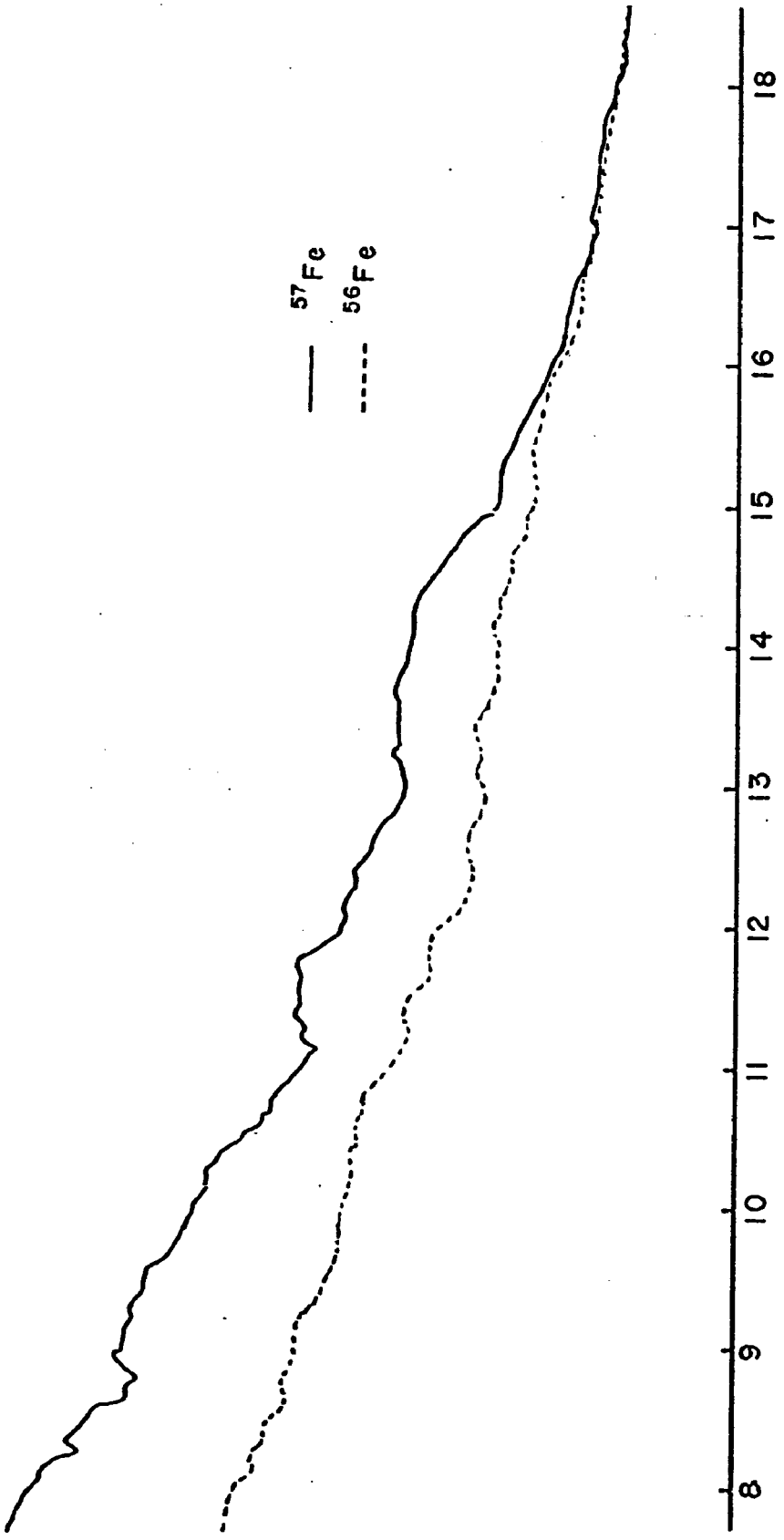


Figure 25. Experimental ^{56}Fe and ^{57}Fe (Ferrous) ENDOR Spectra at H_y

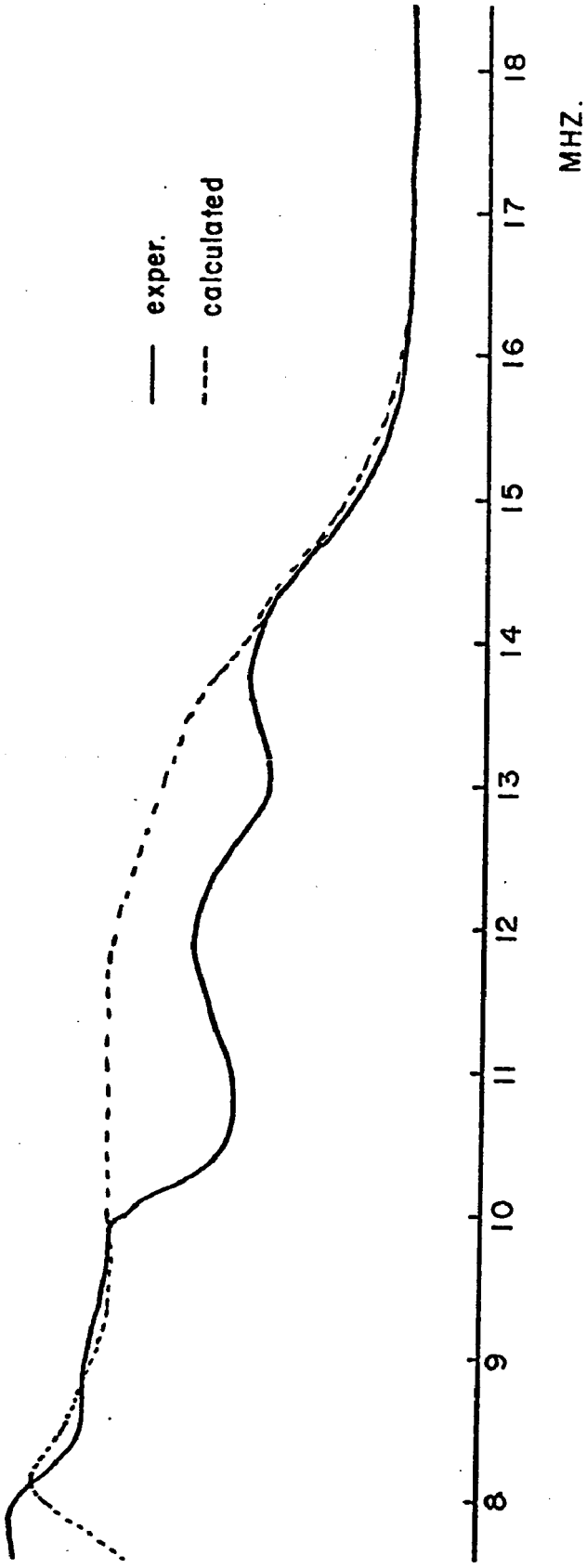


Figure 26. Experimental Difference and Calculated ENDOR Spectra at H_y

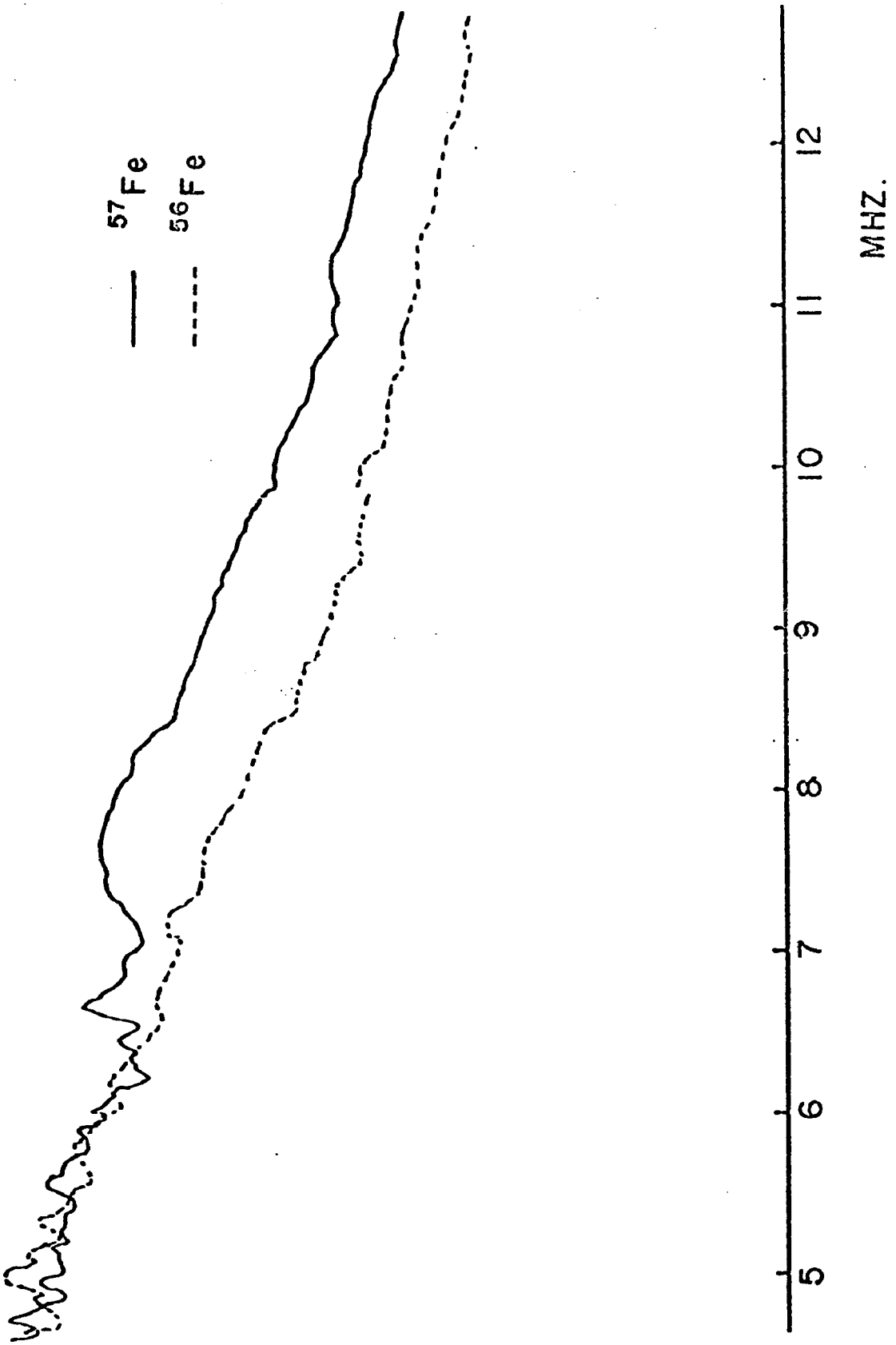


Figure 27. Experimental ^{56}Fe and ^{57}Fe (Ferrous) ENDOR Spectra at H_y

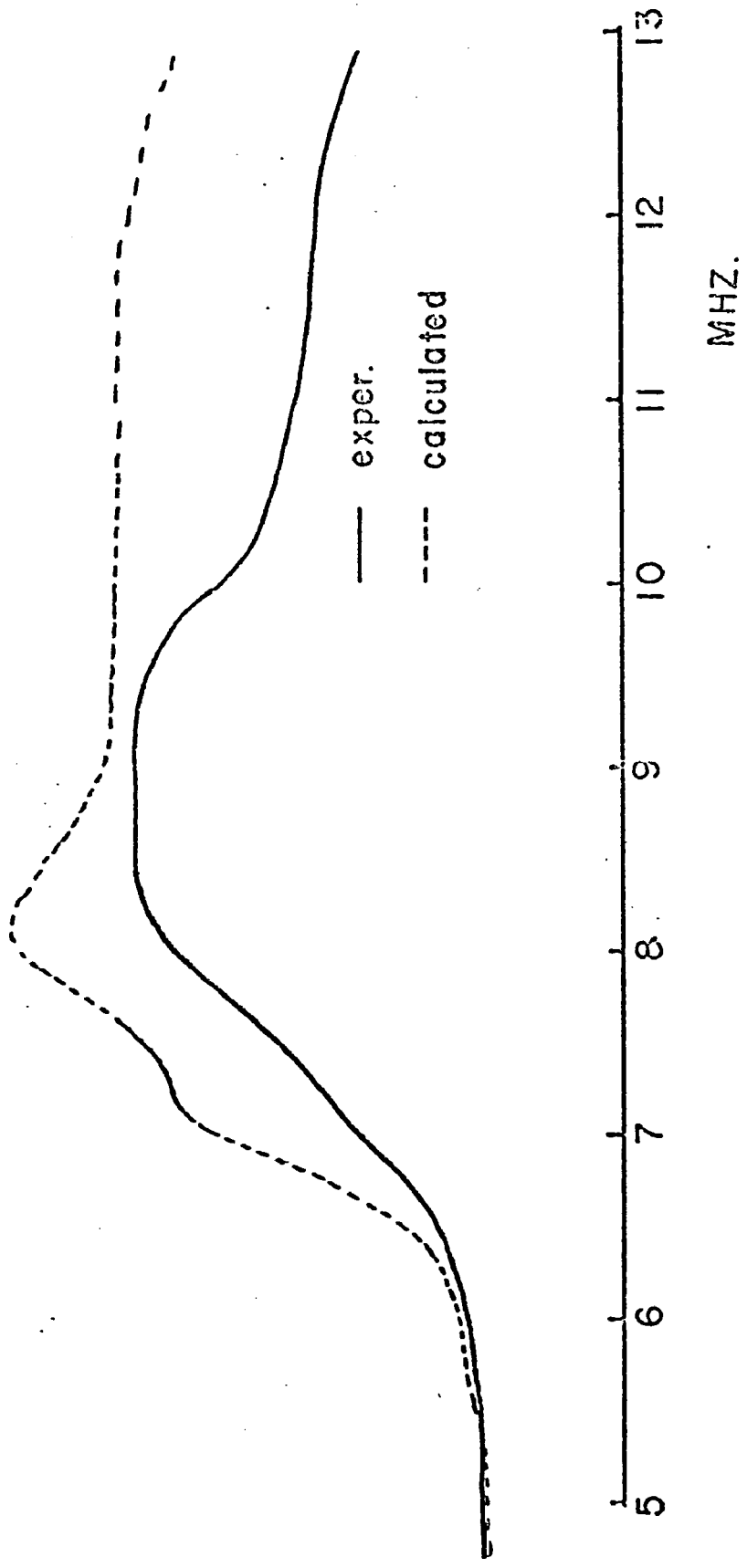


Figure 28. Experimental Difference and Calculated ENDOR Spectra at H_y

that the difference signal actually began at 4.5 MHz. The assumption of zero difference at 3 MHz for H_y experiments was justified by the fact that no difference signals were observed in that range for fields from H_z to H_z + 60 gauss. Since many orientation angles satisfy the H_y resonant condition in Equation 5, the observed difference signal does not allow an A_y assignment without computer fit; this will be discussed below. Similar gain setting procedures were required at fields above H_y. It was observed that the low frequency tail moved down very slowly, if at all, as H_x was approached, while the high frequency end came down quickly from 15.5 MHz at H_y (H_x - 125 gauss) to 12 MHz at H_x - 60 gauss, to 10 MHz at H_x. At H_x + 10 gauss (Figures 29 and 30) the difference signal is similar to that observed at H_z and shows a 2.5 gauss wide distribution peaked and centered at 6.7 gauss. Again no doublet was consistently observed, but since no lower frequency difference is observed, A_x is assumed to be 13.5 MHz.

The computer simulation was begun using A_x = 13.5 MHz and A_z = 35 MHz. A_y and the ENDOR linewidths are relatively free parameters but the latter can't be more than about a megahertz. As expected the spectra most sensitive to A_y variations are those recorded within the range $H_y \pm 40$ gauss. Since it is difficult to trust shape comparisons when two or more rf sweep ranges are used, the zero difference frequencies were used as the major computer fit

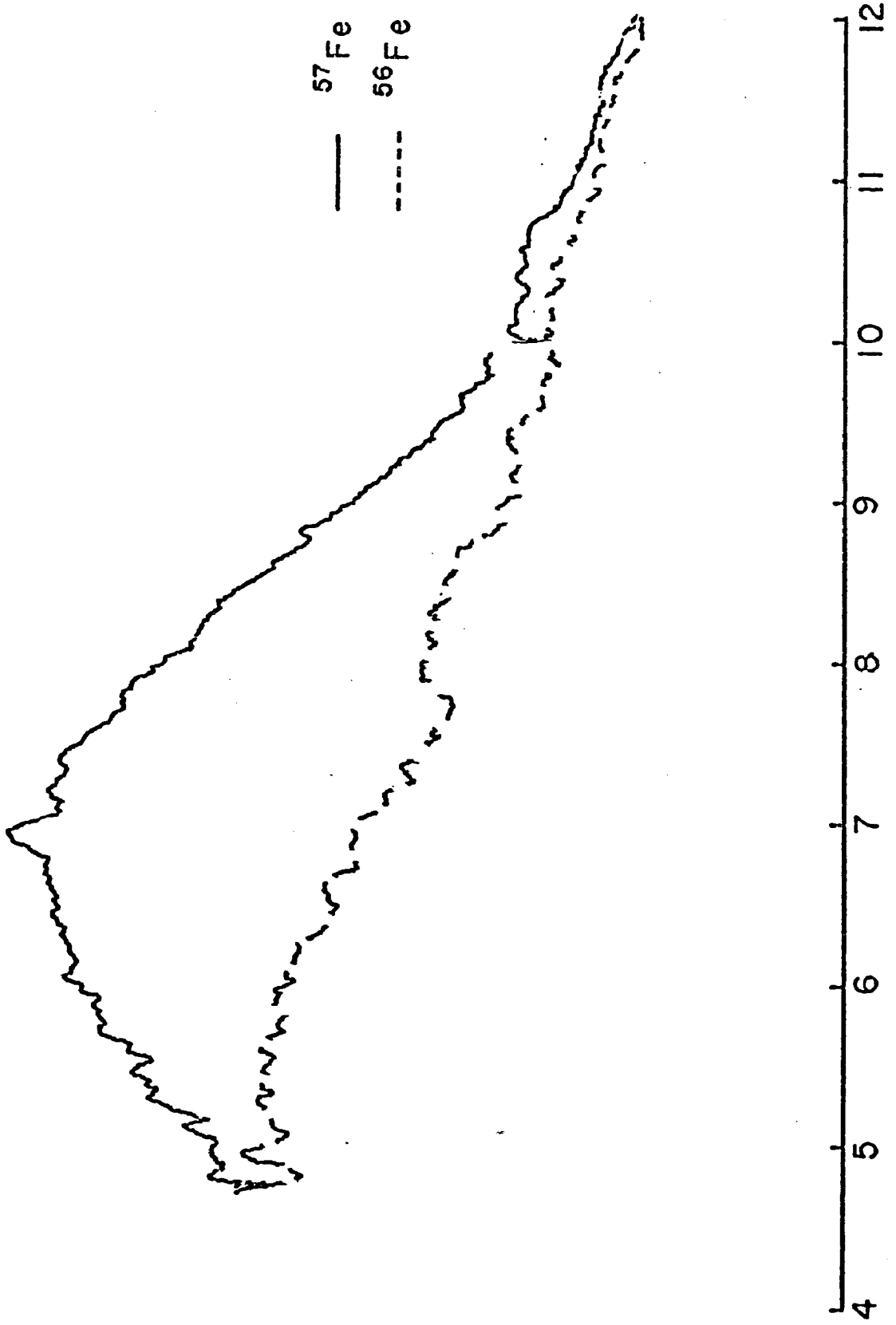


Figure 29. Experimental ^{56}Fe and ^{57}Fe (Ferrous) ENDOR Spectra at H_x

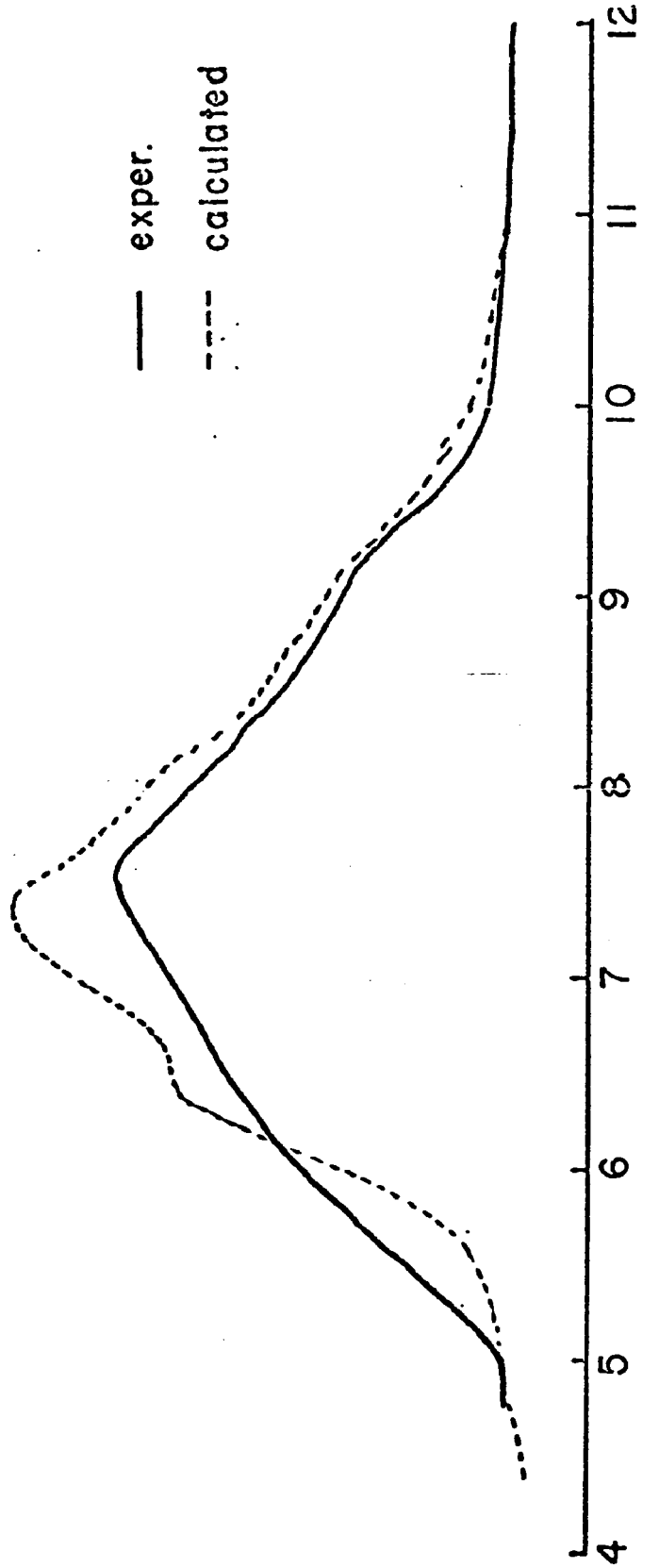


Figure 30. Experimental Difference and Calculated ENDOR Spectra at H_x

criterion. The experimental ENDOR parameters are summarized in Table 3.

3. Proton ENDOR

The H_x ENDOR spectrum of fully protonated algal ferredoxin in Tris-Cl buffer is shown in Figure 31. This spectrum begins at 7.5 MHz where the intensity is predominantly due to nitrogen (see below). The 10-20 MHz segment of Figure 31 shows six pairs of semi-resolved proton lines, centered at the free proton frequency (14.65 MHz at H_x) and split by their hyperfine value. Note that the two intensities of each pair need not be equal. There are also some less intense resonances contributing to this spectrum, some of which can be seen in the deuterated samples. None of these resolved resonances disappear if the sample is freeze-dried and soaked in D_2O, but a change in the overall shape does suggest that some unresolved protons are exchangeable; this too will be more apparent in the deuterated samples.

When the algae is grown on a fully deuterated medium, extracted in protonated phosphate buffers, transferred to Tris-Cl buffer, twice freeze-dried and taken up with D_2O, the ENDOR spectrum in Figure 32 is obtained. This sample has essentially the same concentration as that in Figure 31, but the amplifier gain is increased by a factor of about five. The spectrum at H_x of a deuterated sample extracted in totally deuterated phosphate buffers is shown in Figure 33; note that for this sample all the ENDOR intensity is due to

Table 3

Algal Ferredoxin Experimental Effective Hyperfine Constants

	$\lvert A'_x \rvert$	$\lvert A'_y \rvert$	$\lvert A'_z \rvert$	
Site I (Fe(III))	$51.6^{+0.2}_{-0.4}$	50.0 ± 2	$42.0^{+0.2}_{-0.5}$	MHz
(1.89, 1.96, 2.05)	$19.5^{+0.1}_{-0.2}$	18.2 ± 0.7	$14.6^{+0.1}_{-0.3}$	Electron Gauss
	$\lvert A_x \rvert$	$\lvert A_y \rvert$	$\lvert A_z \rvert$	
Site II (Fe(II))	$13.0^{+0.1}_{-0.5}$	15.0 ± 1.0	36.5 ± 0.5	MHz
(1.89, 1.96, 2.05)	$4.9^{+0.1}_{-0.2}$	5.4 ± 0.4	12.7 ± 0.2	Electron Gauss

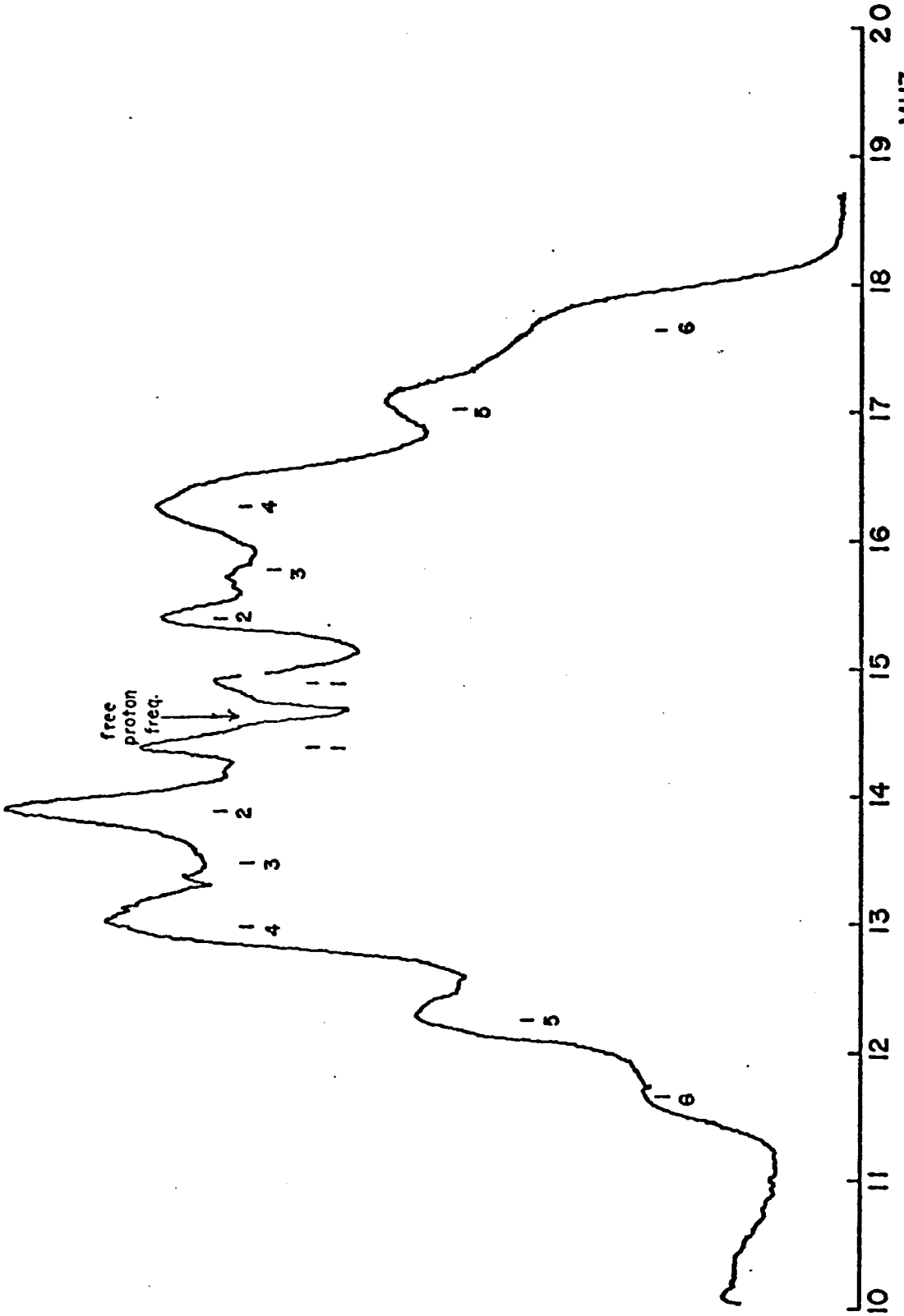


Figure 31. Experimental ENDOR Spectrum of Protonated Algal Ferredoxin at H_x

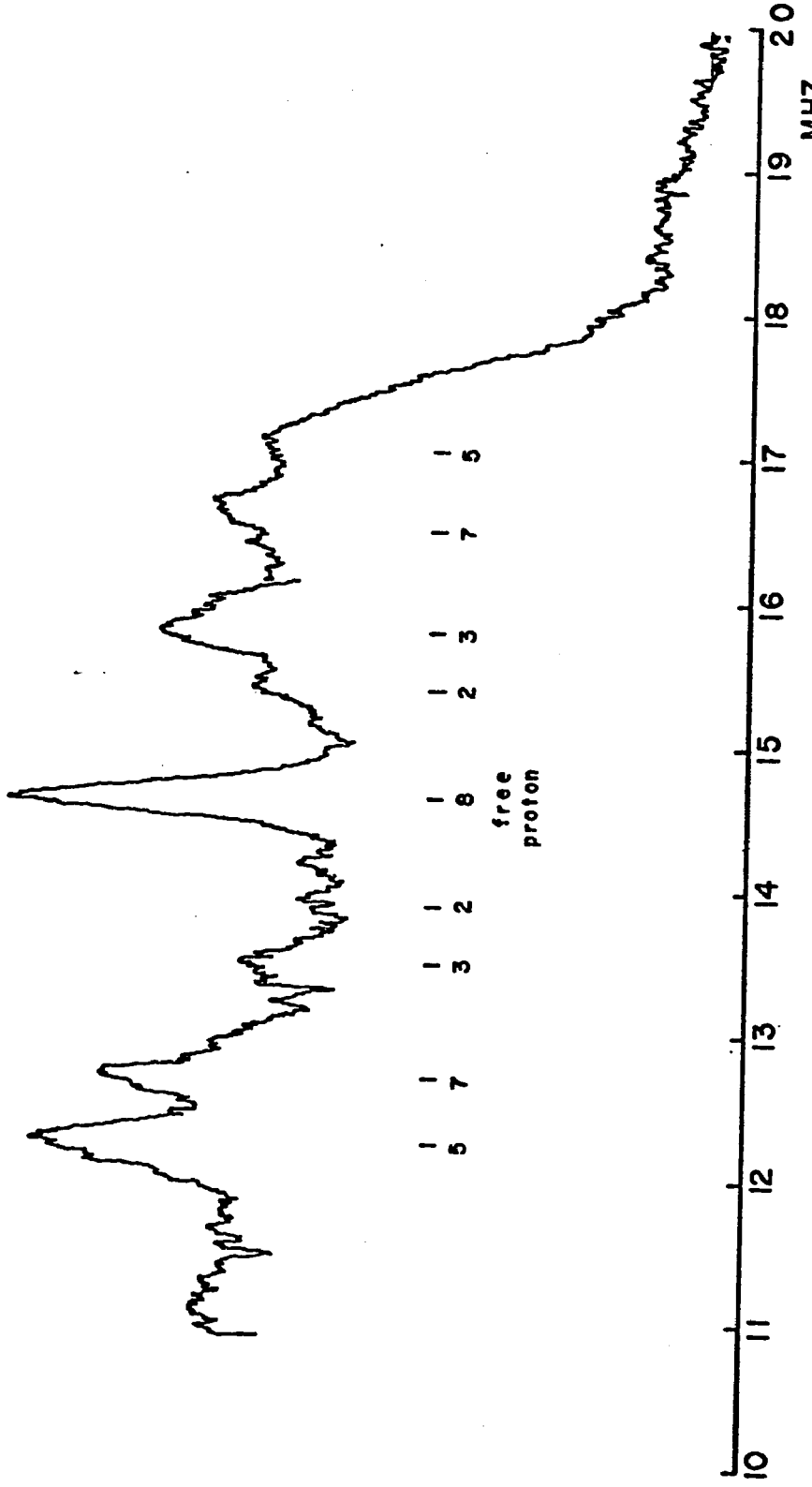


Figure 32. Experimental ENDOR Spectrum of Deuterated Algal Ferredoxin in Tris-Cl (in D_2O) at H_x

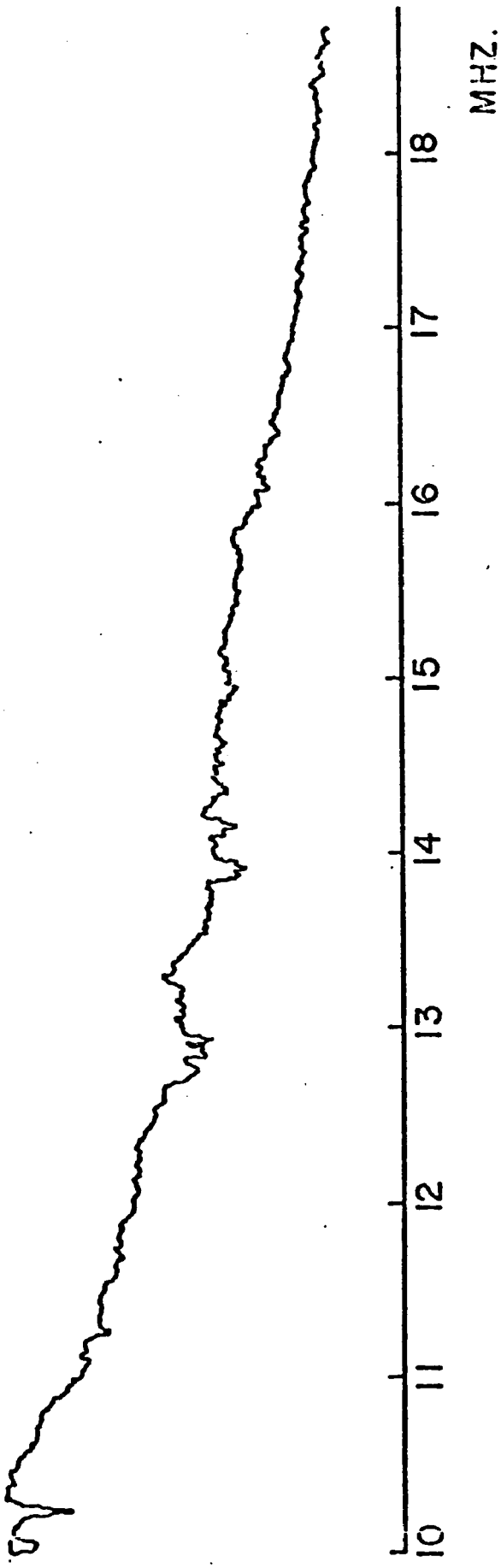


Figure 33. Experimental ENDOR Spectrum of Deuterated Algal Ferredoxin in Potassium Phosphate Buffer (D_2O) at H_x

nitrogen. The resonances seen in Figure 31 but not in 33 show that protons exchange on during protein isolation but do not totally reexchange, even if soaked in D_2O for one week. Notice also that protons #2, 3, and 5 appear in both Figures 31 and 32. These three protons, plus #7 (Figure 32) are exchangeable but exchange off with a time constant of about one week. The weakly coupled protons (#8) exchange quickly, except for those due to the nonexchangeable Tris protons. These Tris protons are weakly coupled to the unpaired spin and the intensity of the signal is related to the Tris concentration. There are no strongly coupled rapidly exchanging protons.

Figure 34 shows the same sample as Figure 32 but at H_z. In principal, one should be able to follow the movement of the proton lines and determine the proton distance from the unpaired electron, but this unfortunately was not possible due to the small intensities at some fields.

In order to obtain proton-free protein for iron ENDOR, it was necessary to reconstitute the samples in totally deuterated phosphate buffers. Apparently the slowly exchanging protons quickly exchange in the apoprotein state and/or when the pH is altered during the denaturation. The reconstituted protein has an ENDOR spectrum free of protons and the ^{56}Fe sample has spectra identical to that in Figure 33.

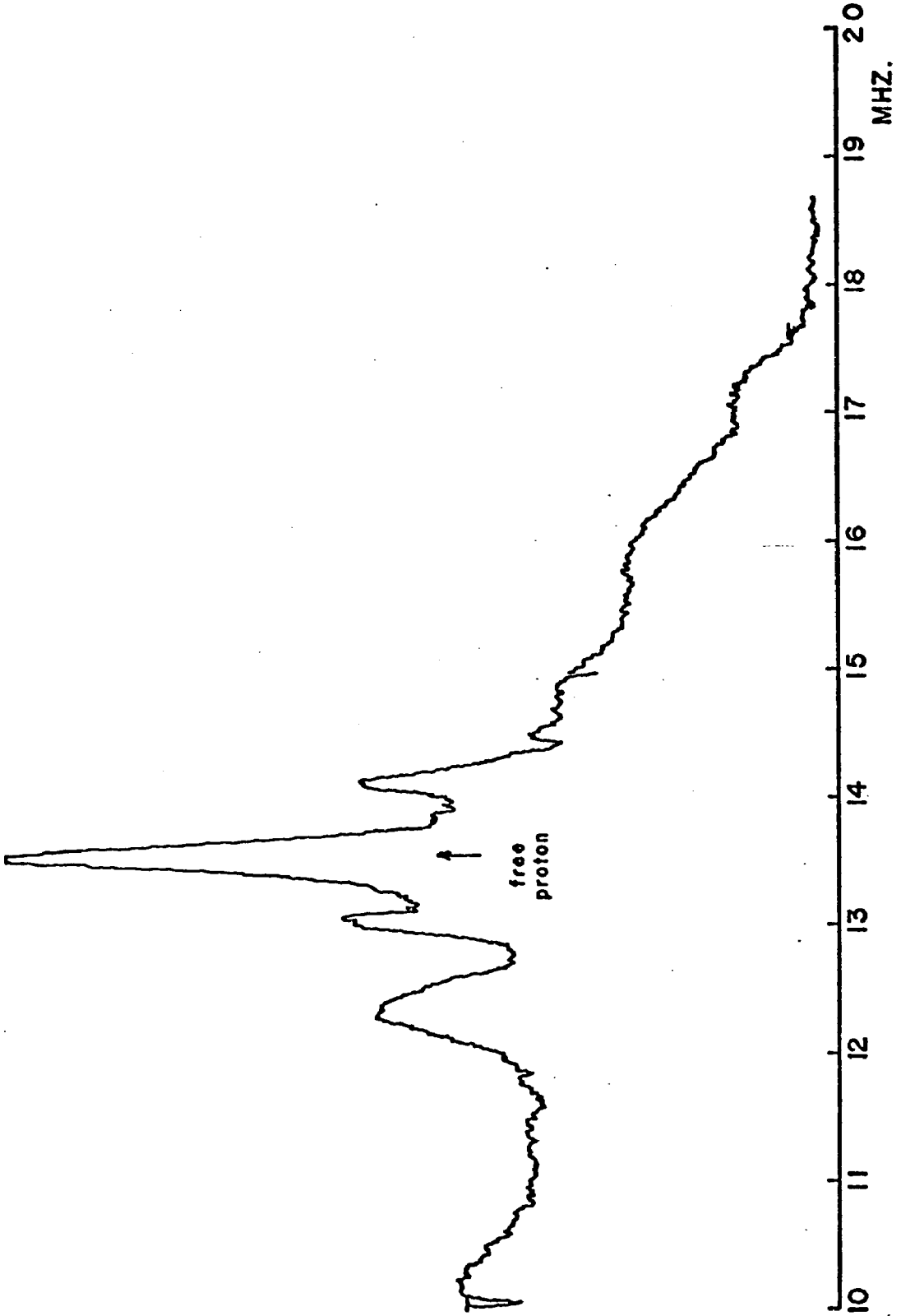


Figure 34. Experimental ENDOR Spectrum of Deuterated Algal Ferredoxin at H_z

4. Nitrogen ENDOR

The question of the baseline sloping from 1.3 MHz to 20 MHz prompted a comparison of ^{14}N versus ^{15}N ferredoxin. Since no S. lividus ferredoxin was available with ^{15}N, a ferredoxin from Chlorella vulgaris was used. The EPR of this sample is shown in Figure 35 and it is clear by inspection of the spectrum that the sample is probably of the spinach ferredoxin type, but that there are impurities in both samples. Since the low frequency ENDOR signals are similar in all ferredoxins, this sample was used with good justification.

Figure 36 shows that for ^{14}N, the ENDOR spectrum is similar to that seen in the low frequency ferrous ENDOR data for S. lividus. The spectrum of ^{15}N in Figure 36 shows two broad resonances, the improved resolution arising from the fact that ^{14}N is broadened because of its quadrupole moment while ^{15}N has $S = 1/2$ and no quadrupole moment. The resonances at H_z occur at 3.1 and 5.2 MHz, while at H_x they occur at 3.2 and 5.6 MHz. At H_z the two resonances should normally be separated by 2.7 MHz, but the experimental separation is approximately 2.1 MHz; a similar discrepancy occurs at H_x.

One possible conclusion is that the observed resonances arise from a single nitrogen atom and that the deviation from the theoretical splitting is due to second order effects. Unfortunately all second order effects for these fields should only be on the order of 5%, not

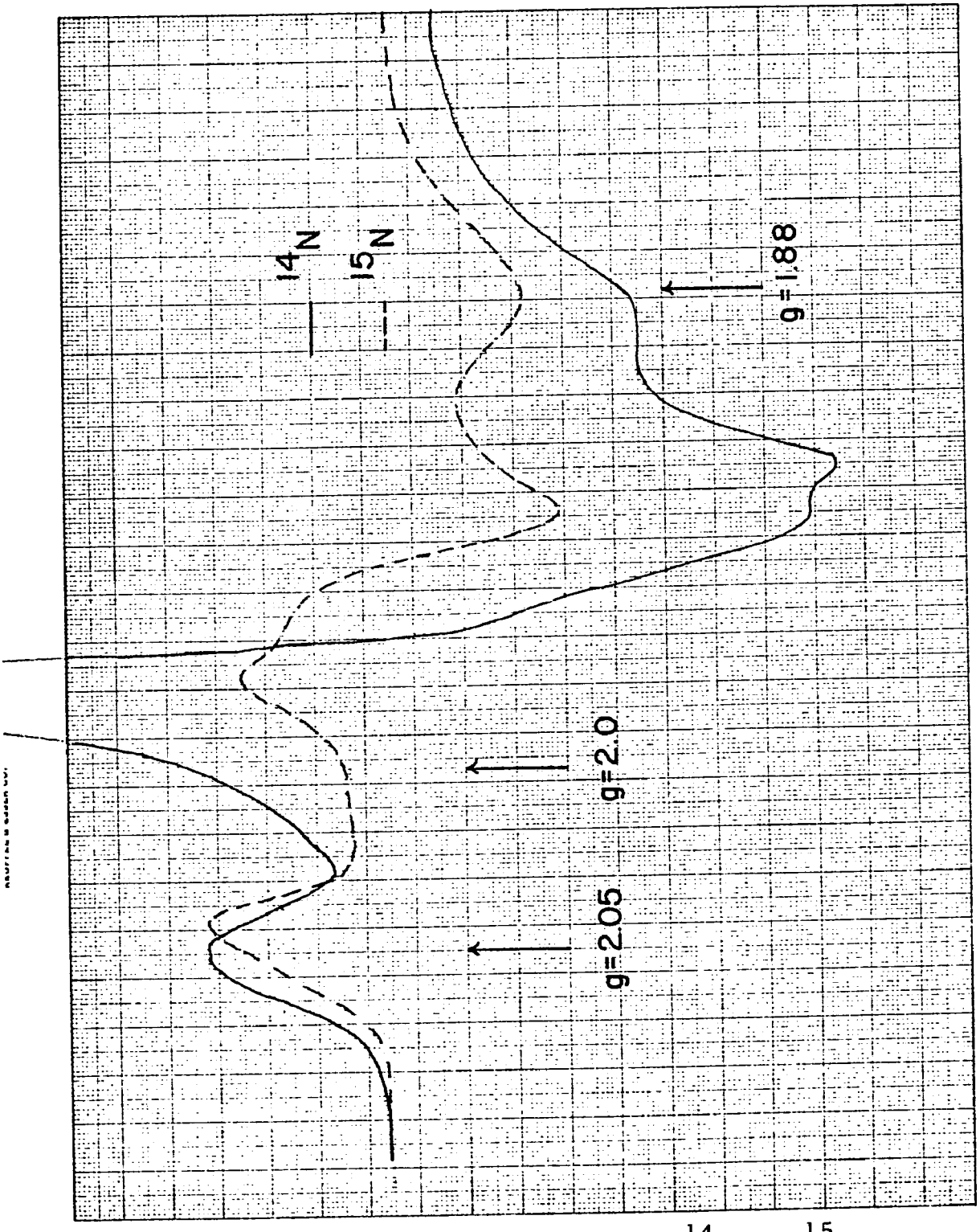


Figure 35. Experimental EPR Spectrum of ^{14}N and ^{15}N Chlorella Vulgarus Ferredoxin

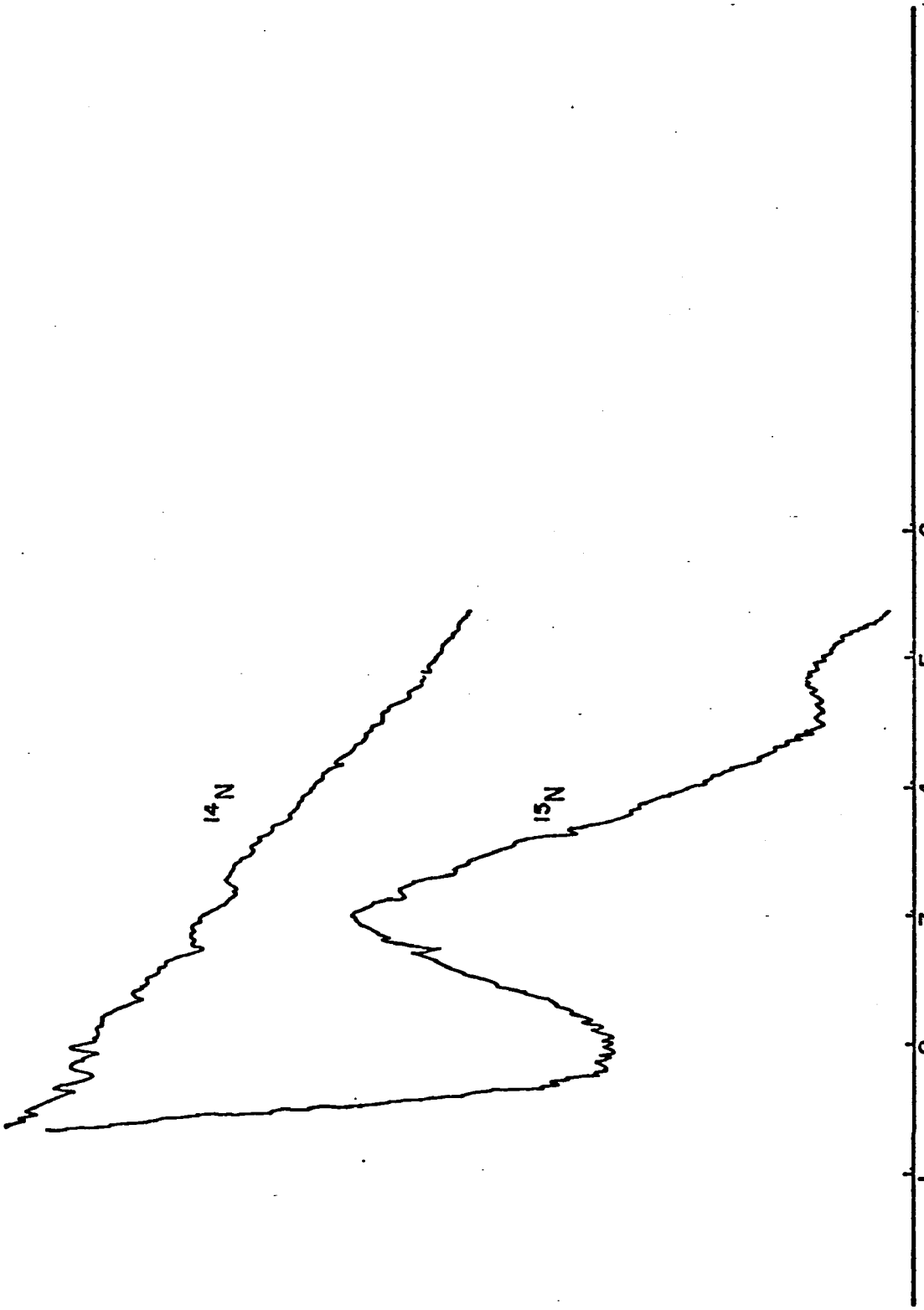


Figure 36. Experimental ^{14}N and ^{15}N ENDOR of Chlorella Vulgaris Ferredoxin at H_x

20% as needed. A second alternative is that two nitrogen atoms are being observed, but for some reason the second member of each pair is not being observed. For instance, the pair of the weak 5.2 MHz line might be at 2.5 MHz, beneath the large absorption at 3.1 MHz; the pair to the latter resonance could in turn be at 0.4 MHz, below the spectrometer range. Since ENDOR pairs can have very unequal transition probabilities, neither of the above alternatives can be ruled out on the basis of intensity.

A third alternative is to question the accuracy of the data. One motivation for this is the condition of the sample as judged by EPR; the obvious solution of further purification is excluded by the fact that the sample is already too weak for good ENDOR, and the reoxidation-repurification would result in further losses. Another reason to question the data is the uncertainty and technical difficulties associated with the ENDOR spectrometer at these frequencies. These include the fact that the sweep range at this frequency is only 1.5 MHz, and the presence of the as yet unexplained broad absorption which increases at lower frequencies.

In spite of all the uncertainties, the essential conclusion still remains valid; there is at least one nitrogen atom near the ferredoxin active site. Furthermore, its hyperfine interaction is nearly isotropic and on the order of 8 MHz. It is difficult to reliably estimate the spin density on the nucleus, but the fact that it is finite is valuable when considering the active site environment.

D. Mossbauer Effect Results

1. Oxidized rotein

The results for the low temperature (4.2°K) Mossbauer spectroscopy of oxidized algal ferredoxin are shown in Figures 37 and 38. The low field data (H = 580 gauss) shows a single quadrupole pair with a Q.S. of 0.7 mm/sec and an isomer shift (relative to platinum) of -0.13 mm/sec. Although the resonance positions can be simulated with the above parameters, the linewidths cannot. This shape can, however, be fit with a single quadrupole pair by increasing the linewidth from the instrumental linewidth of 0.15 mm/sec to 0.2 mm/sec. An alternative procedure is to use two quadrupole pairs, one $Q.S._1$ of 0.83 mm/sec and another $Q.S._2$ of 0.55 mm/sec, each with the same isomer shift and linewidths of 0.17 mm/sec; this fit at low field is somewhat better than the large linewidth fit. The two site fit is shown in Figure 37.

The low field data is identical at 4.2°K and 77°K (Figure 39) indicating that over this range, Q.S. is independent of temperature.

At high field the nuclear Zeeman interactions become important resulting in the additional structure observed in Figure 38. The simplest simulation assumes the single Q.S. and isomer shift from the low field data while eta and the sign of Q.S. are varied for a best fit. A sign change in Q.S. results in the mirror image spectrum, that is, it corresponds to a reversal of the sign of the velocity axis. An eta less than one results in an asymmetry about the zero velocity

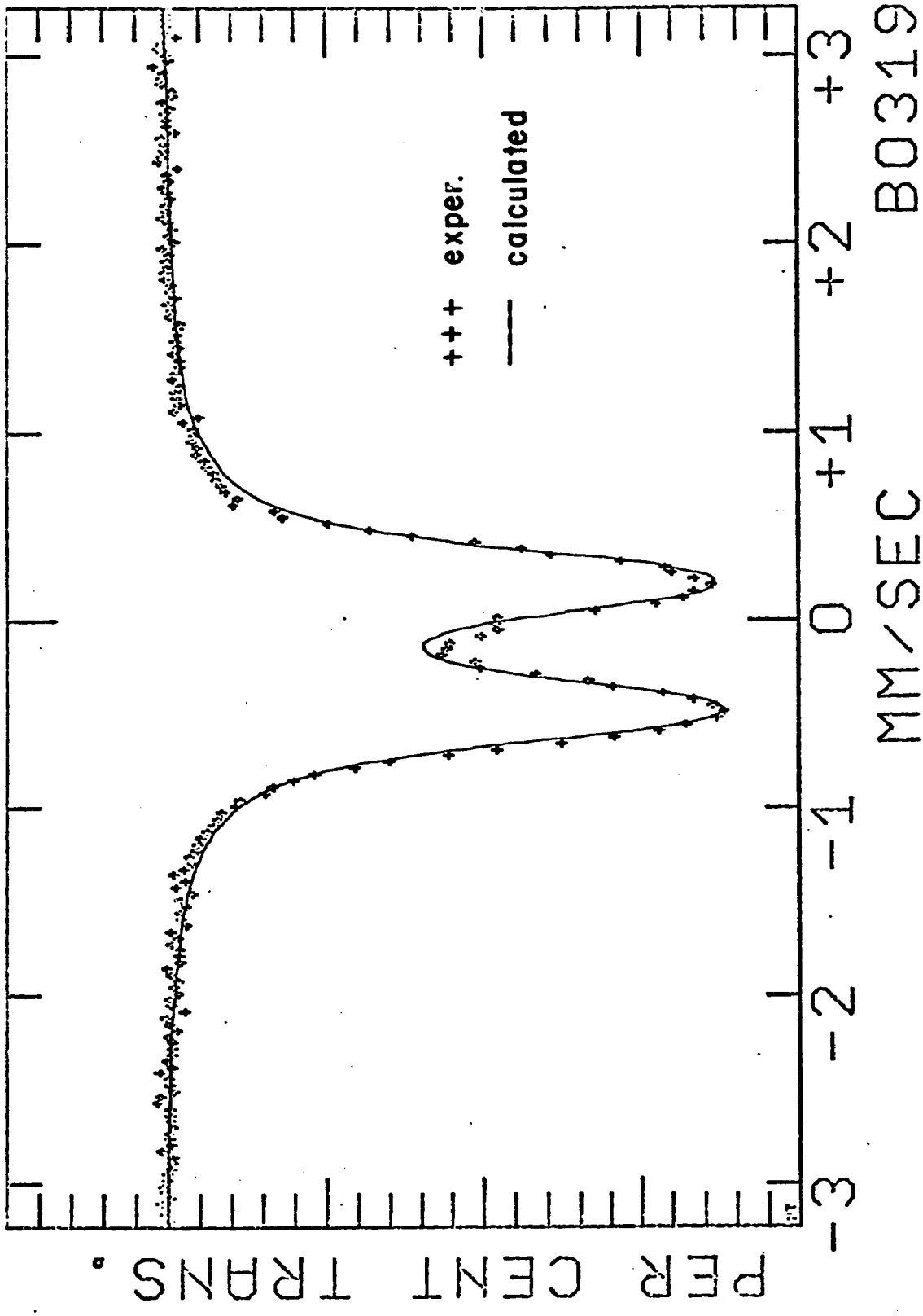


Figure 37. Experimental and Computed Mossbauer Spectra for Oxidized Algal Ferredoxin ($T = 4^{\circ}K$, $H = 0$)

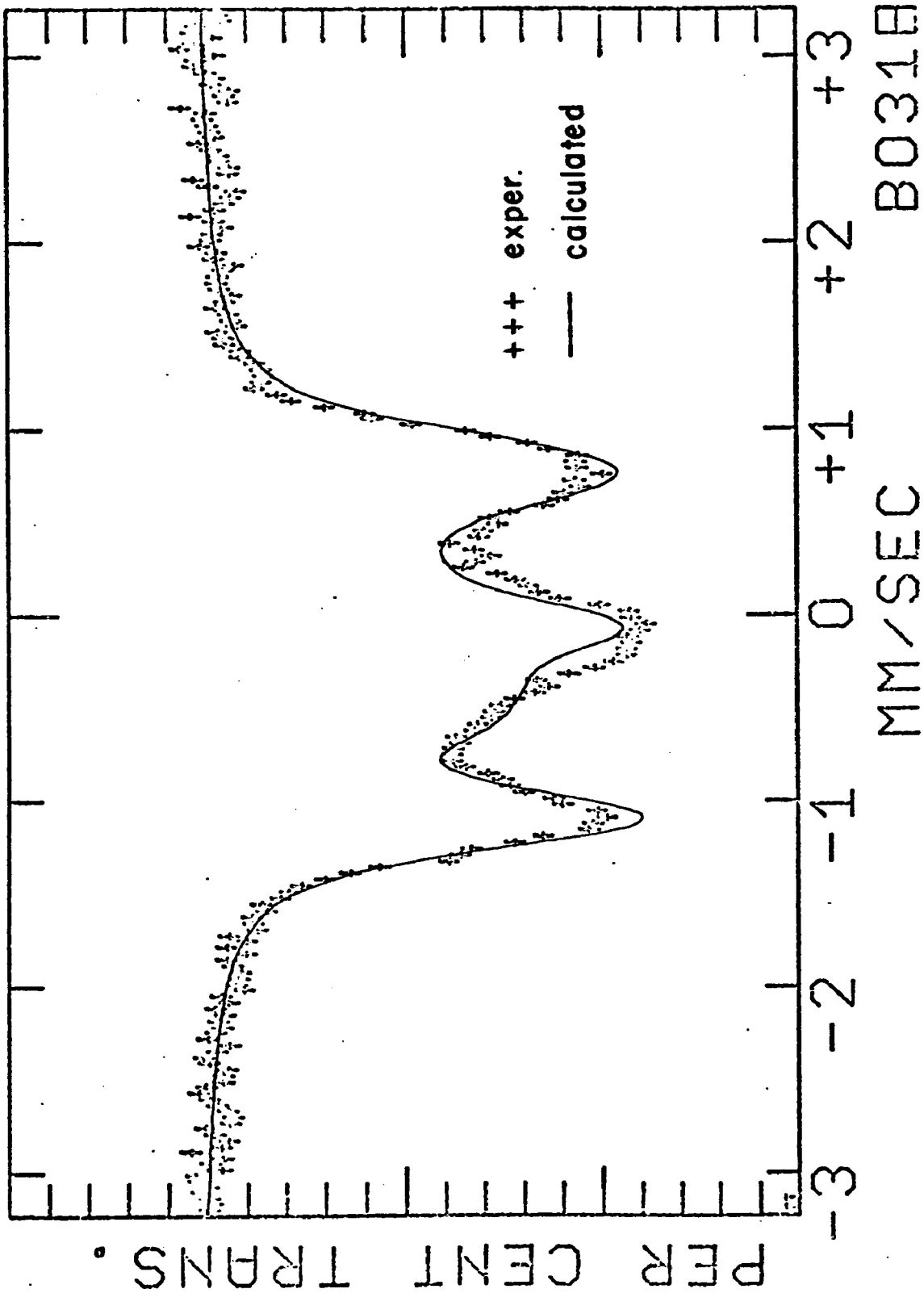


Figure 38. Experimental and Computed Mossbauer Spectra for Oxidized Algal Ferredoxin ($T = 4^{o}K$, H = 46 K Gauss)

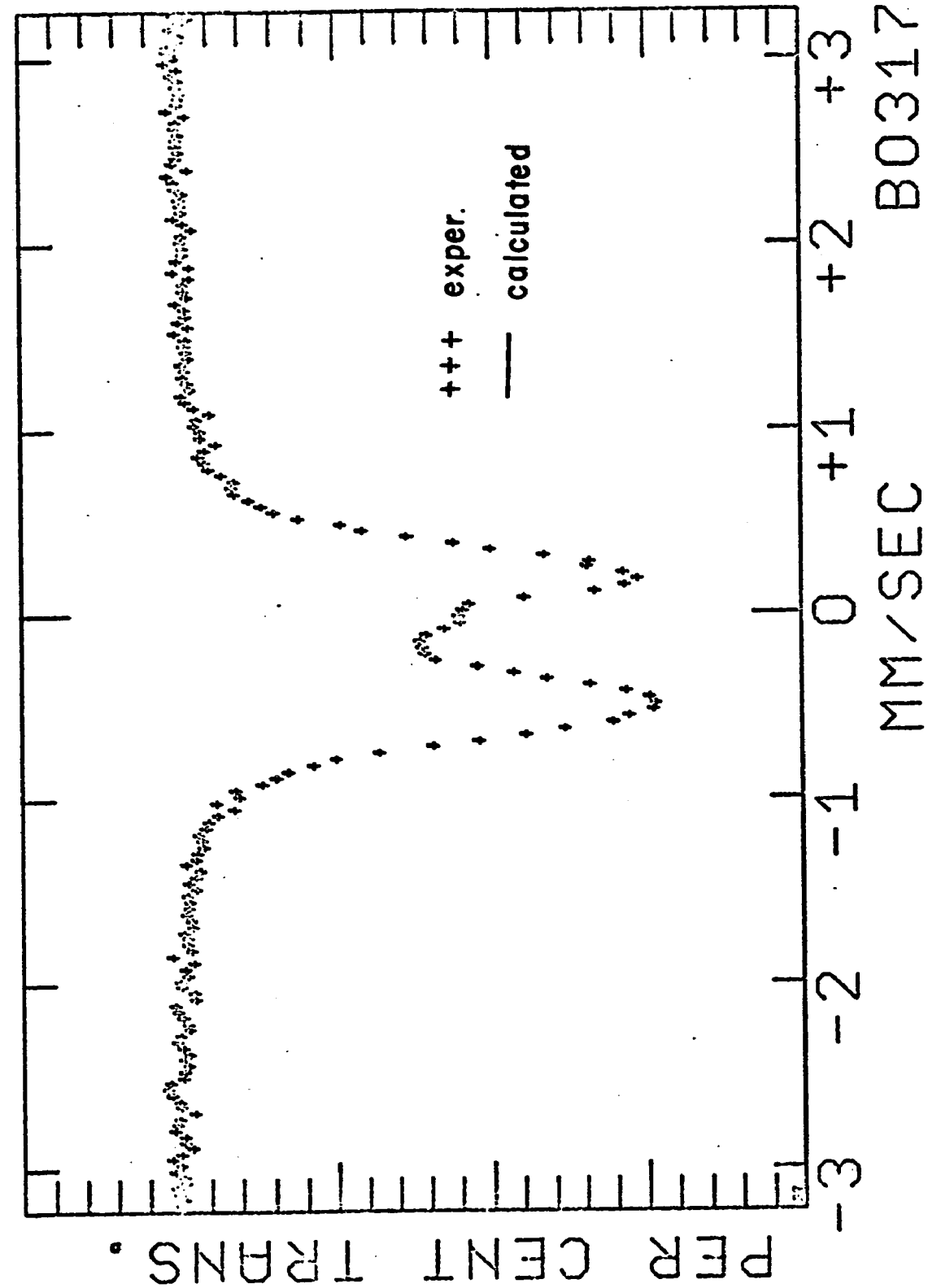


Figure 39. Experimental Mossbauer Spectra for Oxidized Algal Ferredoxin ($T = 77^{o}K$, $H = 0$)

point; for this data eta principally affects the shapes near zero velocity. The fit obtained in this manner (with 0.2 mm/sec linewidths, Q.S. = +0.7, I.S. = -0.13 mm/sec, eta = -0.5) is fairly good, except in the center region. A better fit is obtained for the two quadrupole pair model with both quadrupole splittings positive, the central peak region is better but it still does not fit well.

A more severe problem with the Mossbauer data of the oxidized protein occurs at 77°K, H = 46 K gauss, shown in Figure 40. This structureless spectrum suggests that there is some paramagnetism at 77°K, but the magnetic susceptibility demonstrated that the protein is essentially diamagnetic below 90°K. The small amount of paramagnetism that might be present at 77°K should not be significant. The data can be simulated quite well using very large linewidths (3 mm/sec) but since the effect is field dependent, this still requires some paramagnetism. No final explanation for this data is offered at this time.

The Mossbauer results seem to indicate that the oxidized protein has essentially a single environment for both iron atoms. The fact that the single quadrupole pair with instrumental linewidths cannot fit the data suggests that the two iron atoms may have slightly different environments, or that there is a distribution of environments due to protein microheterogeneity; this latter explanation is analogous to the "g-strain" (presumably due to similar causes) which is invoked to explain the broad EPR linewidths. Whatever the explanation is,

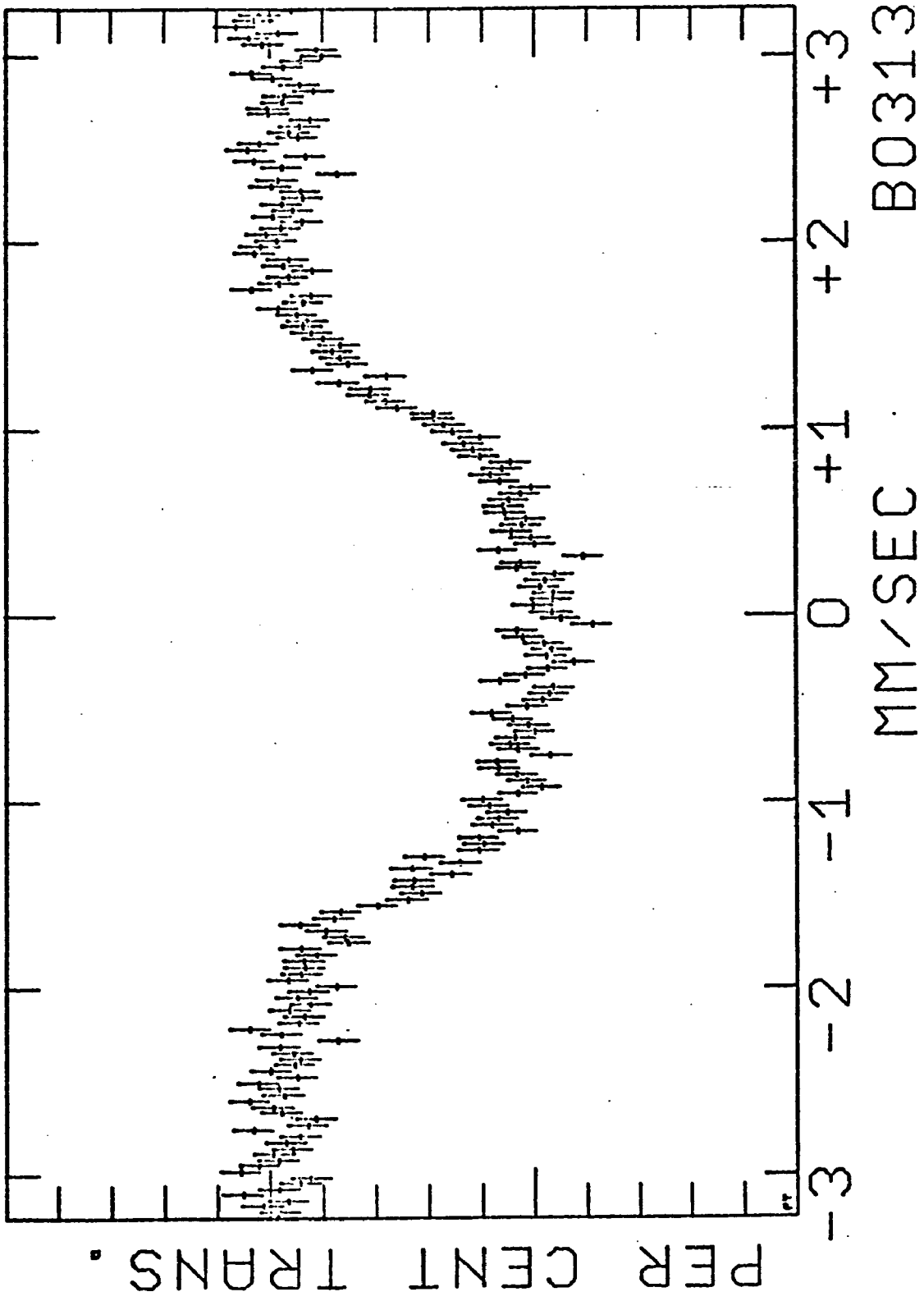


Figure 40. Experimental Mossbauer Spectra for Oxidized Algal Ferredoxin ($T = 77^{o}K$, H = 46 K Gauss)

the small magnitude of Q.S., or the average Q.S., indicates that the iron is probably high spin ferric; since high spin ferric iron is a spherically symmetric $3d^5$ ion, the finite electric field gradient is presumably due to ligand asymmetries. None of the above conclusions account for the 77°K field data, but conversely the conclusions are not dependent on an explanation for that data.

2. Reduced Ferredoxin

The Mossbauer effect spectra for high temperature (250°K) reduced algal ferredoxin is shown in Figure 41 (H = 580 gauss) and Figure 42 (H = 46 K gauss). These high temperature spectra are characteristic of two nonequivalent quadrupole pairs with no evidence of any average internal fields. As was done for the oxidized protein, the magnitudes of Q.S. and the isomer shift are determined by fitting the low field high temperature data. One pair, due to the iron called Site I, has the same Q.S. and eta as the oxidized protein; the small Q.S. (0.6 mm/sec) indicates again a nearly spherically symmetric electric field at the nucleus. The other iron, called Site II, has a very large quadrupole splitting (2.69 mm/sec) and an isomer shift of +0.13 mm/sec. As for the oxidized protein, the above data fits the line positions but not the shapes. The fact that the site I pair has an amplitude greater than that calculated can be accounted for by an incomplete sample reduction. Presumably the dithionite was not in excess or else the reduction was not sufficiently anaerobic and partial reoxidation occurred. An amplitude ratio of 0.6/0.5 (Site I/Site II)

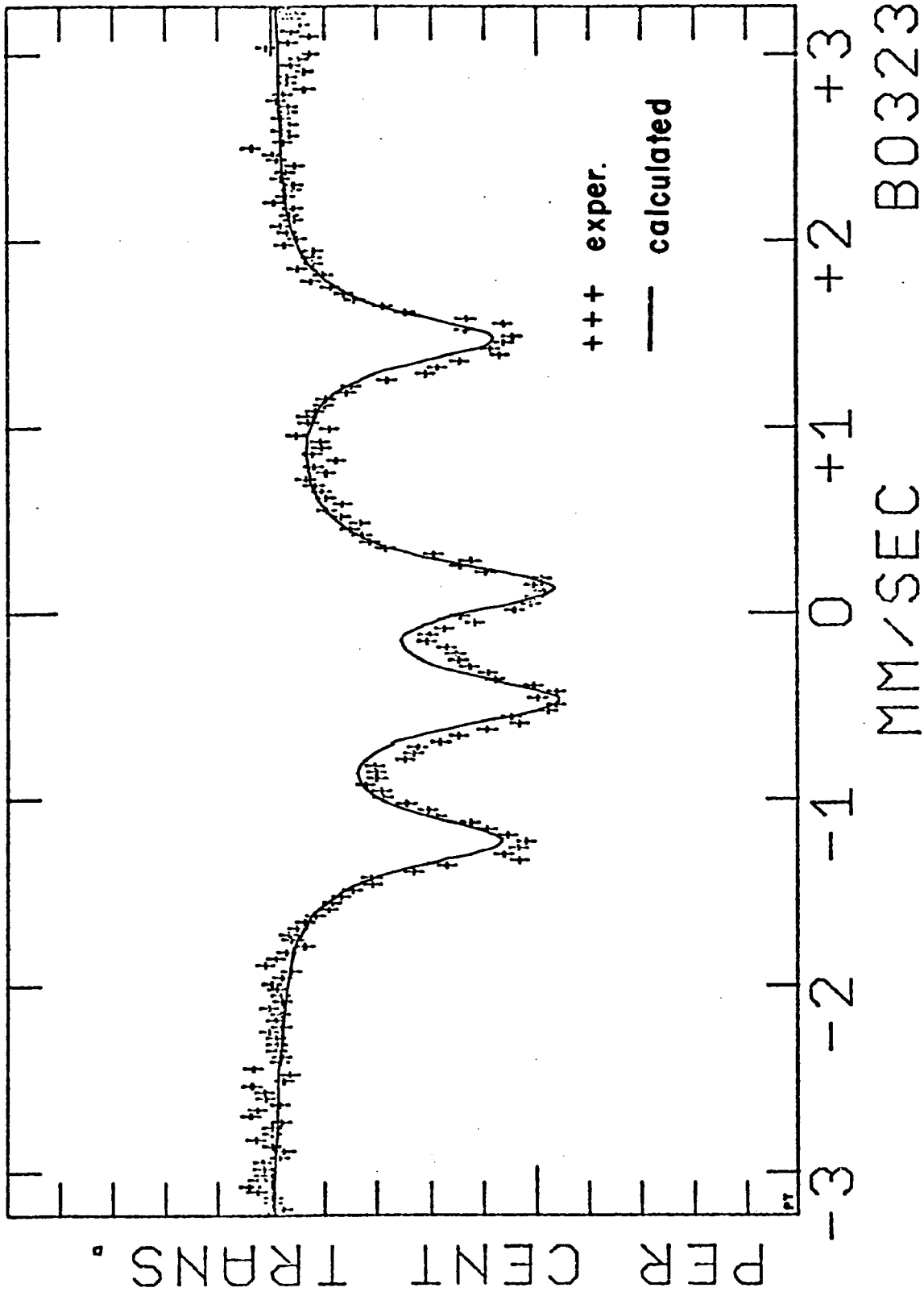


Figure 41. Experimental and Computed Mossbauer Spectra for Reduced Algal Ferredoxin ($T = 250^{\circ}K$, $H = 580$ Gauss)

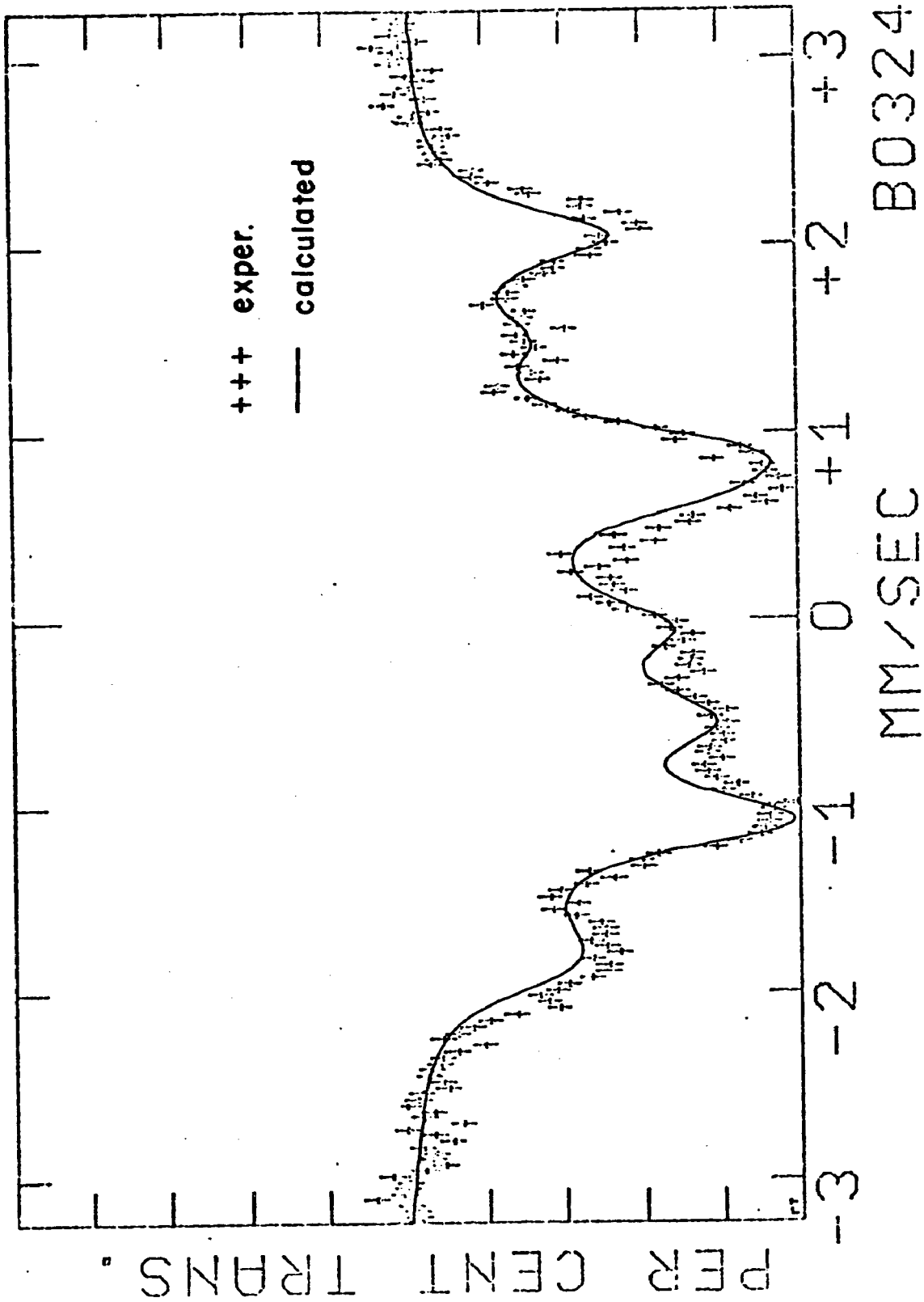


Figure 42. Experimental and Computed Mossbauer Spectra for Reduced Algal Ferredoxin ($T = 250^{o}K$, $H = 46$ K Gauss)

will fit the experimental amplitudes. The linewidths used for the high temperature data are 0.2 and 0.17 mm/sec for Site I and Site II respectively. One possible explanation for these linewidths is that the relaxation rates may be different for the two iron atoms. This would occur if at high temperature the exchange coupled spins are somewhat uncoupled and if their spins are different. It will be shown below that the two sites do indeed have different spins. A second possible explanation for the linewidths is that at 250°K there may still be incomplete averaging of the hyperfine fields. Site I will be shown below to have the larger hyperfine field and thus it would have the larger linewidth if the above is true. A third explanation would attribute the Site I broadening to $Q.S._1$ being slightly different from the assumed 10% oxidized protein contaminant. The validity of any of the above is not certain, and the question of experimental linewidths greater than instrumental linewidths remains unresolved.

Since Q.S. is the same for the oxidized protein and Site I of the reduced protein, its sign and the value of eta are assumed for the high temperature high field simulations. The sign of Q.S. for Site II is found to be negative and a value of eta equal to zero is marginally preferred over an eta equal to one. The large negative Q.S. establishes (32) that site II is high spin ferrous iron. If one assumes the single quadrupole pair fit to the oxidized data, then the fact that the Site I parameters are the same implies that the reducing electron is mostly on Site II and doesn't affect the Site I electric field.

An alternative interpretation for the oxidized protein assumes two nonequivalent iron sites. The fact that the Site I Q.S. in the reduced state is not equal to either of the oxidized quadrupole splittings then shows that the Site I electric field is altered by the reducing electron. This explanation is intuitively more reasonable but neither model can be confirmed at this time. For either case 10% extra Site I iron and linewidths greater than theoretical are required to fit the data.

At low temperatures (4.2°K) electron relaxation rates are slowed to the point where any paramagnetic internal fields have a lifetime greater than the nuclear precession time. This effect is observed in the low field (580 gauss, Figure 43) and high field (46 K gauss, Figure 44) Mossbauer data. Since even the weak magnetic field is enough to align the spin moments, the effective field at the nucleus is given by the sum of the applied field and the internal fields due to the hyperfine interactions. This can be written,

$$H_{eff} = H_{applied} - \frac{A_1 m_s}{g_n \beta_n H} - \frac{A_2 m_s}{g_n \beta_n H}$$

where A_1 and A_2 are here written as scalars although they are in fact tensors. A typical hyperfine value of 40 MHz will result in an effective field of approximately 15 K gauss in magnitude and oriented parallel or antiparallel to $H_{applied}$ depending on the sign of m_s. When the applied field is small with respect to the internal fields, the two spin states will exhibit identical Mossbauer spectra; this is the case shown in Figure 43. The calculated simulation assumes the

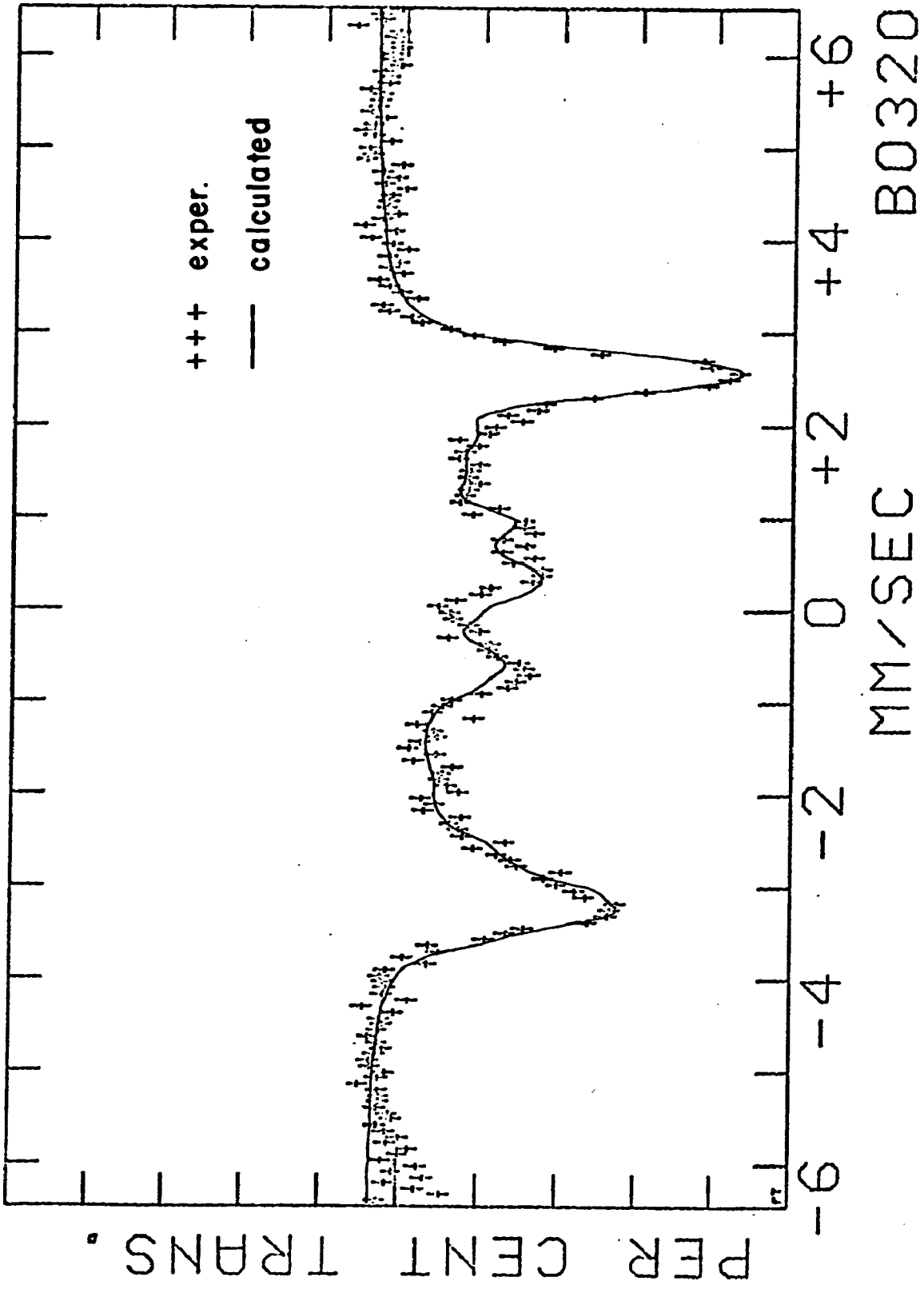


Figure 43. Experimental and Computed Mossbauer Spectra for Reduced Algal Ferredoxin ($T = 4^{o}K$, H = 580 Gauss)

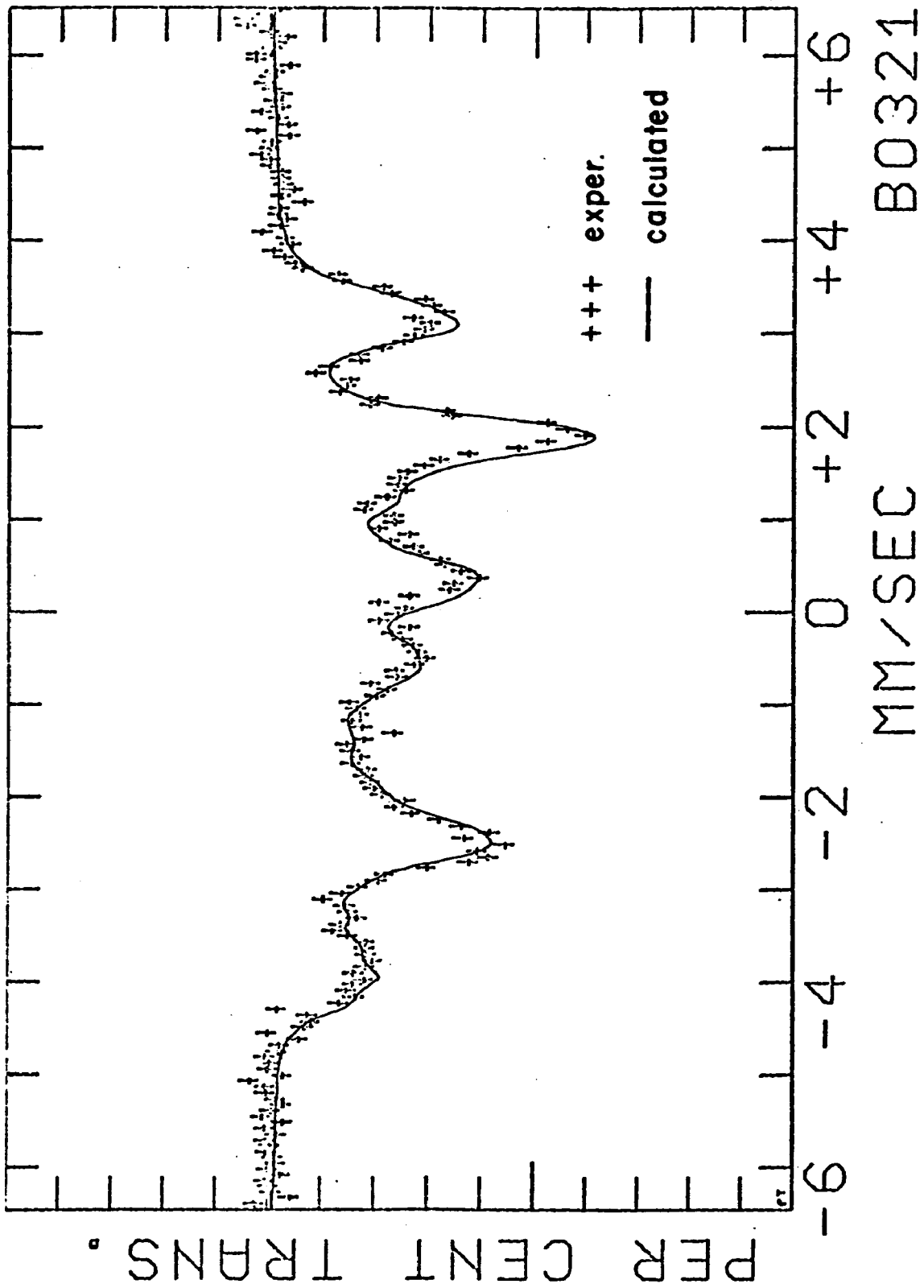


Figure 44. Experimental and Computed Mossbauer Spectra for Reduced Algal Ferredoxin ($T = 4^{o}K$, H = 46 K Gauss)

magnitudes of the hyperfine tensors from the ENDOR data (Table 3), the EPR g-values, and the Site I Q.S. and eta from the high temperature Mossbauer data. Site I Q.S. is assumed to be independent of temperature because of its similarity to the oxidized temperature independent Q.S; Q.S. and eta for Site II are treated as free parameters. Q.S. is found to be temperature dependent for Site II and its magnitude increases from -2.69 mm/sec at high temperature to -3.2 mm/sec at low temperature, indicating that at the higher temperatures an excited state with a smaller or opposite Q.S. has a finite Boltzmann population; this temperature dependent Q.S. is consistent with the first electron excited state lying 430 cm^{-1} above the ground state. The rotation of the Site I hyperfine tensor relative to the g-tensor, as indicated by the ENDOR results, measurably improves the fit at both high and low fields. Since no data is available for the quadrupole orientation, it was assumed coincident with the g-tensor. This should be a reasonable assumption since both tensors arise from the crystal field.

The low temperature high field spectra consists of four spectra (weighted by their Boltzmann factors), two each for $m_s = -1/2$ and $m_s = 1/2$; the Boltzmann ratio at 4.2°K and 46 K gauss applied field is 3.3. The simulation requires that the Site I ground state ($m_s = -1/2$) hyperfine field be aligned antiparallel to the applied field while the Site II ground state is aligned parallel. The expression for H_{eff} shows that the above effect can only be explained if the two sites have hyperfine

tensors with opposite signs; the Site I principal A-values must all be negative while those of Site II are all positive. Watson and Freeman (36) have shown, however, that the contact hyperfine interaction for both ferric and ferrous iron is necessarily negative, hence m_s for Site II must be positive for the dominant Boltzmann Term. Since Site II is known to be high spin ferrous by its large negative quadrupole splitting, the only way for Site II to have a positive net spin is for the S = 2 ferrous to be antiferromagnetically coupled to a spin larger by 1/2, that is S = 5/2; therefore Site I must be high spin ferric. This conclusion is consistent with both the magnetic susceptibility data, the small site I Q.S., and the nearly isotropic Site I hyperfine tensor. The low temperature data requires that $\eta = 0$.

The near identity of oxidized protein and Site I reduced protein Mossbauer data requires that the oxidized ferredoxin have both iron atoms in the high spin ferric state. The lack of any internal fields in the oxidized protein agrees with the diamagnetism at those temperatures as shown by the magnetic susceptibility; the two 5/2 spins are again antiferromagnetically coupled to result in net S = 0.

The orbital symmetry for the sixth electron in the ferrous iron can be determined from the Mossbauer data. Reference to Table 2 shows that the negative Q.S. for the ferrous iron, Site II, restricts the orbital to d_{z^2}, d_{xz}, or d_{yz}; an eta of approximately zero eliminates all of these possibilities except d_{z^2}. The conclusion is that the paired electrons are in a d_{z^2} orbital. It will be shown in

the next section that the hyperfine tensor determined by the ENDOR experiments also establishes the filled orbital as d_{z^2}. Since the factor $\langle r \rangle^{-3}$ is common to both the anisotropic hyperfine tensor and the quadrupole splitting, comparisons of the magnitudes would also be possible except that terms such as the quadrupole moment for the excited ^{57}Fe are not well known.

All of the experimental Mossbauer parameters are summarized in Table 4.

Table 4

Mossbauer Parameters for Oxidized and Reduced Algal Ferredoxin

A. Oxidized Ferredoxin

I.S./Pt (mm/sec)	-0.13 ± 0.02	
Q.S. (mm/sec)	a) 0.55 & 0.83 ± 0.04	2 sites
	b) 0.70 ± 0.04	1 site
Eta	0.5 ± 0.3	

B. Reduced Ferredoxin

	Ferric	Ferrous
a) High Temperature		
I.S./Pt (mm/sec)	-0.15 ± 0.02	0.13 ± 0.02
Q.S. (mm/sec)	0.60 ± 0.02	-2.69 ± 0.02
b) Low Temperature		
I.S./Pt (mm/sec)	-0.20 ± 0.02	0.07 ± 0.02
Q.S. (mm/sec)	0.60 ± 0.02	-3.20 ± 0.1
Eta	-0.3 ± 0.3	0.0 ± 0.2
g_x*	1.89	
g_y	1.96	
g_z	2.05	
A_x (MHz)**	$-51.6\ {}^{+0.2}_{-0.4}$	$13.0\ {}^{+0.1}_{-0.5}$
A_y (MHz)	-50.0 ± 2.0	15.0 ± 1.0
A_z (MHz)	$-42.0\ {}^{+0.2}_{-0.5}$	36.5 ± 0.5

* g-values from EPR
** Effective A-values from ENDOR

CHAPTER 6

CONCLUSIONS

The results of the previous section provide substantial support for a model proposed by Gibson et al. (37) in 1966. These authors sought to explain the observed g-values in reduced spinach ferredoxin by assuming that a high spin ferric ($S_1 = 5/2$) was antiferromagnetically exchange coupled to a high spin ferrous ($S_2 = 2$) iron resulting in an effective spin, $S = 1/2$. For the coupled spin system, the individual spin moments precess about the resultant spin at a rate fast with respect to the precession rate of the total spin. This results in only the projection of the individual spin moments along the net spin having an average nonzero expectation value. The electronic Zeeman Hamiltonian must now be written,

$$\mathcal{H} = \beta H\left(g_1 \frac{S_1 \cdot S}{S^2} + g_2 \frac{S_2 \cdot S}{S^2}\right) \cdot S$$

$$= g \beta H \cdot S$$

The effective g-value is calculated assuming $S_1 = 5/2$, $S_2 = 2$, $S = 1/2$ giving

$$g_{eff} = \frac{7}{3} g_1 - \frac{4}{3} g_2$$

The negative sign results from the antiferromagnetic coupling. If one assumes that g_1 (ferric) is isotropic and equal to 2.019 (38) then the real ferrous g_2 values can be calculated from the experimental

effective g-values (see EPR Results, Chapter 5B). For algal ferredoxin the real ferrous principal g-values are,

$$g_x = 2.12$$

$$g_y = 2.06$$

$$g_z = 2.00$$

Gibson et al. (37) sought to explain the ferrous g-values by assuming that the iron electrostatic environment is approximately tetrahedral with rhombic distortions. The g-values for such a crystal field (see p. 25-26) for S = 2 are,

$$g_x = g_e + \frac{3\lambda}{2(\Delta_{xz-z^2})}$$

$$g_y = g_e + \frac{3\lambda}{2(\Delta_{yz-z^2})}$$

$$g_z = g_e$$

The spin-orbit coupling constant, λ, was reduced by these authors from the free ferrous ion case (λ = 400 cm^{-1}) to a lower value (λ = 300 cm^{-1}) because of assumed covalancy. With these assumptions the d_{yz} and d_{xz} orbitals are above d_{z^2} by 6000 cm^{-1} and 3750 cm^{-1} respectively.

The data presented in the previous sections confirms many of the assumptions made for the above model. The antiferromagnetic exchange coupling is confirmed by the temperature behavior of the magnetic susceptibility for both the oxidized and reduced protein. The same fact is confirmed (for the reduced protein) by the low

temperature Mossbauer simulations which require that the two hyperfine fields oppose; since the hyperfine interaction is necessarily negative for both iron atoms, this is only explained by the two spin projections being antiparallel. The spin states assumed by Gibson are also confirmed by the (reduced protein) Mossbauer experiments, which showed that the Site II (ferrous) quadrupole splitting is large and negative; this is consistent only with Site II being high spin ferrous. The Site I spin state is derived from the fact that Site II has spin 2 and a positive hyperfine field; this, as discussed in the Mossbauer Results, requires that Site I have a spin larger than 2 by 1/2, or S = 5/2. Thus there is indeed antiferromagnetic exchange coupling between a high spin ferric and a high spin ferrous iron atom.

The electrostatic environment at the active site is reflected most strongly in the electric field gradient, or Q.S. It was shown in the Mossbauer section that the negative Q.S. and zero asymmetry require that the lowest lying ferrous orbital is d_{z^2}, again consistent with the assumed basically tetrahedral symmetry. The same fact is confirmed by comparing the observed ferrous hyperfine values (Table 3) with the expressions calculated for the d-orbitals (Table 1). One can see that A_x and A_y being essentially equal and less than A_z is consistent only with d_{z^2} lying low. It is interesting to note just how well the experimental values agree with the calculated ones. Since the observed hyperfine fields are projected along the total S

direction, one must first calculate the real values in a manner directly analogous to the g-value calculation. In this case the hyperfine interaction is written,

$$\mathcal{H}_{hyp} = I_1 \cdot A_1 \cdot \left(\frac{S_1 \cdot S}{S^2}\right) S + I_2 \cdot A_2 \cdot \left(\frac{S_2 \cdot S}{S^2}\right) S$$

$$= \left(\frac{7}{3} A_1 I_1 - \frac{4}{3} A_2 I_2\right) \cdot S$$

Thus the effective hyperfine constants become $7/3\, A_1$ for Fe(III) and $-4/3\, A_2$ for Fe(II). Equating these expressions to the measured values, the real hyperfine values are deduced to be (see Table 3),

	Ferric	Ferrous
A_x	-21.2 MHz	-9.8 MHz
A_y	-20.4 MHz	-11.3 MHz
A_z	-18.0 MHz	-27.4 MHz

The above shows that the average real ferric hyperfine interaction is approximately 21 MHz. Watson and Freeman (39) have shown that the spin densities for ferric and ferrous ions are -3.00 and -3.29 (atomic units) respectively. If one assumes the same covalency for ferric and ferrous, these values allow one to calculate the ferrous contact term as

$$a_2 = \frac{-3.3}{-3.0} a_1$$

$$= 23 \text{ MHz}$$

Table 1 and the assumption that K = 0.35 (40) yields the anisotropic dipolar hyperfine contribution. The agreement between the calculated

and experimental hyperfine values is very good considering the simplifications which were assumed:

	Calculated	Experimental
A_x; A_y	16 MHz	13.0, 15.0 MHz
A_z	48 MHz	36.5 MHz

It is also interesting to note that the assumed covalency is reflected in the hyperfine interaction. For example, the above spin density value for a free ferric ion results (S = 5/2) in a hyperfine field of 630 K gauss at the nucleus (39). The observed field is only 380 K gauss (21 MHz/0.138 MHz/gauss). This shows that the iron hyperfine interaction is reduced by approximately 40% due to covalency and confirms the need for a reduction in the spin orbit coupling constant. Presumably the spin density is to a large extent on the ligands, but not involved in a direct iron-iron bond. If the latter were true, the addition of the reducing electron should have a considerable effect; the near identity of the oxidized and ferric quadrupole splitting suggests that the added electron is a minimal perturbation at the ferric iron. The high degree of covalency does, however, place serious doubts on any crystal field calculations, hence the use of pure d-orbitals is certainly an error. If, however, one does continue their use - for lack of an alternative - then again the temperature dependence of the ferrous quadrupole splitting requires, as discussed in the previous section, that there be an orbital approximately 430 cm^{-1} above d_z2; this is presumably $d_{x^2-y^2}$.

The question of the placement and purity of the d-orbitals rests ultimately with optical measurements. Recent studies comparing rubredoxin (having a known tetrahedral sulfur array around the single iron) and spinach ferredoxin have observed (41) two d-to-d absorptions at energies within 5% of those predicted by Gibson et al. (37).

CHAPTER 7

SUMMARY

The purpose of this study was to provide an accurate characterization of the magnetic interaction at the active site of a two iron ferredoxin from the algae Synechococcus lividus. The results from the techniques used were compared for internal consistency. The four techniques, the parameters measured by each and the source of the conclusions are listed below:

1. Magnetic susceptibility measured the variation with temperature of the relative static susceptibility for both the oxidized and reduced ferredoxin. The results showed that the oxidized protein has two antiferromagnetically coupled iron atoms of the same spin state resulting in diamagnetism at low temperatures ($77^{o}K$) and increasing paramagnetism as the temperature is increased; the coupling constant, J, is approximately $-165\ cm^{-1}$. The reduced protein is also antiferromagnetically coupled resulting in Curie $S = 1/2$ paramagnetism at low temperatures with the paramagnetism decreasing faster than Curie as the temperature is increased; this is consistent with an antiferromagnetic exchange coupling with $J = -116\ cm^{-1}$. The data is also consistent with a $J = -98\ cm^{-1}$ if the first ferrous excited state is $430\ cm^{-1}$ above the ground state.

2. EPR measurements showed that at low temperature ($20^{o}K$) the reduced protein is describable by an effective $S = 1/2$ and principal g-values of $g_{x,y,z} = 1.88, 1.96, 2.05$. EPR showed that

for algal ferredoxin, iron and protons do have hyperfine interactions with the unpaired electron and hence are at the active site. The near identity of algal and spinach ferredoxin allowed one to also conclude from EPR that two labile sulfurs and at least one cysteine sulfur are iron ligands. Most importantly, EPR historically provided the motivation for the study of the ferredoxins and the basic model proposed in 1966 (38). EPR also shows that deuterated and protonated algal ferredoxin are essentially identical.

3. ENDOR spectroscopy showed that there are two nonequivalent iron atoms at the active site and determined the magnitudes of the three principal hyperfine couplings for both the iron atoms. The hyperfine tensors showed that the interaction is reduced approximately 40% due to covalency, that one iron has a nearly spherically symmetric environment while the other is axially distorted with the electron in a d_{z^2} orbital. The ferric ENDOR spectra of protonated and deuterated algal ferredoxin are identical. ENDOR also demonstrated that at least one nitrogen atom, at least five classes of protein protons, and solvent protons have hyperfine interactions with the reducing electron.

4. Mossbauer effect spectroscopy is sensitive to the electronic g-values, the iron hyperfine tensors, the electric field gradient at the nucleus, the ^{57}Fe nuclear quadrupole moment, and the isomer shift. The interpretation required the use of the g-values from EPR and the magnitudes of the two iron hyperfine tensors from ENDOR. With this

information, Mossbauer simulations were able to establish the quadrupole splittings, the isomer shifts, the asymmetry parameter, and the sign of the two iron hyperfine tensors. The interpretation of these parameters showed that the oxidized protein contains two antiferromagnetically coupled high spin ferric atoms, while the reduced protein has a high spin ferric iron (nearly identical to the oxidized ferric) similarly coupled to a high spin ferrous iron with the reducing electron in a d_{z^2} orbital. The temperature dependence of the ferrous Q. S. is consistent with the first excited state lying 430 cm^{-1} above the d_{z^2} ground state.

One can in summary conclude that the plant type ferredoxin from Synechococcus lividus contains two iron atoms which are at the active site and are antiferromagnetically exchange coupled. For the oxidized protein, the irons are both high spin ferric resulting in diamagnetism at low (below 77°K) temperatures. The reduced protein has one high spin ferric and one high spin ferrous iron resulting in an effective spin of 1/2 at low temperatures. The coordination symmetry of the ferric iron in the oxidized and reduced protein is not known, but it is asymmetric enough to produce a measurable electric field gradient at the ferric nucleus; the ferric environment is essentially unchanged by reduction. The ferrous iron has tetrahydral symmetry with rhombic distortions resulting in d_{z^2} being the ground state orbital. Both iron atoms are strongly covalent with spin density on both the labile and cysteine (or possibly methionine)

sulfurs, five classes of protons, and at least one nitrogen (in the case of C. vulgaris). There is no evidence for a direct iron-iron bond.

All of the above data establish the near identity between algal (both protonated and deuterated) and spinach ferredoxin; this conclusion is verified by comparing the results in Tables 3 and 4 with the corresponding series of published articles (4, 5, 6, 7, 8) on spinach ferredoxin. These similarities increase one's confidence in the spinach ferredoxin Mossbauer parameters since all of the hyperfine parameters were measured for algal but not for spinach ferredoxin. By inference, one can also conclude from the infrared spinach ferredoxin data (41) that algal ferredoxin probably has four tetrahedrally oriented (with rhombic distortions) sulfur ligands, two labile sulfur and two cysteine sulfurs. Chemical data on spinach ferredoxin further suggests that the two iron atoms are bonded via the two labile sulfur atoms (42).

Any conclusions beyond the above are less certain due to unexplained data. For instance, the Mossbauer data is particularly frustrating because of its great detail and the inadequacy of some of the computer simulations. The broadness of both the Mossbauer and EPR lines raises unanswered questions about protein microheterogeneity or for the oxidized Mossbauer data, at least the question of inequivalance of the two iron atoms. The very broad Mossbauer absorption for the high field 77^{o}K oxidized protein clearly indicates

that some field dependent interaction is being ignored. There is also ENDOR evidence that some interactions are being neglected since neither the nitrogen nor the iron ENDOR lines are split by exactly twice the nuclear Zeeman interaction. These questions point out the need for a more careful theoretical treatment of the problem. Since the extent of covalency is considerable, the crystal field approximation is a large error and only a full molecular orbital calculation is adequate. For this reason work is continuing on the ligand environment. PMR calculations have shown that there are temperature dependent contact shifted protons which can be identified with one or the other iron depending on the sign of its temperature dependence. Hopefully PMR and ENDOR of isotopically substituted algal ferredoxin will confirm that four of these protons are associated with the cysteine residues at the ferrous iron. Further experiments with ^{15}N algal ferredoxin are being done to determine whether there are one or two nitrogen ligands.

Work is also being done to determine whether the deviations from expected ENDOR splittings are due to inadequacies in earlier perturbation calculations. All crystal field calculations will probably be inadequate, but hopefully additional work will make the correct molecular orbital calculation feasible.

REFERENCES

1. L. E. Mortenson, R. C. Valentine, J. E. Carnahan, Biochem. Biophys. Res. Commun., 7, 448 (1962).

2. G. Palmer and H. Brintzinger, "The Properties of Non-Porphyrin Bound Metals Functional in Biological Oxidation Reduction Reactions" in A Treatise on Electron and Coupled Energy Transfer in Biological Systems, Vol. 2, p. 379, edited by M. Klingenberg and T. E. King, Marcel Dekker, Inc., New York (1972).

3. S. G. Mayhew, D. Petering, G. Palmer, Gordon Foust, J. Biol. Chem., 244, 2830 (1969).

4. G. Palmer and R. H. Sands, J. Biol. Chem., 241, 253 (1966).

5. J. Fritz, R. Anderson, J. A. Fee, G. Palmer, R. H. Sands, J. C. M. Tsibris, I. C. Gunsalus, W. H. Orme-Johnson, and H. Beinert, Biochim. Biophys. Acta, 253, 110 (1971).

6. G. Palmer, W. R. Dunham, J. A. Fee, R. H. Sands, T. Iizuka and T. Yonetani, Biochim. Biophys. Acta, 245, 201 (1971).

7. W. R. Dunham, A. J. Bearden, I. T. Salmeen, G. Palmer, R. H. Sands, W. H. Orme-Johnson, and H. Beinert, Biochim. Biophys. Acta, 253, 134 (1971).

8. G. Palmer, Biochem. Biophys. Res. Commun., 27, 315 (1967).

9. Y. I. Shethna, P. W. Wilson, R. E. Hansen, and H. Beinert, Proc. Natl. Acad. Sci., 52, 1263 (1964).

10. D. V. Der Vartanian, W. H. Orme-Johnson, R. E. Hansen, H. Beinert, R. L. Tsai, J. C. M. Tsibris, R. C. Bartholomaus, and I. C. Gunsalus, Biochem. Biophys. Res. Commun., 26, 569 (1967).

11. J. C. M. Tsibris, R L. Tsai, I. C. Gunsalus, W. H. Orme-Johnson, R. E. Hansen, and H. Beinert, Proc. Natl. Acad. Sci., 59, 959 (1968).

12. W. H. Orme-Johnson, R. E. Hansen, H Beinert, J. C. M. Tsibris, R. C. Bartholomaus, and I. C. Gunsalus, Proc. Natl. Acad. Sci., 60, 368 (1968).

13. J. A. Fee and G. Palmer, Biochim. Biophys. Acta, 245, 175 (1971).

14. J. A. Fee, S. G. Mayhew, and G. Palmer, Biochim. Biophys. Acta, 245, 196 (1971).

15. J. J. Katz and H. L. Crespi, Science, 151, 1187 (1966).

16. H. L. Crespi and J. J. Katz, "Preparation of Deuterated Proteins and Enzymes", in Methods in Enzymology, to be published (1972-1973).

17. B. Hosein, personal communication.

18. A. Abragam and B. Bleaney, Electron Paramagnetic Resonance of Transition Ions, Clarendon Press, Oxford, p. 1 (1970).

19. F. Bloch, Phys. Rev., 70, 460 (1946).

20. C. J. Ballhausen, Introduction to Ligand Field Theory, McGraw-Hill Book Co., Inc. (1962).

21. H. Watanabe, Operator Methods in Ligand Field Theory, Prentice-Hall, Inc. (1966).

22. G. E. Pake, Paramagnetic Resonance, W. A. Benjamin, Inc. (1962).

23. J. S. Griffith, Theory of the Transition Metal Ions, Cambridge University Press (1961).

24. R. H. Sands, Phys. Rev., 99, 1222 (1955).

25. F. K. Kneubuhl, J. Chem. Phys., 33, 1074 (1960).

26. F. K. Kneubuhl and B. Natterer, Helv. Phys. Acta, 34, 710 (1961).

27. A. Abragam and B. Bleaney, Electron Paramagnetic Resonance of Transition Ions, Clarendon Press, Oxford, p. 217 (1970).

28. J. S. Hyde, "ENDOR with Intense R. F. Fields", in Proceedings of the International Conference on Magnetic Resonance in Biological Systems, Pergammon Press, London (1967).

29. W. R. Dunham, Ph. D. Thesis, University Microfilms, Ann Arbor, Michigan., 1970, Order № 70-19, 588.

30. S. De Benedetti, F. Des Barros, and G. R. Hoy, "Chemical and Structural Effects on Nuclear Radiations" in Nuclear Interactions, Wiley (1966).

31. P. G. De Brunner, "Mossbauer Spectroscopy of Biomolecules" in Mossbauer Effect Methodology, Vol. 4, edited by I. J. Gruverman, Plenum Press, New York (1969).

32. R. Ingalls, Phys. Rev., 133A, 287 (1964).

33. J. Hyde, J. Chem. Phys., 43, 1806 (1965).

34. J. Fritz, Ph. D. Thesis, University Microfilms, Ann Arbor, Michigan, 1970, Order № 70-14524.

35. T. Iizuka and M. Kotani, Biochim. Biophys. Acta, 181, 275 (1969).

36. I. T. Salmeen, Ph. D. Thesis, University Microfilms, Ann Arbor, Michigan, 1969, Order № 70-4181.

37. J. F. Gibson, D. O. Hall, J. H. Thornley, and F. R. Whatley, Proc. Natl. Acad. Sci., 56, 987 (1966).

38. R. S. Title, Phys. Rev., 131, 623 (1963).

39. R. E. Watson and A. J. Freeman, Phys. Rev., 123, 2027 (1961).

40. W. T. Oosterhuis and G. Lang, Phys. Rev., 178, 439 (1969).

41. W. A. Eaton, G. Palmer, J. A. Fee, T. Kimura, and W. Lovenberg, Proc. Natl. Acad. Sci., 68, 3015 (1971).

42. W. R. Dunham, G. Palmer, R. H. Sands, and A. J. Bearden, Biochim. Biophys. Acta, 253, 373 (1971).

APPENDIX

CALCULATION OF ENDOR SPECTRA

An ENDOR FORTRAN computer program has been adapted to calculate powder ENDOR spectra for two nonequivalent ground state iron nuclei ($I = 1/2$) having an electron-nuclear hyperfine interaction with a net electronic spin $S = 1/2$. The electronic g-tensor and each of the two hyperfine tensors may be anisotropic and have arbitrary orientations.

For an anisotropic electronic g-tensor, the Zeeman Hamiltonian in the g-tensor principal axis frame can be written,

$$\mathcal{H} = H \cdot g \cdot S$$

$$= (g_x H_x S_x + g_y H_y S_y + g_z H_z S_z)$$

If the g-frame is related to the lab frame by three Euler rotation angles (α, β, γ; Whittaker convention) then for a magnetic field applied along the lab z-axis, the field in the g-frame will have components,

$$H_x = -H_o \sin\beta\cos\gamma$$

$$H_y = H_o \sin\beta\sin\gamma$$

$$H_z = H_o \cos\beta$$

The electronic Zeeman Hamiltonian operator in the g-frame can then be written as,

$$= g\ H_o(-g_x \sin\beta\cos\gamma\, S_x + g_y \sin\beta \sin\gamma\, S_y + g_z \cos\beta\, S_z) \qquad \text{Eq. 1}$$

$$= g_{eff}\ H_o S_z$$

where, $g_{eff}^2 = g_x^2 \sin^2\beta \cos^2\gamma + g_y^2 \sin^2\beta \sin^2\beta + g_z^2 \cos^2\beta$

Equation 2 is obtained from the nondiagonal form by a coordinate transformation from the g-frame to the tilde frame, in which the electronic Zeeman Hamiltonian is diagonalized.

The electron-nuclear hyperfine interaction is assumed small with respect to the electronic Zeeman term, so it must be evaluated in the diagonalized Zeeman frame. Assuming for the moment that the A-tensor is anisotropic, but coincident with the g-frame, the hyperfine Hamiltonian in the g-frame can be written,

$$\mathcal{H}_{hyp} = A_x I_x S_x + A_y I_y S_y + A_z I_z S_x$$

The rotation of the electronic spin operators to the diagonalized Zeeman frame gives,

$$\mathcal{H}_{hyp} = A I S_z^2$$

where, $A = \frac{1}{g}\left(g_x^2 A_x^2 \sin^2\beta\cos^2\gamma + g_y^2 A_y^2 \sin\beta\sin^2\beta + g_z^2 A_z^2 \cos^2\beta\right)^{1/2}$

If the hyperfine tensor is not coincident with the g-tensor but related to it by three Euler rotations (ψ, θ, ϕ) then the electronic spin operators must first be rotated to the g-tensor frame and then to the diagonalized Zeeman frame. The net result is written the same, but now the effective A-tensor includes the effect of both rotations.

The program, ENDOR 3, calculates powder ENDOR spectra as follows:

A. Input data is read:

1. Card 1:

a. LSHAPE - ENDOR line shape. O = Gaussian,
1 = Lorentzian.

b. IFPRT - ENDOR print option. 0 = no print,

1 = print line spectrum.

c. IFPEPR - EPR print option. 0 = no print,

1 = print EPR line spectrum.

d. NMENDR - number of ENDOR fields.

e. MO - number of angle θ intervals.

f. NO - number of angle ϕ intervals.

g. NMBR - number of points in EPR line spectrum.

h. MRF - number of points in ENDOR line spectrum.

i. IGA - switch for noncoincident A & g tensors,

0 = no rotation, 1 = rotate.

2. Card 2:

RECORD - label and comments.

3. Card 3:

a. XNU - microwave frequency (Ghz).

b. RF1 - first element in rf field array (mhz).

c. RINC - interval between rf points (mhz).

d. DLTH - θ interval (degrees).

e. DLPH - ϕ interval (degrees).

f. DRL - multiple of linewidth at which EPR lineshape

is truncated.

g. RLR - ENDOR linewidth (mhz).

h. FPRB - output scaling factor.

4. Card 4:

   G(1,2,3) - g_x, g_y, g_z.

5. Card 5:

   a. A(1,2,3) - Iron #1 A-values (mhz).

   b. AH(1,2,3) - Iron #1 Euler angles (degrees).

   c. A(4,5,6) - Iron #2 A-values.

   d. AH(4,5,6) - Iron #2 Euler angles.

6. Card 6:

   RLW(1,2,3) - EPR anisotropic linewidth (gauss).

7. Card 7:

   HENDOR - EPR static fields for ENDOR (kgauss).

8. Card 8:

   Blank.

B. Trigonometric functions (SN(I), SNSQ(I), CS(I), CSSQ(I)) arrays for 0-180^{o} are calculated and stored. MO increments of DLTH are calculated.

C. An EPR field array, H(I), is constructed of NMBR increments of HINC gauss each beginning at H1 = H_z - 20 gauss - DRLxRLW(z) and ending above H_x, at HMAX = H_x + 20 gauss + DRLxRLW(x).

D. An RF field array, RF(I), is constructed of MRF increments of RINC each.

E. The two A-tensors are rotated to the g-frame using a rotation subroutine ROTVEC and are then transformed to the frame in which the electronic Zeeman interaction is diagonal.

F. The effective values for the g-tensor (GE), EPR linewidth (LX, LY, LZ), the two A-tensors (AE & AEF), and the iron Zeeman splitting (XNUFE) are calculated for each value of θ, θ from 0-180°.

G. The four lines for the EPR stick spectrum are calculated for each GE and their magnitudes are weighted by the solid angle.

H. The ENDOR stick spectrum is calculated for each EPR line with resonances at,

$$\nu_{rf} = \frac{AE}{2} \pm \text{XNUFE} \quad \text{and} \quad \frac{AEF}{2} \pm \text{XNUFE}$$

I. For the desired ENDOR field the program searches above and below the field by DRL linewidths (RLW(I)). Each contributing line is weighted by the EPR intensity and the position on the gaussian shape function applied to each line, and then summed in the array ENDOR (field, freq).

J. The ENDOR stick spectrum is convoluted with either a Lorentzian or Gaussian line shape and contributions from overalpping distributions are summed resulting in the final output, CONVEN(I), I = 1, MRF.

K. A "print-plot" program is included which plots the output points every 0.1 MHz for each ENDOR field in 10 MHz wide spectra (1 inch = 1 MHz).

```
C         PROGRAM ENDOR 3
C              VERSION 3.003        (MAY 1972)
C     ENDOR 3 SIMULATES SPECTRA FOR TWO NONEQUIVALENT NONCOINCIDENT IRON NUCLEI
C
      COMMON ENDOR,FINEND,RF,CONVEN,PEND
      DIMENSION AH(6),ATRIG(6),H(3,3)
      DIMENSION G(3),A(6),PLW(3),HIN(3),FLAB(10)
      DIMENSION SN(100),CS(100),H(100),EPR(100),COUNT(100),NAME(6)
      DIMENSION ENDOR(100,800),FINEND(800),RF(800),HENDOR(6),NA(2)
      DIMENSION SNSQ(100),CSSQ(100),FLW(100),CONVEN(800),SPEC(100)
      DIMENSION RECORD(18),PEND(800)
      DATA NAME/'GAUS','SIAN','    ','LORE','NTZI','AN  '/,SCALE/1.000/
 8000 FORMAT(8F10.5)
 8010 FORMAT(18A4)
 8020 FORMAT(7F7.2,E7.2)
 8030 FORMAT(3I1,I7,5I10)
 9000 FORMAT('-ENDOR LINE SHAPE IS ',3A4//1X,2(5X,'RF',7X,'INTENSITY',
     17X)//(1X,2(F8.3,2X,F15.8,5X)))
 9001 FORMAT('1NMENDR =',I3,6X,'HENDOR =',6F10.2)
 9002 FORMAT('-NMBR =',I5,5X,'IGA =',I5//
     1' MO =',I5,5X,'DLTH =',F7.3,' DEG.'/' NO =',
     215,5X,'DLPH =',F7.3,' DEG.'//' MRF =',I5,5X,'RF1 =',F10.5,' MHZ',
     35X,'RINC =',F10.5,' MHZ'//' NU =',F7.3,' GHZ',5X,
     4//9X,'H',11X,'G',9X,'L',9X,'A',9X,'AH'
     5//(' (',I1,') ',F7.2,5X,F6.4,5(5X,F7.2)))
 9003 FORMAT('0DRL =',F7.3,5X,'FPRB =',E10.2,5X,'RLR =',F7.3,5X)

 9004 FORMAT('1SPECTRUM NO. ',I2,' (OF ',I2,')',10X,'HENDOR =',F8.2)
 9005 FORMAT('-*** ILLEGAL CHARACTER FOR LSHAPE.   LSHAPE =',I1)
 9006 FORMAT('-  ENDOR LINE SPECTRUM'//1X,'    RF  ',10(5X,'(',F5.3,')')
     1/)
 9007 FORMAT('2EPR SPECTRUM      H(1) =',F8.2,'  TO H(',I3,') =',F8.2,
     1'  IN HINC =',F8.3)
 9008 FORMAT('-EPR'//(1X,10F10.6))
 9009 FORMAT('-FLW'//(1X,10F10.2))
 9010 FORMAT('-COUNT'//(1X,10F10.1))
 9011 FORMAT(1X,F8.3,2X,10F12.6)
 9012 FORMAT('0',5X,18A4)
C
C     BEGIN ENDOR -- READ DATA
C
  100 READ(5,8030)LSHAPE,IFPRT,IFPEPR,NMENDR,MO,NO,NMBR,MRF,IGA
      IF(NMENDR.EQ.0)CALL EXIT
      READ(5,9010)(RECORD(I),I=1,18)
      READ(5,8020)XNU,RF1,RINC,DLTH,DLPH,DRL,RLR,FPRB
      READ(5,8000)(G(I),I=1,3)
      READ(5,8000)(A(I),I=1,6)
      READ(5,8000)(AH(I),I=1,6)
      READ(5,8000)(PLW(I),I=1,3)
      READ(5,8000)(HENDOR(I),I=1,NMENDR)
      IF(FPRB.LE.0.0)FPRB=1.0
C
C     PRINT HEADING AND ECHO PRINT INPUT DATA
C
      CONST1=714.443*XNU
      HA=CONST1/2000.0
```

```
      DO 200 I=1,3
  200 HIN(I)=CONST1/G(I)
      WRITE(6,9001)NMENDR,(HENDOR(I),I=1,NMENDR)
      WRITE(6,9012)(RECORD(I),I=1,18)
      WRITE(6,9003)DRL,EPSB,RLR
      WRITE(6,9002)NMBR,IGA,MO,DLTH,NO,DLPH,MRF,RF1,RINC,XNU,
     1(I,HIN(I),G(I),RLW(I),A(I),AH(I),A(I+3),AH(I+3),I=1,3)
C
C     SET UP TRIGONOMETRIC FUNCTION TABLES
C
      RAD=0.017453
      DLTH=DLTH*RAD
      DLPH=DLPH*RAD
      THTA=DLTH*0.5
      IT=MO+1
      MP=MO/2
      MO=MP+1
      DO 300 I=1,MP
      J=MO-I
      CS(I)=COS(THTA)
      CSSQ(I)=CS(I)**2
      SN(J)=CS(I)
      SNSQ(J)=CSSQ(I)
      THTA=THTA+DLTH
  300 CONTINUE
      DO 301 I=MO,MO
      J=IT-I
      SN(I)=SN(J)
      SNSQ(I)=SNSQ(J)
      CS(I)=-CS(J)
      CSSQ(I)=CSSQ(J)
  301 CONTINUE
C
C     CLEAR ARRAYS AND SET UP FIELD ARRAYS
C
      H1=HIN(3)-20.0-DRL*RLW(3)
      HMAX=HIN(1)+20.0+DRL*RLW(1)
      HINC=(HMAX-H1)/NMBR
      H1=H1+0.5*HINC
      DO 400 I=1,NMBR
      EPR(I)=0.0
      COUNT(I)=0.0
      FLW(I)=0.0
      H(I)=H1
      H1=H1+HINC
  400 CONTINUE
      DO 410 I=1,MRF
      RF(I)=RF1
      FIMEND(I)=0.0
      DO 420 J=1,NMBR
      ENDOR(J,I)=0.0
  420 CONTINUE
      RF1=RF1+RINC
  410 CONTINUE
C
      GX=G(1)
      GY=G(2)
      GZ=G(3)
C
C     CREATE A-TENSOR
```

```
      AX=A(1)
      AY=A(2)
      AZ=A(3)
      AXX=AX
      AYY=AY
      AZZ=AZ
      AXY=0.0
      AXZ=0.0
      AYZ=0.0
      AXF=A(4)
      AYF=A(5)
      AZF=A(6)
      AXXF=AXF
      AYYF=AYF
      AZZF=AZF
      AXYF=0.0
      AXZF=0.0
      AYZF=0.0
C     SET UP BRANCH POINT FOR ORIENTATION OF HYPERFINE PRINCIPAL AXES
      IF(IGA.EQ.0) GO TO 189
C     COMPUTE TRANSFORMATION MATRIX FOR VECTOR OPERATORS FOR ROTATION
C     FROM A TENSOR TO G TENSOR PRINCIPAL AXES
      DO 90 I=1,3
      AH(I)=AH(I)*RAD
      ATRIG(I)=COS(AH(I))
      ATRIG(I+3)=SIN(AH(I))
   90 CONTINUE
      CALL ROTVEC(ATRIG,W)
C     COMPUTE A TENSOR COMPONENTS IN G-TENSOR FRAME
      AXX=AX*W(1,1)*W(1,1)+AY*W(2,1)*W(2,1)+AZ*W(3,1)*W(3,1)
      AYY=AX*W(1,2)*W(1,2)+AY*W(2,2)*W(2,2)+AZ*W(3,2)*W(3,2)
      AZZ=AX*W(1,3)*W(1,3)+AY*W(2,3)*W(2,3)+AZ*W(3,3)*W(3,3)
      AXY=AX*W(1,1)*W(1,2)+AY*W(2,1)*W(2,2)+AZ*W(3,1)*W(3,2)
      AXZ=AX*W(1,1)*W(1,3)+AY*W(2,1)*W(2,3)+AZ*W(3,1)*W(3,3)
      AYZ=AX*W(1,2)*W(1,3)+AY*W(2,2)*W(2,3)+AZ*W(3,2)*W(3,3)
      DO 91 I=1,3
      AH(I+3)=AH(I+3)*RAD
      ATRIG(I)=COS(AH(I+3))
      ATRIG(I+3)=SIN(AH(I+3))
   91 CONTINUE
      CALL ROTVEC(ATRIG,W)
      AXXF=AXF*W(1,1)*W(1,1)+AYF*W(2,1)*W(2,1)+AZF*W(3,1)*W(3,1)
      AYYF=AXF*W(1,2)*W(1,2)+AYF*W(2,2)*W(2,2)+AZF*W(3,2)*W(3,2)
      AZZF=AXF*W(1,3)*W(1,3)+AYF*W(2,3)*W(2,3)+AZF*W(3,3)*W(3,3)
      AXYF=AXF*W(1,1)*W(1,2)+AYF*W(2,1)*W(2,2)+AZF*W(3,1)*W(3,2)
      AXZF=AXF*W(1,1)*W(1,3)+AYF*W(2,1)*W(2,3)+AZF*W(3,1)*W(3,3)
      AYZF=AXF*W(1,2)*W(1,3)+AYF*W(2,2)*W(2,3)+AZF*W(3,2)*W(3,3)
  189 CONTINUE
C     TRANSFORM TO FRAME WHERE ELECTRON ZEEMAN IS DIAGONAL
      GXSQ=GX**2
      GYSQ=GY**2
      GZSQ=GZ**2
      DEL=DLTH*DLPH*FPRB
      AXXX=AXX*GX
      AXYY=AXY*GY
      AXZZ=AXZ*GZ
      AYXX=AXY*GX
      AYYY=AYY*GY
      AYZZ=AYZ*GZ
      AZXX=AXZ*GX
```

```
      AZYY=AYZ*GY
      AZZZ=AZZ*GZ
      AXXXF=AXXF*GX
      AXYYF=AXYF*GY
      AXZZF=AXZF*GZ
      AYXXF=AXYF*GX
      AYYYF=AYYF*GY
      AYZZF=AYZF*GZ
      AZXXF=AXZF*GX
      AZYYF=AYZF*GY
      AZZZF=AZZF*GZ
      RX=RLW(1)**2
      RY=RLW(2)**2
      RZ=RLW(3)**2
      RINC=1.5-PF(1)/RINC
      RNC=2*RINC
C     SUM OVER ANGLE THETA STARTS HERE
  190 DO 1000 I=1,MD
      PROB=SN(I)*DEL/2
      RXS=RX*SNSQ(I)
      RYS=RY*SNSQ(I)
      RZC=RZ*CSSQ(I)
      GXSN=GXSQ*SNSQ(I)
      GYSN=GYSQ*SNSQ(I)
      GZCS=GZSQ*CSSQ(I)
      ASXX=-AXXX*SN(I)
      ASXY=AXYY*SN(I)
      ASXZ=AXZZ*CS(I)
      ASYX=-AYXX*SN(I)
      ASYY=AYYY*SN(I)
      ASYZ=AYZZ*CS(I)
      ASZX=-AZXX*SN(I)
      ASZY=AZYY*SN(I)
      ASZZ=AZZZ*CS(I)
      ASXXF=-AXXXF*SN(I)
      ASXYF=AXYYF*SN(I)
      ASXZF=AXZZF*CS(I)
      ASYXF=-AYXXF*SN(I)
      ASYYF=AYYYF*SN(I)
      ASYZF=AYZZF*CS(I)
      ASZXF=-AZXXF*SN(I)
      ASZYF=AZYYF*SN(I)
      ASZZF=AZZZF*CS(I)
C     SUM OVER ANGLE PHI STARTS HERE
      DO 1010 J=1,NO
      GE=SQRT(GXSN*CSSQ(J)+GYSN*SNSQ(J)+GZCS)
      AXP=(ASXX*CS(J)+ASXY*SN(J)+ASXZ)/GE
      AYP=(ASYY*SN(J)+ASYX*CS(J)+ASYZ)/GE
      AZP=(ASZZ+ASZX*CS(J)+ASZY*SN(J))/GE
      AE=SQRT(AXP**2+AYP**2+AZP**2)
      AXPF=(ASXXF*CS(J)+ASXYF*SN(J)+ASXZF)/GE
      AYPF=(ASYYF*SN(J)+ASYXF*CS(J)+ASYZF)/GE
      AZPF=(ASZZF+ASZYF*CS(J)+ASZXF*SN(J))/GE
      AEF=SQRT(AXPF**2+AYPF**2+AZPF**2)
C     EFFECTIVE ZEEMAN FIELD ALONG DIRECTION OF NUCLEAR QUANTIZATION
C     WHICH HAS DIRECTION COSINES AXP/AE,AYP/AE,AZP/AE
      HE=HA*(-AXP*SN(I)*CS(J)+AYP*SN(I)*SN(J)+AZP*CS(I))/AE
      HEF=HA*(-AXPF*SN(I)*CS(J)+AYPF*SN(I)*SN(J)+AZPF*CS(I))/AEF
C     ENDOR LINES ARE AT AF/2 + OR - GN*R*HE
      XNUFE=0.138*HE
```

```
      XNUEEE=0.138*HEE
C     GENERATION OF EPR POSITIONS FOR 1:2:1 TRIPLET
      AP=AE/(GE*1.40)
      APE=AEE/(GE*1.40)
      DHP=CONST1/GE-H(1)
      MHEA=(DHP-AP/2-APE/2)/HINC +1.5
      MHEB=(DHP-AP/2+APE/2)/HINC +1.5
      MHEC=(DHP+AP/2-APE/2)/HINC +1.5
      MHED=(DHP+AP/2+APE/2)/HINC +1.5
      NDRA=AEE/RNC+RENC-XNUEEE/RINC
      NDRB=AEE/RNC+RENC+XNUEEE/RINC
      NDRC=AE/RNC+RENC-XNUEE/RINC
      NDRD=AE/RNC+RENC+XNUEE/RINC
      ENDOR(MHEA,NDRA)=ENDOR(MHEA,NDRA)+PROB
      ENDOR(MHEA,NDRB)=ENDOR(MHEA,NDRB)+PROB
      ENDOR(MHEA,NDRC)=ENDOR(MHEA,NDRC)+PROB
      ENDOR(MHEA,NDRD)=ENDOR(MHEA,NDRD)+PROB
      ENDOR(MHEB,NDRA)=ENDOR(MHEB,NDRA)+PROB
      ENDOR(MHEB,NDRB)=ENDOR(MHEB,NDRB)+PROB
      ENDOR(MHEB,NDRC)=ENDOR(MHEB,NDRC)+PROB
      ENDOR(MHEB,NDRD)=ENDOR(MHEB,NDRD)+PROB
      ENDOR(MHEC,NDRA)=ENDOR(MHEC,NDRA)+PROB
      ENDOR(MHEC,NDRB)=ENDOR(MHEC,NDRB)+PROB
      ENDOR(MHEC,NDRC)=ENDOR(MHEC,NDRC)+PROB
      ENDOR(MHEC,NDRD)=ENDOR(MHEC,NDRD)+PROB
      ENDOR(MHED,NDRA)=ENDOR(MHED,NDRA)+PROB
      ENDOR(MHED,NDRB)=ENDOR(MHED,NDRB)+PROB
      ENDOR(MHED,NDRC)=ENDOR(MHED,NDRC)+PROB
      ENDOR(MHED,NDRD)=ENDOR(MHED,NDRD)+PROB
      EPR(MHEA)=EPR(MHEA)+PROB
      EPR(MHEB)=EPR(MHEB)+PROB
      EPR(MHEC)=EPR(MHEC)+PROB
      EPR(MHED)=EPR(MHED)+PROB
      TLW=SQRT(PXS*CSSC(J)+PYS*SNSQ(J)+RZC)
      FLW(MHEA)=FLW(MHEA)+TLW
      FLW(MHEB)=FLW(MHEB)+TLW
      FLW(MHEC)=FLW(MHEC)+TLW
      FLW(MHED)=FLW(MHED)+TLW
      COUNT(MHEA)=COUNT(MHEA)+1.0
      COUNT(MHEB)=COUNT(MHEB)+1.0
      COUNT(MHEC)=COUNT(MHEC)+1.0
      COUNT(MHED)=COUNT(MHED)+1.0
 1010 CONTINUE
 1000 CONTINUE
C
C     END OF CALCULATION OF EPR LINE SPECTRUM -- EPR PRINT OPTION FOLLOWS
C
      IF(IEPRPR.EQ.0)GO TO 1018
      WRITE(6,9007)H(1),NMBR,H(NMBR),HINC
      WRITE(6,9008)(EPR(I),I=1,NMBR)
      WRITE(6,9009)(FLW(I),I=1,NMBR)
      WRITE(6,9010)(COUNT(I),I=1,NMBR)
C
C     SET UP BRANCHING FOR ENDOR LINE SHAPE
C
 1018 IF(LSHAPE.EQ.0)GO TO 1011
      IF(LSHAPE.EQ.1)GO TO 1012
      IF(LSHAPE.EQ.2)GO TO 1013
      WRITE(6,9005)LSHAPE
      CALL EXIT
```

```
 1011 ASSIGN 1021 TO LE1
      ASSIGN 1040 TO LE2
      ASSIGN 1020 TO LE3
      ASSIGN 1200 TO LE4
      GO TO 1016
 1012 LCODE=1
      GO TO 1014
 1013 LCODE=2
 1014 ASSIGN 1019 TO LE1
      ASSIGN 1050 TO LE2
      ASSIGN 1090 TO LE3
      ASSIGN 1100 TO LE4
C
C     SET INITIAL VALUES, INCREMENTS, AND TEST VALUES FOR CALCULATION
C        OF ENDOR SPECTRUM
C
 1016 CONTINUE
      BIGL=0.0
      DO 1017 I=1,3
      IF(RLW(I).LE.BIGL)GO TO 1017
      BIGL=RLW(I)
 1017 CONTINUE
      NMAX=BIGL*ORL/HINC+0.5
C
C     BRANCH FOR ENDOR LINE SHAPE -- CALC. OF BASIC ABSORPTION LINE FOLLOWS
C
      GO TO LE4,(1100,1200)
 1100 DO 1101 I=1,100
 1101 SPEC(I)=0.0
      CALL SHAPE(SPEC,LCODE,IDEL,NSPEC,RINC,RLR)
C
C     BEGIN CALCULATION OF ENDOR SPECTRUM -- LOOP FOR EACH RESONANCE OBSERVED
C
 1200 DO 1020 K=1,NMENDR
C
C     CLEAR ARRAYS
C
      DO 1021 L2=1,MPF
      FINEND(L2)=0.
      GO TO LE1,(1019,1021)
 1019 CONVEN(L2)=0.0
 1021 CONTINUE
C
C
      HH=HENDOR(K)-H(1)
      KH=HH/HINC+1.5
C
C
      NA(1)=-1
      NA(2)=1
C
C     SEARCH FOR CONTRIBUTING EPR LINES
C
      DO 1035 LO=1,2
      NI=KH
      DO 1040 K3=1,NMBR
      NI=NI+NA(LO)
      IF(K3.GT.NMAX.OR.NI.LT.1.OR.NI.GT.NMBR)GO TO 1035
      IF(EPR(NI).EQ.0.0)GO TO 1040
      XLW=FLW(NI)/COUNT(NI)
```

```
      Z=H(NI)-H(KH)
C
C     CALCULATE CONTRIBUTION TO ENDOR LINE SPECTRUM -- BRANCH IF NONE
C
      IF(DRL*XLW.LT.ABS(Z))GO TO 1035
      S1=S(Z,XLW)
      DO 1060 IR=1,MRF
      IF(ENDOR(NI,IR).EQ.0.0)GO TO 1059
      PEND(IR)=S1*ENDOR(NI,IR)
      FINEND(IR)=FINEND(IR)+PEND(IR)
      GO TO 1060
 1059 PEND(IR)=0.0
 1060 CONTINUE
C
C     BRANCH FOR CONVOLUTED SPECTRUM -- CONVOLUTION FOLLOWS
C
      GO TO (2,(1040,1050)
 1050 DO 1054 I=1,MRF
      IF(PEND(I).EQ.0.0)GO TO 1054
      JZERO=I-IDEL-1
      DO 1052 J=1,NSPEC
      JR=JZERO+J
      IF(JR.LT.1)GO TO 1052
      IF(JR.GT.MRF)GO TO 1054
      CONVEN(JR)=CONVEN(JR)+PEND(I)*SPEC(J)
 1052 CONTINUE
 1054 CONTINUE
 1040 CONTINUE
 1035 CONTINUE
C
C     END CALCULATION OF ENDOR SPECTRUM -- PRINT OF SPECTRUM HEADING FOLLOWS
C
      WRITE(6,9004)K,NMENDR,HENDOR(K)
C
C     ENDOR LINE SPECTRUM PRINT OPTION -- PRINT FOLLOWS
C
      IF(IPRT.EQ.0)GO TO 1090
      DO 1063 I=1,MRF
 1063 FINEND(I)=FINEND(I)*SCALE
      DO 1061 I=1,10
      IL=I-1
 1061 FLAB(I)=IL*RINC
      WRITE(6,9006)(FLAB(I),I=1,10)
      IMAX=MRF/10
      DO 1062 I=1,IMAX
      J2=I*10
      J1=J2-9
 1062 WRITE(6,9011)RF(J1),(FINEND(J),J=J1,J2)
      IDI=MRF-J2
      IF(IDI.LE.0)GO TO 1064
      J1=J2+1
      J2=J2+IDI
      WRITE(6,9011)RF(J1),(FINEND(J),J=J1,J2)
 1064 GO TO (3,(1020,1090)
C
C     PRINT FINAL ENDOR SPECTRUM
C
 1090 N2=3*LCODE
      N1=N2-2
      DO 1091 I=1,MRF
```

```
 1091 CONVEN(I)=CONVEN(I)*SCALE
      DIMENSION IMAGE(5567),NSCALE(5)
      DATA NSCALE(1)/0/
      CALL PLOT1(NSCALE(1),2,40,2,100)
      CALL PLOT2(IMAGE,10.0,0.0,1.0,0.0)
      CALL PLOT3('X',RE(1),CONVEN(1),100,4)
      CALL PLOT4(9,'INTENSITY')
 3999 FORMAT(1H1)
      WRITE(6,3999)
      CALL PLOT1(NSCALE(1),2,40,2,100)
      CALL PLOT2(IMAGE,20.0,10.0,1.0,0.0)
      CALL PLOT3('Y',RE(101),CONVEN(101),100,4)
      CALL PLOT4(9,'INTENSITY')
      WRITE(6,3999)
      CALL PLOT1(NSCALE(1),2,40,2,100)
      CALL PLOT2(IMAGE,30.0,20.0,1.0,0.0)
      CALL PLOT3('Z',RE(201),CONVEN(201),100,4)
      CALL PLOT4(9,'INTENSITY')
 1020 CONTINUE
      GO TO 100
      END
      FUNCTION S(Z,XLW)
C
C  S CALCULATES THE GAUSSIAN ABSORPTION LINE SHAPE FOR USE IN DETERMINING
C  WHETHER A PARTICULAR EPR LINE WILL CONTRIBUTE TO THE ENDOR LINE.
C
      S=1.0/(1.414214*1.772454*XLW)*EXP(-0.5*(Z/XLW)**2)
      RETURN
      END
      SUBROUTINE SHAPE(SPEC,LCODE,IDEL,NSPEC,RINC,RLR)
C
C  SHAPE GENERATES THE BASIC ENDOR LINE SHAPE TO BE APPLIED TO EACH
C  POINT IN THE ENDOR LINE SPECTRUM.  EACH POINT IN THE BASIC SPECTRUM
C  WILL BE MULTIPLIED BY THE INTENSITY OF THE ENDOR LINE.
C
      DIMENSION SPEC(100),DRL(2)
      DATA DRL/5.0,10.0/,PI/3.141593/
      T2=1.0/RLR
      T2SQR=T2*T2
      IDEL=DRL(LCODE)*RLR/RINC+0.5
      NSPEC=2*IDEL+1
      IRMIN=-IDEL-1
      DO 100 I=1,NSPEC
      Z=(IRMIN+I)*RINC
      C1=T2SQR*Z*Z
      GO TO (90,80),LCODE
   80 C2=PI*(1.0+C1)
      GO TO 100
   90 C2=SQRT(2.0*PI)*EXP(0.5*C1)
  100 SPEC(I)=T2/C2
      RETURN
      END
      SUBROUTINE ROTVEC(X,R)
      DIMENSION X(6),R(3,3)
      R(1,1)=X(1)*X(2)*X(3)-X(4)*X(6)
      R(1,2)=X(4)*X(2)*X(3)+X(1)*X(6)
      R(1,3)=-X(5)*X(3)
      R(2,1)=-X(1)*X(2)*X(6)-X(4)*X(3)
      R(2,2)=-X(4)*X(2)*X(6)+X(1)*X(3)
      R(2,3)=X(5)*X(6)
```

```
R(3,1)=X(1)*X(5)
R(3,2)=X(4)*X(5)
R(3,3)=X(2)
RETURN
END
```